THESIS

QUANTIFYING DEEP CONVECTIVE INFLUENCE ON THE TROPICAL TROPOPAUSE LAYER (TTL)

Submitted by

Laura C. Paulik

Department of Atmospheric Science

In partial fulfillment of the requirements

For the Degree of Master of Science

Colorado State University

Fort Collins, Colorado

Fall 2011

Master's Committee:

Advisor: Thomas Birner

Graeme Stephens
Colette Heald
David Krueger

ABSTRACT

QUANTIFYING DEEP CONVECTIVE INFLUENCE ON THE TROPICAL TROPOPAUSE LAYER (TTL)

The transition between the troposphere and the stratosphere is best described as a layer containing both tropospheric and stratospheric characteristics. In the tropics, this region is known as the Tropical Tropopause Layer (TTL). The TTL roughly spans the altitude range of 12-18 km, bounded from above by the cold point tropopause (CPT) and from below by the main convective outflow level. This region is unique in that it is subject to both tropospheric and stratospheric processes (e.g. deep convective transport/the stratospheric circulation). Processes in the TTL set the boundary condition for atmospheric constituents entering the stratosphere. This thesis aims to better quantify deep convective influence on the TTL using two approaches.

The first approach investigates TTL ozone using the Southern Hemisphere Additional Ozonesondes (SHADOZ) dataset. Low ozone concentrations in the TTL are indicative of deep convective transport from the boundary layer. A new diagnostic, the "ozone mixing height" is introduced that identifies the maximum altitude in a vertical ozone profile up to which reduced ozone concentrations, typical of transport from the boundary layer are observed. Deep convective

temperature and stratification signals in the TTL are quantified using this diagnostic.

The second approach collocates deep convective clouds identified by CloudSat 2B-CLDCLASS with COSMIC GPS temperature profiles. Results suggest the convective temperature signal is large-scale and persistent in time; however, it is only the convective events that penetrate into the upper half of the TTL that have a significant impact on TTL temperature. Finally, CloudSat 2B-CLDCLASS data is used in conjunction with the SHADOZ dataset revealing that deep convective cloud top heights appear to be well approximated by the level of neutral buoyancy.

ACKNOWLEDGEMENTS

A special thank you to Dr. Thomas Birner for his continued guidance throughout the research and writing process. I would also like to recognize Dr. Graeme Stephens, Dr. Colette Heald, and Dr. David Krueger for encouraging and supporting this research.

TABLE OF CONTENTS

1. INTRODUCTION

The region of focus in this thesis is the tropical tropopause layer (TTL). In the tropics, the cross over between the troposphere and the stratosphere is hard to pinpoint; rather than a definite boundary, a transition layer exists that contains characteristics of both the troposphere and the stratosphere. The TTL is unique in that both stratospheric and tropospheric processes influence its properties.

The "wave driven" global-scale stratospheric circulation has a significant impact on TTL temperature and composition and largely constrains the bulk of the troposphere-to-stratosphere transport to occur across the tropical tropopause. Vertically propagating Rossby waves that originate in the troposphere and break in the stratosphere impart an easterly acceleration and a deceleration of the zonal flow. The Coriolis force acts to balance this, creating a poleward circulation depicted in Figure 1.1, with upwelling in the tropics and subsidence over high latitudes (Vallis 2006). This means the extratropical stratosphere constantly acts on the lower tropical stratosphere creating a sort of "suction pump." (Holton et al. 1995). Therefore, the TTL sets the boundary condition for atmospheric constituents entering the stratosphere.

Deep convection in the tropical troposphere has a significant impact on TTL temperature and composition as well, with the capacity to transport air from the surface to the TTL within 1-2 hours. Previous studies have found ozone to be a

useful indicator of deep convection, where low ozone concentrations in the TTL are indicative of deep convective transport from the boundary layer (Kley et al. 1996, Folkins et al. 1999). An understanding of TTL ozone composition is also important for determining the region's radiative budget.

TTL temperature, modulated by both the stratospheric circulation and deep convection, is fundamental for determining stratospheric water vapor. The stratosphere is very dry, having a mixing ratio of around 3 ppmv (Highwood and Hoskins 1998). Brewer (1949) proposed the "freeze-drying" mechanism, where tropospheric air ascending into the stratosphere passes through the cold point tropopause (CPT), the lowest temperature observed in a vertical profile, and dehydrates to the local saturation mixing ratio. However, the zonally averaged CPT temperature is not low enough to produce the observed stratospheric mixing ratio. Rather, only CPT temperatures in localized regions with strong deep convective influence are low enough to match water vapor observations; these regions include the west Pacific, northern Australia, Indonesia, Malaysia during November-March, and the Bay of Bengal and India during the monsoon. Newell and Gould-Stewart (1981) proposed these regions constitute the "stratospheric fountain," where by air enters the stratosphere from the troposphere. Recent studies show transport path plays a role in dehydration. Because air moves more quickly zonally than vertically, air in the TTL may pass through the localized cold regions, referred to as the "cold trap," before ascending into the stratosphere (Holton and Gettleman 2001). The "lagrangian cold point" describes the minimum temperature experienced by an air parcel following its transport path as it ascends from the troposphere to the

stratosphere. Studies using trajectory calculation with assimilated temperature and wind fields are able to accurately describe stratospheric water vapor mixing ratio (Fueglistaler et al. 2005). The role of convection in dehydration is also debated. While Sherwood and Dessler (2000) proposed that convective overshooting leads to stratospheric dehydration, observations suggest convection hydrates by injecting a large amount of ice mass in the lower stratosphere (Corti et al. 2008). Uncertainty in these processes motivates greater understanding of this region.

This thesis aims to better quantify deep convective influence on the TTL. Chapter 1 will proceed by formally defining the TTL, describing the tropospheric and stratospheric processes that affect its temperature and ozone composition, and providing a review of deep convective cloud observations in the TTL. Given this background information, Chapter 3 and Chapter 4 will present results that further quantify deep convective influence on this region.

1.1 Defining the Tropical Tropopause Layer (TTL)

As discussed, the TTL represents a better way to think about the transition between the tropical troposphere and the stratosphere. Figure 1.2 displays a schematic of the TTL. This region roughly spans the altitude range of 12-18 km, and is bounded from above by the CPT and from below by the level of main convective outflow (Gettelman and Forster 2002; Gettelman and Birner 2007; Fueglistaler et al. 2009). In the troposphere, the temperature decreases with height up to the level of the CPT. Above the CPT, the temperature increases with height due to short-wave ozone heating. The height and temperature of the CPT exhibits a seasonal cycle

(to be discussed later). Deep convection maintains the lapse rate in the upper troposphere near the moist adiabatic lapse rate; however, increasing stratospheric control on temperature causes the lapse rate to decrease. The point where the lapse rate diverges from the moist adiabat defines the lapse rate maximum (LRM). While deep convection can penetrate past the LRM, the LRM gives an indication of where convective influence subsides (Gettelman and Forster 2002). Within the TTL, the level of zero radiative heating (LZH) marks the shift between radiative cooling in the troposphere balancing latent heat release, and radiative heating in the stratosphere balancing adiabatic cooling from the stratospheric circulation (Gettelman and Forster 2002). Parcels above the LZH, located at ~15 km, under clear sky conditions would tend to rise into the stratosphere while parcels below it would tend to sink back down to the troposphere. Because the TTL spans the interface between the troposphere and the stratosphere, its properties are influence by both tropospheric and stratospheric processes, and clearly separating some of these influences is still a subject of debate.

1.2 Temperature Structure of the Tropical Tropopause Layer (TTL)

Figure 1.3 (5B), taken from Fueglistaler et al. (2009), shows the spatial distribution of temperature at 70 hPa (located in the stratosphere), 100 hPa (the approximate the height of the CPT), and 150 hPa (located in the troposphere) for both January and July. In the tropics, the temperature at 150 hPa is zonally symmetric, while strong meridional gradients occur in the subtropics. Moving up in altitude to the 100 hPa level, a spatial pattern in tropical temperature emerges. In

January, the lowest temperatures occur over the west Pacific and South America. In July, the lowest temperatures appear over the west Pacific and the Asian monsoon region. Here, it is also evident that January temperatures at 100 hPa are much lower than those observed in July. In the lower stratosphere (70 hPa), the quasi-stationary longitudinal structure begins to vanish. Figure 1.3 (5B) clearly shows CPT temperature is not zonally symmetric and has an annual cycle characterized by lower temperatures during boreal winter.

1.2.1 Stratospheric Influence on Tropical Tropopause Layer (TTL) Temperature

Several studies have found the extratropical wave driving of the stratospheric circulation to be important for determining the annual cycle of CPT temperature. As discussed previously, the circulation in the stratosphere is wave driven. However, the circulation is not even in the annual mean. Charney and Drazin (1961) examined conditions that are favorable for vertical wave propagation. Assuming waves are stationary, they can propagate vertically if the zonal wind ($\bar{u}$) is greater than zero and less than a critical value. Therefore, the nature of the stratospheric winds, easterly in the summer stratosphere ($\bar{u} < 0$) and westerly in the winter stratosphere ($\bar{u} > 0$), constrains vertical wave propagation to occur only in the winter stratosphere. Consequently, the winter hemisphere tends to have a stronger residual circulation (refer to Figure 1.1).

Figure 1.4, shows the annual cycle of lower stratospheric temperature for the tropics, the extratropics, and the whole globe (Yulaeva 1994). Because the temperatures in the extratropics and the tropics are out-of-phase, Yulaeva et al.

(1994) concluded that negative/positive zonal mean temperature anomalies in the tropics/extratropics during boreal winter are the result a stronger stratospheric circulation during boreal winter versus austral winter. A stronger circulation in boreal winter leads to greater adiabatic cooling in the tropics/adiabatic warming in the extratropics, consistent with the observed anomalies. Topographic differences between hemispheres cause the annual cycle in the strength of the circulation; planetary wave forcing due to orography and land-sea contrast is more prevalent in the Northern Hemisphere leading to a stronger residual circulation in Northern Hemisphere winter compared to Southern Hemisphere winter.

The strength of the residual circulation is also subject to interannual variability. Several recent studies have found El Niño- Southern Oscillation (ENSO) events to affect the strength of the residual circulation and ultimately the temperature of the TTL region (García-Herrera et al. 2006; Randel et al. 2009; Calvo et al. 2010). ENSO is an ocean-atmosphere interaction where the warm tropical sea surface temperatures (SSTs) and deep convection shift between the east and west Pacific. Their findings show that anomalous wave drag during an ENSO warm event (i.e. positive SST anomalies and stronger deep convective influence in the east Pacific) leads to a stronger residual circulation. Thus, the strength of the upwelling increases, leading to greater adiabatic cooling and a colder tropical lower stratosphere.

The annual cycle in the strength of the residual circulation has also been examined in connection with tropopause height. The tropopause height is at a minimum during boreal summer and at a maximum during boreal winter (Reid and

Gage, 1981). Because the annual cycle in the tropopause height is consistent with the annual cycle in the strength of the residual circulation, it seems the change in upwelling induces the tropopause height change. Birner (2010) found stratospheric dynamics, which leads to temperatures colder than the radiative equilibrium temperature in the tropical stratosphere and temperatures warmer than the radiative equilibrium temperature in the extratropical stratosphere, more than doubled the equator-to-pole contrast in tropopause height when compared to stratospheric radiative equilibrium. This confirms stratospheric dynamics is significant for determining tropopause height; however, it is uncertain that cooling the lower stratosphere will produce the observed height change alone. Reid and Gage (1996) suggested that lower temperatures in the upper troposphere during boreal winter destabilize the region leading to higher convective influence and mixing that results in a higher tropopause. Thus, influence of tropospheric and stratospheric dynamics becomes harder to separate.

1.2.2 Tropospheric Influence on Tropical Tropopause Layer (TTL) Temperature

Norton (2006) and Kerr-Munslow and Norton (2006) have found vertically propagating waves in the tropics forced by deep convection to be important for determining the annual cycle of CPT temperature. A model experiment presented by Norton (2006) demonstrated the response to a Gaussian heating (1000-200 hPa) centered over the equator at 180°E. The zonal mean temperature response to this imposed tropospheric heating is cooling at the 100 hPa level (> -5 K) and warming in the troposphere (> 3 K). The findings indicate the presence of a circulation

(different from the stratospheric circulation), with ascent and adiabatic cooling in the tropics and poleward meridional flow in the upper troposphere. The strongest 100 hPa cooling is centered over the tropospheric heating, consistent with observations (refer to Figure 1.3, 5B). The zonal mean temperature response to a Gaussian heating (1000-200 hPa) centered at 15°N and 180°E is weaker and shifted off the equator. The shift in heating between the equator and 15°N mimics the observed season cycle in tropical convection. Thus, they concluded that the location of the heating (i.e. tropical convection) is important for the annual cycle of CPT temperature resulting in an increase of upwelling and adiabatic cooling consistent with the seasonal cycle of tropical Rossby waves. These findings propose an alternative explanation based on large-scale tropical tropospheric dynamics for the annual cycle of CPT temperature.

Deep convective heating also directly affects CPT temperature. Holloway and Neelin (2006) noted the "convective cold top" when regressing the temperature at every pressure level with the vertically averaged temperature of the free-troposphere. Their results from a simple hydrostatic model indicated the cooling is the result of horizontal pressure gradients that extend above the heating leading to divergence aloft. Rising motion occurs in order to conserve mass, and this rising motion causes adiabatic cooling to occur. The "convective cold top" is the result of adiabatic cooling, and is a natural response to the convective heating. Folkins et al. (2008) examined temperature anomalies associated with high rainfall rates from the Tropical Rainfall Measuring Mission (TRMM) at various tropical radiosonde stations. Findings revealed a positive temperature anomaly (~1 K) located in the

upper troposphere (5-14 km) and a negative temperature anomaly (~-1 K) located in the TTL region (14-17 km). Figure 1.5, taken from Gettelman and Birner (2007), displays the January tropical temperature anomalies, the departure from the zonal mean, similar in construction to Figure 6 in Randel et al. (2003). In the Indian and west Pacific Oceans, areas with active deep convection, the temperature signal is characterized by tropospheric warming up to 150 hPa and CPT cooling. An opposite signal appears in the east Pacific where convection is suppressed due to the descending branch of the Walker circulation. These findings more clearly describe the large-scale temperature signal associated with deep convection.

Convective overshooting also affects the CPT at the meso-scale. Findings by Kuang and Bretherton (2004) show penetrative deep convection is strongly coupled to the CPT. An air parcels is considered to "overshoot" when it surpasses the level of neutral buoyancy (LNB). The LNB identifies the "level at which an air parcel, rising or descending adiabatically, attains the same density as its environment" (AMS Glossary). This means that an air parcel rising adiabatically within a convective updraft will no longer be positively buoyant above the LNB; however, if the parcel has enough energy, it will overshoot its LNB. When an air parcel overshoots the LNB, it will continue to cool adiabatically becoming colder than the environment. Detrainment and mixing of the parcels with the environment will cool the environment above the LNB. Overshooting, as well as, all processes previously described, affects the temperature of the TTL. The exact interaction of these processes is hard to determine, but is necessary in order to understand stratospheric water vapor.

1.3 Ozone in the Tropical Tropopause Layer (TTL)

Ozone concentrations are significantly higher in the stratosphere than in the troposphere, and the TTL is the location where this strong transition occurs. Figure 1.3 (5D), taken from Fueglistaler et al. (2009), shows the spatial distribution of ozone at 70 hPa (located in the stratosphere), 100 hPa (the approximate the height of the CPT), and 150 hPa (located in the troposphere) in both January and July. The transition between the tropospheric and stratospheric chemical regime is evident when comparing the 70 hPa and 150 hPa spatial distributions. The ozone concentrations at 70 hPa have values typically found in the stratosphere (>100 ppbv), while the 150 hPa ozone concentrations are more typical of the troposphere (< 100 ppbv). A seasonal cycle in ozone concentrations in the lower stratosphere (70 hPa) is also evident when comparing January and July. Ozone concentration at the CPT (100 hPa) exhibit troposphere-like concentrations (< 100 ppbv) in localized regions; in January, the lowest ozone concentrations occur over the west Pacific and South America, while the lowest ozone concentrations in July are found over the equatorial Pacific and the Asian monsoon region. The regions with low ozone concentrations at 100 hPa also are regions with the lowest CPT temperatures (refer to Figure 1.3, 5B) and a high occurrence of deep convection. Figure 1.3 (5D) shows regional and seasonal differences in ozone at the CPT, as well as seasonal differences in ozone concentration at the 70 hPa level.

1.3.1 Stratospheric Ozone Chemistry

Ozone is photochemically produced via the Chapman mechanism in the tropical stratosphere. Figure 1.6 shows a latitude-altitude cross section of the ozone number density taken from Jacob (1999). Maximum production of ozone in the tropical stratosphere occurs between 20-30 km (i.e. the ozone layer). High ozone number density in the extratropics is due to transport from the tropical stratosphere via the stratospheric circulation, indicating the distribution of stratospheric ozone is strongly influenced by dynamics.

The annual cycle in vertical velocity due to the strength of the residual circulation has an impact on ozone concentrations at the CPT. Randel et al. (2007) investigated the annual cycle of ozone above the tropopause using ozone measurements taken from the Southern Hemisphere ADditional OZonesonde (SHADOZ) dataset and the Halogen Occultation Experiment (HALOE) dataset. In Figure 1.7 (Top), a clear annual cycle in ozone at 17.5 km is evident over Nairobi, Kenya (1°S) with the lowest ozone concentrations occurring during boreal winter. Similarly, Figure 1.7 (Bottom) displays the annual cycle of ozone measured at 83 hPa and averaged over the equatorial region (10°S-10°N). Findings show that the annual cycle of ozone is mainly due to the residual vertical velocity acting on the background vertical gradient of ozone. ENSO, which affect the residual circulation, also have impacts on the ozone distribution. ENSO warm events reduce ozone concentrations in the TTL by altering upwelling in the tropical lower stratosphere (Randel et al. 2009).

1.*3.2 Tropospheric Ozone Chemistry*

While ozone concentrations are high in the stratosphere because of the Chapman mechanism, ozone concentrations in the troposphere are low with sources including transport from the stratosphere and chemical production involving NO_x. In the marine boundary layer, where water vapor mixing ratio is high, emissions of NO_x are low (sources of NO_x include fossil fuels, lightning, and biomass burning), and sufficient sunlight is present, ozone destruction occurs. Photolysis of ozone in the troposphere is a source of OH, and the following oxidation reaction (R1-R3) constitutes the main path by which ozone is destroyed in the marine boundary layer (Kley et al. 1996):

$$CO + OH \rightarrow H + CO_2 \quad (R1)$$

$$H + O_2 + M \rightarrow HO_2 + M \quad (R2)$$

$$HO_2 + O_3 \rightarrow OH + 2O_2 \quad (R3)$$

$$\text{Net: } O_3 + CO \rightarrow CO_2 + O_2$$

Another path by which ozone destruction occurs appears in the reaction below (R4), however R4 is much slower than R1 in the troposphere. The product of R4 (HO_2) causes further ozone destruction via R3 where NO_x concentrations are low:

$$O_3 + OH \rightarrow HO_2 + O_2 \quad (R4)$$

Ozone concentrations in the upper troposphere are sensitive to HO_x/NO_x concentrations and distributions. Higher NO_x concentrations in the upper tropical troposphere lead to chemical production of ozone (Folkins et al. 2002). NO reacts with HO_2, which sources include oxidation of CO/O_3 (R1-R2/R4), creating NO_2 and OH. Photolysis of NO_2 yields a free oxygen atom that combines with O_2 to produce

ozone. Ozone production is approximately 1-2 ppbv/day in the upper troposphere and the TTL (Folkins et al. 2002).

Low ozone concentrations in the tropical upper troposphere are the result of convective transport of low ozone concentrations from the surface (Kley et al. 1996; Folkins et al. 1999). Figure 1.8 shows a latitude-height cross-section of ozone mixing ratio. Low ozone concentrations near the surface at the equator result from the ozone destruction reactions summarized above. The low ozone concentrations in the upper tropical troposphere arise from transport from the surface. Further discussion of this is found in Chapter 3.

1.4 Deep Convective Clouds in the Tropical Tropopause Layer (TTL)

Tropical deep convection has a significant impact on temperature and ozone composition. Therefore, observing deep convective clouds is important for determining their impact. Liu and Zipser (2005) utilized the Tropical Rainfall Measuring Mission (TRMM) to examine the intensity of deep convective events and convection overshooting the tropopause. Figure 1.9 identifies precipitation features that overshoot various reference levels calculated using NCEP reanalysis. Their findings show that overshoots more frequently occur over land, with the Congo basin and Panama being the regions with the highest overshoots. The largest overshoot area occurs over Africa. Their findings also show that convection with a larger overshoot distance tends to have more lightning flashes observed by the TRMM Lighting Imaging Sensor (LIS) and strong ice scattering in the 85 GHz channel.

Luo et al. (2008) also examined convection overshooting the tropopause defining distinct cloud types based on cloud top temperature and height relative to the tropopause. “Cold-low” convective clouds have cloud top heights below the CPT, yet the cloud top temperature is lower than the CPT temperature. These clouds best represent undiluted adiabatic ascent. “Cold-high” convective clouds have cloud top heights above the CPT, and the cloud top temperature is lower than the CPT temperature. This cloud type likely represents a recent overshoot. The third type, “warm-high”, is associated with the dissipation stage; deep convection overshoots the tropopause and mixing with the warmer stratosphere. This results in a higher cloud top temperature when compared to the CPT temperature. These studies have provided insight into the extent to which deep convection penetrates the tropical tropopause and the properties associated with overshoots.

1.5 Outlook of Thesis

The introduction has motivated the need to understand TTL temperature and ozone. Because there is still debate on how the combination of stratospheric and tropospheric processes affects the TTL, this thesis aims to better quantify the influence of deep convection on this region. Chapter 2 describes the data utilized in this thesis. Chapter 3 then presents an analysis of ozone as an indicator of deep convection, determining TTL temperature and stratification anomalies associated with reduced ozone events. In Chapter 4, the temperature signal is further investigated in connection with deep convective clouds identified from satellite data. Finally, Chapter 5 summarizes significant findings from this thesis.

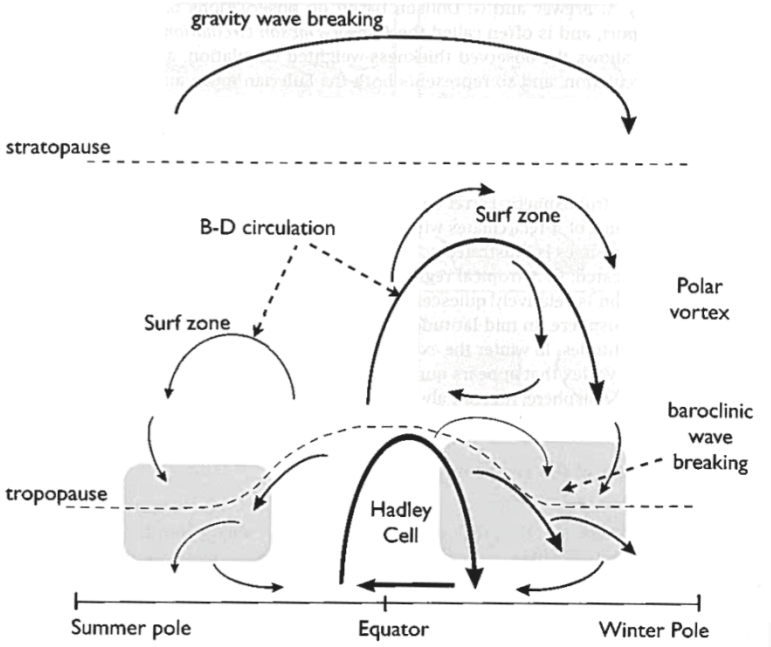

Fig. 13.14 A schema of the residual mean meridional circulation of the atmosphere. The solid arrows indicate the residual circulation (B-D for Brewer–Dobson) and the shaded areas the main regions of wave breaking (i.e., enstrophy dissipation) associated with the circulation. In the surf zone the breaking is mainly that of planetary Rossby waves, and in the troposphere and lower stratosphere the breaking is that of baroclinic eddies. The surf zone and residual flow are much weaker in the summer hemisphere. Only in the Hadley Cell is the residual circulation comprised mainly of the Eulerian mean; elsewhere the eddy component dominates.

Figure 1.1: Taken from Vallis (2006).

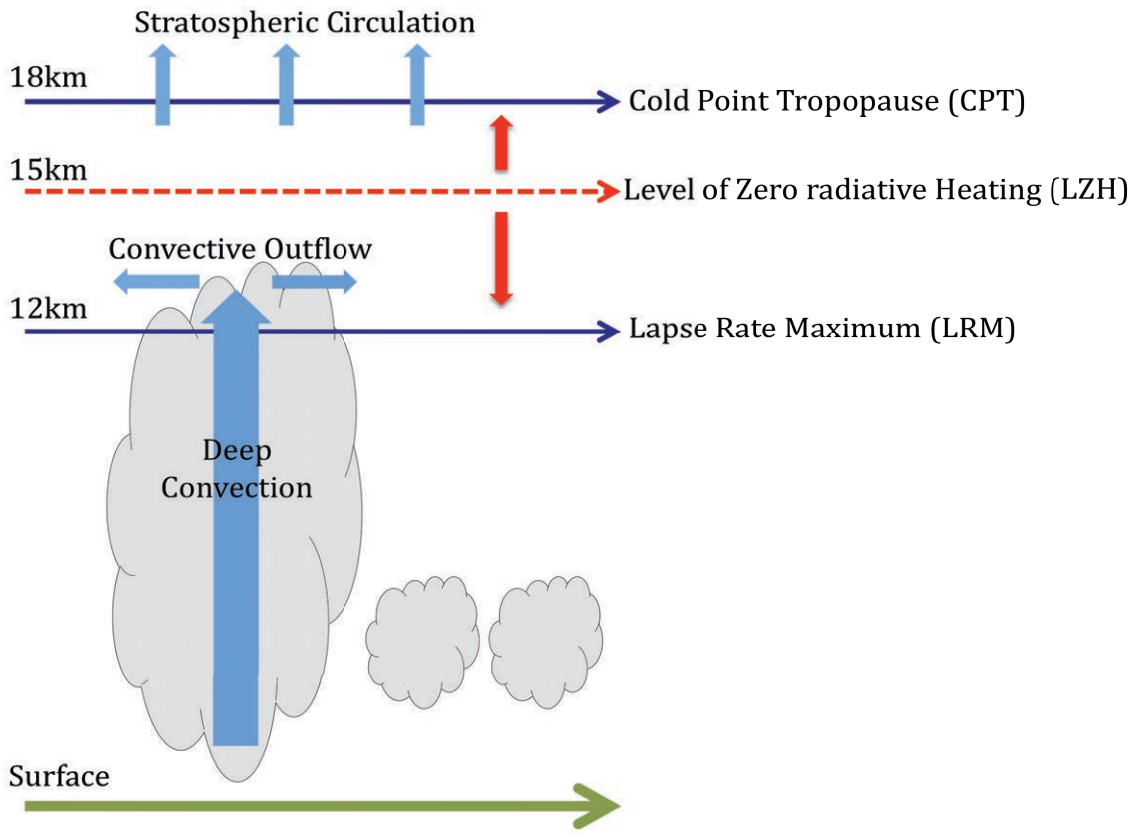

Figure 1.2: A schematic of the Tropical Tropopause Layer (TTL).

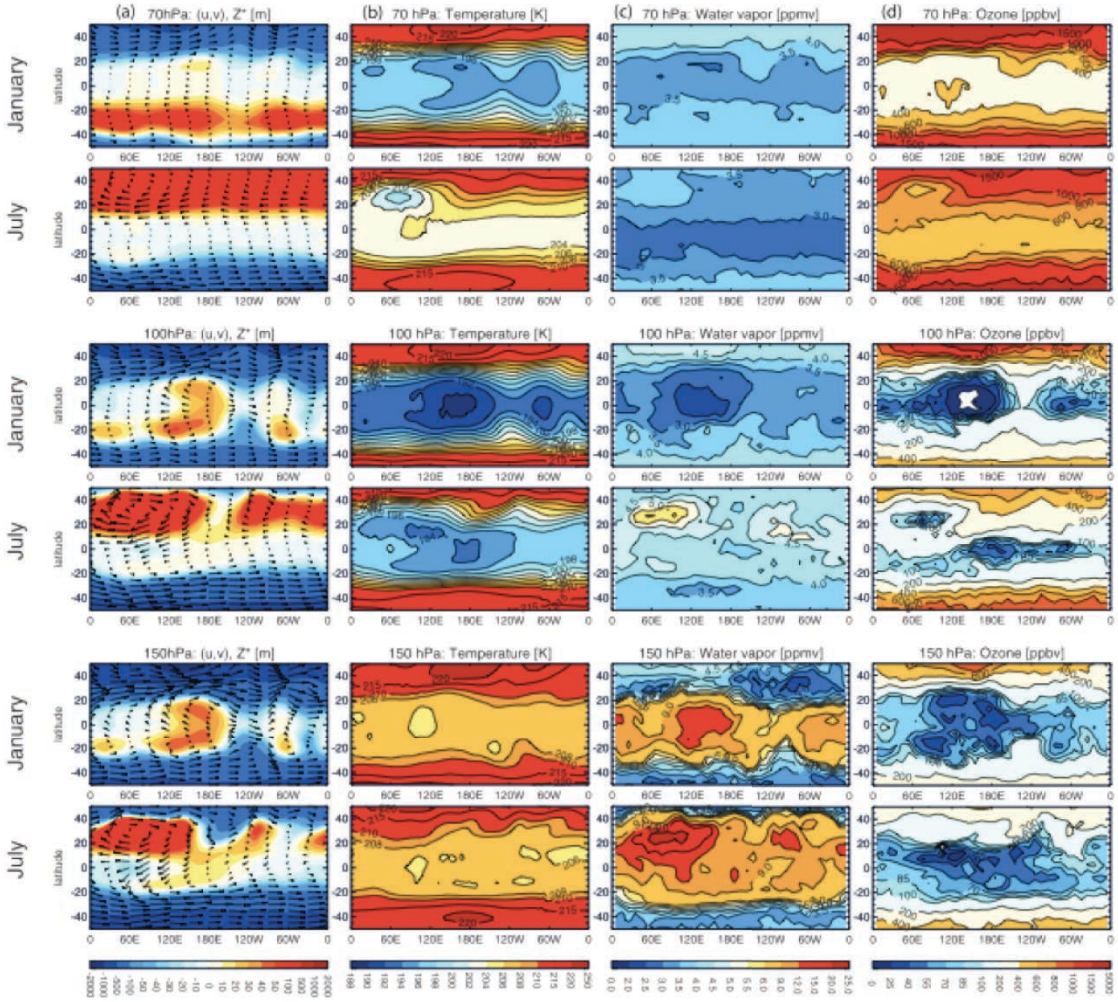

Figure 5. Maps on 150, 100, and 70 hPa of January and July mean fields. (a) Wind (vector field, arbitrarily scaled for best visual representation of flow) and geopotential height anomaly relative to 10°S–10°N mean (ERA-40, averaged 1990–2000); (b) temperature (ERA-40 [*Uppala et al.*, 2005], averaged 1990–2000); (c) water vapor (Microwave Limb Sounder (MLS)/Aura data v2.2 [*Read et al.*, 2007], January and July 2006); and (d) ozone (MLS/Aura data v2.2 [*Froidevaux et al.*, 2006], January and July 2006). Note irregular contour increments to capture full dynamic range of data; white areas indicate no valid data.

Figure 1.3: Taken from Fueglistaler et al. (2009).

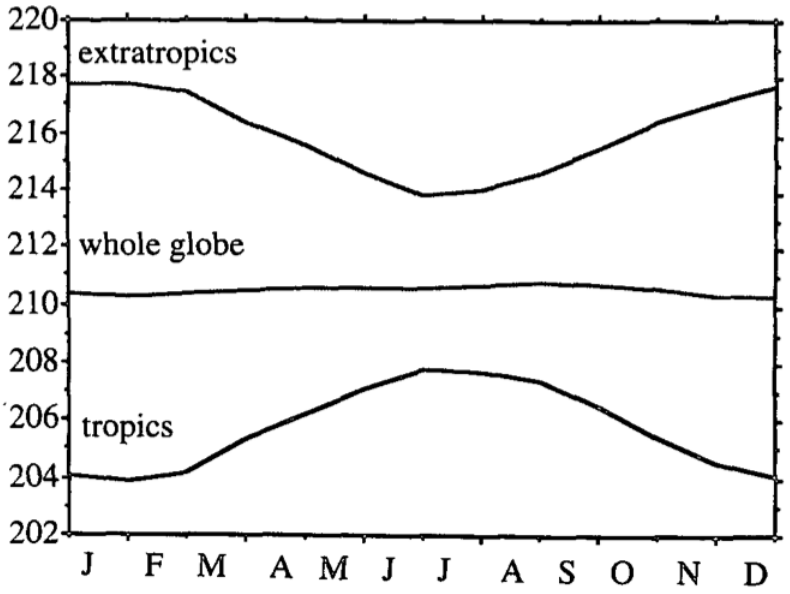

FIG. 2. Climatological mean annual march of lower-stratospheric temperature based on MSU-4 data for the period 1979–91, averaged over the tropics (30°S–30°N), the extratropics (poleward of 30°S and 30°N), and the entire globe.

Figure 1.4: Taken from Yulaeva et al. (1994).

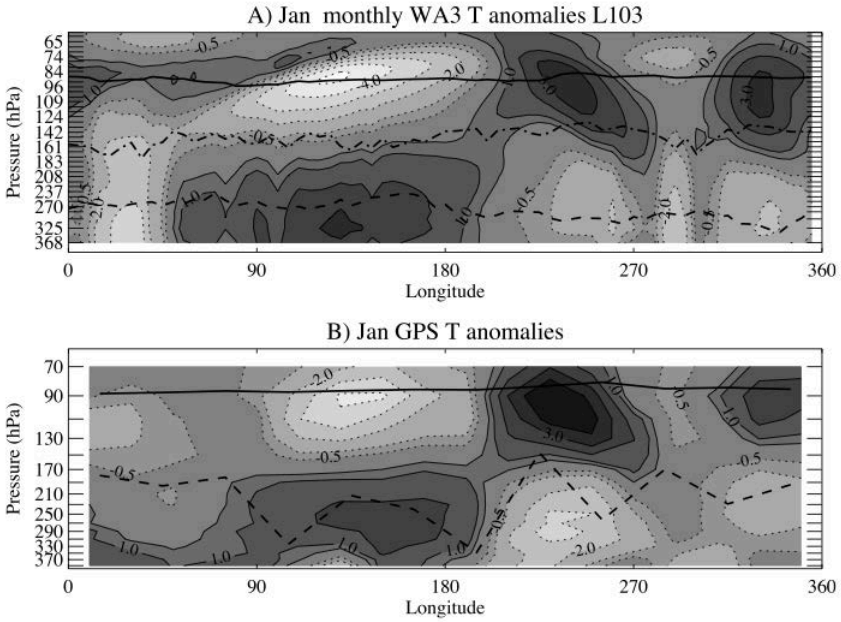

Figure 9. January tropical (25S–25N) temperature anomalies (deviations from the zonal mean) as a function of longitude and height from () WACCM L103 simulation and (b) GPS. Positive anomalies are solid; negative anomalies are dotted. Contour interval of ±1 K with ±0.5 K values added. Also shown is the meridional (25S–25N) average of the Cold Point Tropopause pressure (solid), the level of zero heating (dot-dash), and the level of the minimum lapse rate (dashed).

Figure 1.5: Taken from Gettelman and Birner (2007).

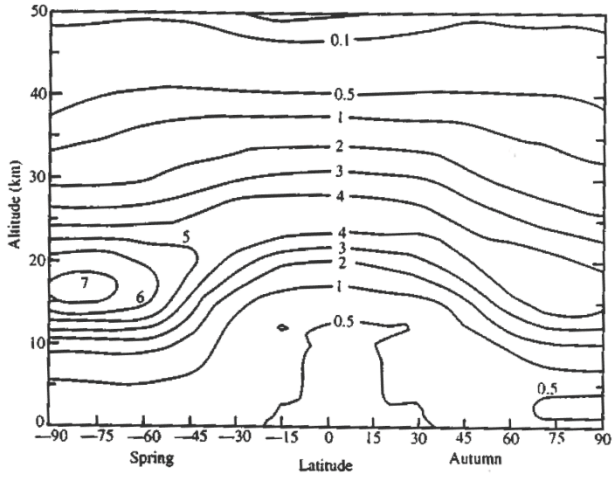

Fig. 10-1 The natural ozone layer: vertical and latitudinal distribution of the ozone number density (10^{12} molecules cm^{-3}) at the equinox, based on measurements taken in the 1960s. From Wayne, R. P. *Chemistry of Atmospheres*. Oxford: Oxford University Press, 1991.

Figure 1.6: Taken from Jacob (1999).

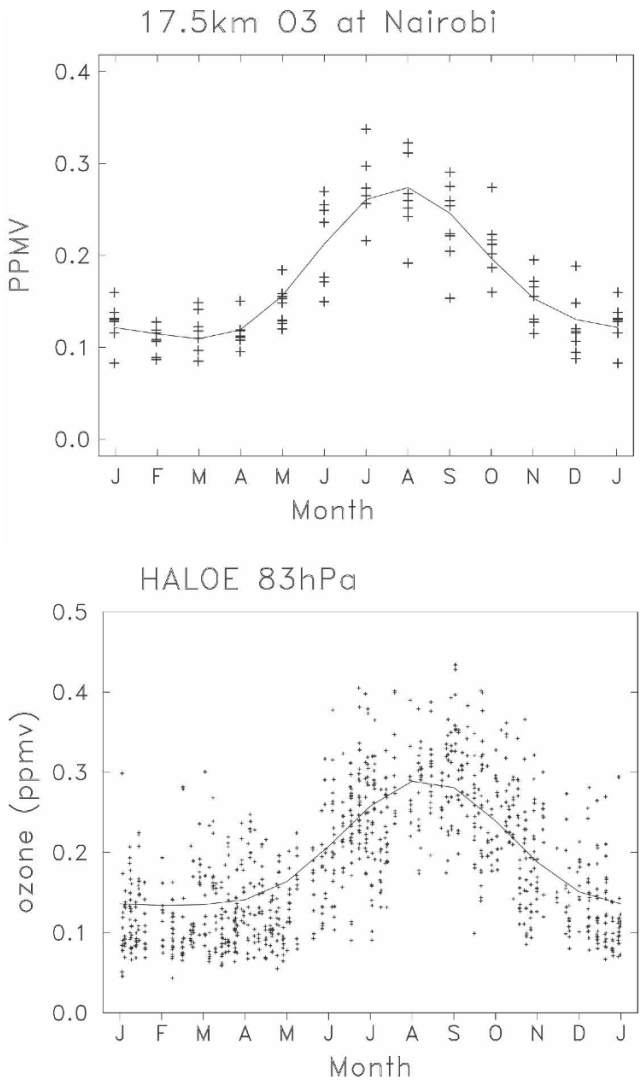

FIG. 1. (top) Ozone mixing ratio (ppmv) at 17.5 km derived from ozonesonde measurements over Nairobi during 1998–2006, plotted according to month of the observation. (bottom) HALOE ozone observations at 83 hPa over 10°N–S, combining all observations over 1992–2005. The thin line in each panel shows the harmonic seasonal cycle fit to the individual points.

Figure 1.7: Taken form Randel et al. (2007).

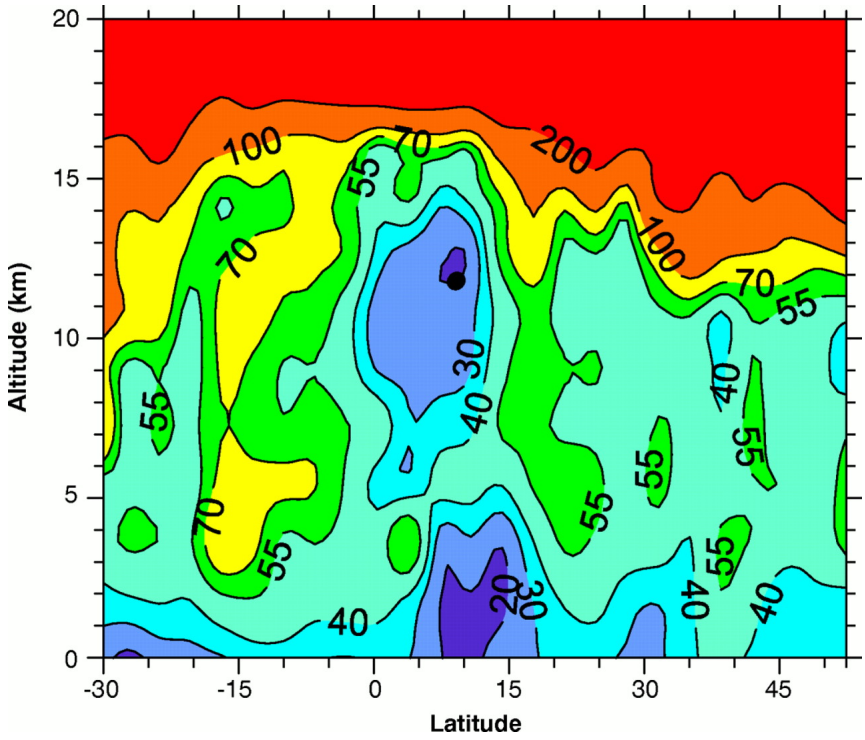

Figure 1.8: Latitude-height cross section of tropospheric ozone mixing ratio (ppbv) taken from Kley et al. (1997).

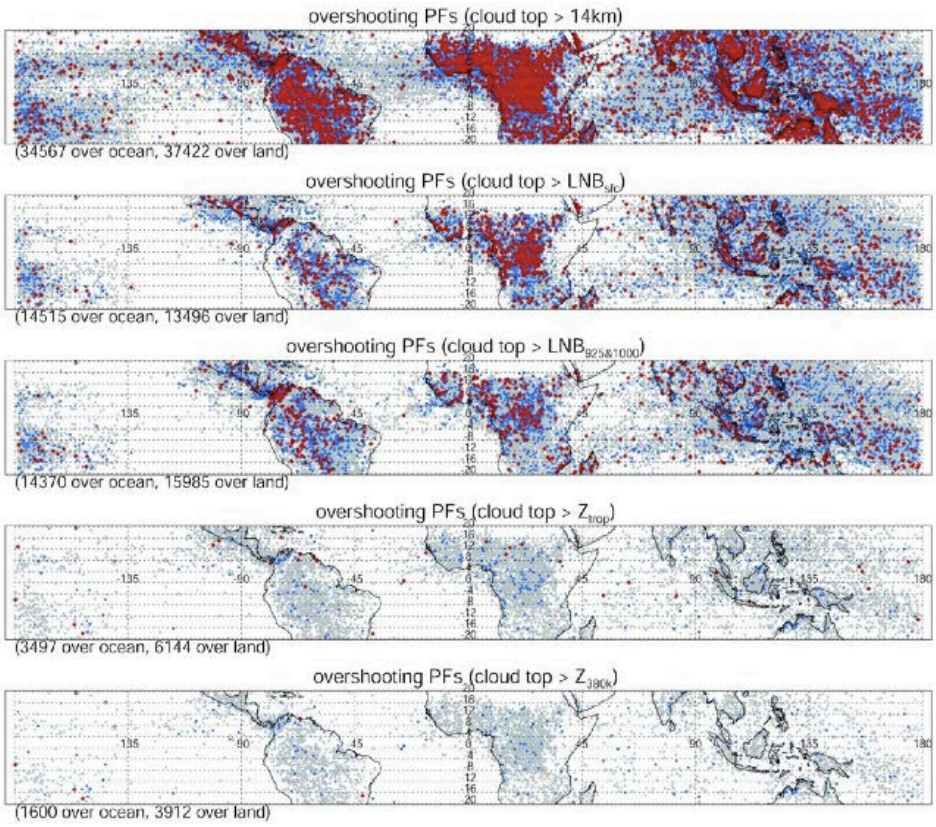

Figure 1. Location of identified overshooting PFs at 20°N–20°S using different reference heights. The PFs with over ng distance greater than 2 km are in blue, and those greater than 3 km are in red.

Figure 1.9: Taken from Liu and Zipser (2005).

2. DATA

2.1 Balloon-borne Sounding Data

This thesis presents results from the Southern Hemisphere Additional OZonesondes (SHADOZ) dataset (Thompson et al. 2003a,b). Started in 1998, the aim of the SHADOZ project is to provide consistent ozone soundings in regions lacking data. Balloon-borne electrochemical concentration cell (ECC) ozonesondes flown with standard radiosondes measure ozone via a reaction with potassium iodide. This reaction creates iodine, which when converted back to iodide by the cell releases two electrons. The partial pressure of ozone is proportional to the electron current minus a background current generated by the cell in absence of ozone. A full description of the ECC instrument can be found in Komhyr et al. (1989).

Thompson et al. (2003a) found the SHADOZ ozonesondes to have ~5% imprecision in total ozone column. However, issues have been raised concerning ECC accuracy in the tropical upper troposphere. Vömel and Diaz (2010) discuss problems with ECC background currents. They found the background current is often over estimated due to trace amounts of ozone in the air. This leads to negative ozone measurements in the upper troposphere because the background current is larger than the observed current. Kley et al. (1996) examined ECC ozonesondes launched during the Central Equatorial Experiment (CEPEX) finding a few profiles with near-zero and negative ozone concentrations. After reprocessing the

background current for this CEPEX campaign, Vömel and Diaz (2010) found that most near-zero observation of ozone mixing ratio are removed. In spite of this, ozone concentrations remained low in the upper troposphere; however, in order to avoid error, the focus of this study is shifted away from near-zero ozone events.

SHADOZ data is available for download at http://croc.gsfc.nasa.gov/shadoz/. Ten SHADOZ stations are utilized in this study: Ascension Island (7.98°S, 14.42°W); Suva, Fiji (18.13°S, 178.4°E); Hilo, Hawaii (19.4°N, 155.0°W); Watukosek, Java (7.57°S, 112.56°E); Kuala Lumpur, Malaysia (2.73°S, 101.7°E); Nairobi, Kenya (1.27°S, 36.8°E); Natal, Brazil (5.42°S, 35.38°W); Paramaribo, Suriname (5.81°N, 55.21°W); Pago Pago, American Samoa (14.23°S, 170.56°W); San Cristobal (0.92°S, 89.60°W). All stations have a few soundings per month for the time period January 1998- December 2009 (except Paramaribo which has no data in 1998, Fiji which has no data in 2006, and San Cristobal which has no data in 2009). The data fields used in this study include launch date and time, attitude (km), pressure (hPa), temperature (K), and ozone mixing ratio (ppbv).

NOAA High Resolution Radiosonde Data obtained from the SPARC data center, http://www.sparc.sunysb.edu/html/hres.html, is also utilized in this study. This dataset includes ninety-three stations that launch balloons-bourn instruments every 12 hours. In this thesis, only the data collected from Pago Pago International Airport (-14.33°S, 170.72°W) in Pago Pago, American Samoa will be used. The data fields used in this study include launch date and time, attitude (km), pressure (hPa), and temperature (K) between January 1998-December 2005.

2.2 COSMIC GPS Temperature Profiles

This study utilizes temperature data from the COSMIC/FORMOSAT-3 mission, a joint project between the National Space Organization (NSPO) in Taiwan and the University Corporation for Atmospheric Research (UCAR) in the United States (Anthes et al. 2008). The COSMIC mission uses radio occultation described extensively by Kursinski et al. (1997). Figure 2.1 presents a schematic of this technique taken from Kursinski et al. (1996). A signal sent from a GPS transmitter traveling through the atmosphere is slowed and bent due to the vertical gradient of density and a COSMIC low-earth orbiting (LEO) satellite measures the Doppler shifted frequency of the transmitted signal. The measured frequency, as well as the positions and velocities of the transmitter and receiver, are used to derive the bending angle. The vertical profile of refractive index (N) is calculated from bending angle with an Abel transform inversion. The equation below, taken from Anthes et al. (2008), shows that the refractive index depends on temperature (T; K), pressure (p; hPa), partial pressure of water vapor (e; hPa), and electron density (n_e; number of electrons per cubic meter), where f is the frequency of the transmitter (Hz).

$$N = 77.6\frac{p}{T} + 3.73\times10^{5}\frac{e}{T^{2}} + 4.03\times10^{7}\frac{n_e}{f^{2}}$$

Below 90 km, the refractive index depends only on the dry atmospheric density and water vapor density (the first two terms on the right hand side of the equation). The contribution of the water vapor to the refractive index only becomes important where temperature is greater than 250 K (Kursinski et al. 1996), which occurs between the surface and ~7-8 km in the tropics. The temperature is derived

from refractive index through integration of the hydrostatic equation. COSMIC uses data assimilation of COMSIC GPS temperature profiles and ECMWF temperature to determine water vapor mixing ratios in the troposphere, providing a temperature profile without the water vapor contribution to the refractive index in the lower tropical troposphere.

This study uses the assimilated temperature profiles, yet above ~7-8 km the temperature is essentially COSMIC GPS temperature. The profiles extend from the surface up to 40 km and have 200 m vertical resolution. They are available for download at http://cosmic-io.cosmic.ucar.edu/cdaac/products.html. Within 17 months of its launch in April 2006, the COSMIC mission achieved global coverage with ~2000 soundings per day. During the first few month of the COSMIC mission, satellites were in close proximity to one another, which allowed for assessment of their measurements. Profiles with less than 10 km tangent point separation were compared. Results showed that the highest precision is found between 8-20 km, where the standard deviation is 0.2% or ~0.5 K (Anthes et al. 2008). Radiosonde comparisons with the Challenging Minisatellite Payload (CHAMPS), which also utilizes the GPS radio occultation technique, found a ~0.5 K difference between Vaisala/Shanghai radiosondes and radio occultation refractivity profiles (Kuo et al. 2005).

Figure 2.2 (A) shows the locations of COSMIC GPS temperature soundings on December 1, 2008. The geometry of radio occultation gives a minimum number of profiles at the equator and a maximum number of profiles in the subtropics. Nevertheless, COSMIC data provides a large spatial domain unattainable by balloon-

borne sounding data. The data fields used in this study include sounding date and time, location of the sounding (° latitude, ° longitude), attitude (km), pressure (hPa), and temperature (K) between April 2006-December 2010. The temperature profiles are not vertical, but enter the atmosphere at an angle, so the location of the sounding is given as a function of altitude.

2.3 CloudSat 2B-CLDCLASS

This study utilizes the CloudSat data product, 2B-CLDCLASS, available at http://cloudsat.cira.colostate.edu/. The CloudSat mission, launched in June 2006 provides vertical distributions of hydrometeors. The Cloud Profiling Radar (CPR) operating frequency, 94-GHz, is optimal for maximum cloud detection because clouds are weak scatterers of microwave radiation. CPR footprint is 1.4 x 2.5 km, with an effective vertical resolution of 240 m. CloudSat satellite flies as a part of the A-train, trailing Aqua by less than 120s, and only 15s ahead of CALISPO. The A-train provides the opportunity to observe cloud features missed by CloudSat.

The 2B-CLDCLASS algorithm identifies eight cloud types using vertical and horizontal distribution of hydrometeors, maximum effective radar reflectivity (Z_e), precipitations signals, and ECMWF temperature profiles/surface topography height (Sassen and Wang 2008). The cloud types include cumulus (fair weather and cumulus congestus), stratocumulus, stratus, altocumulus, altostratus, nimbostratus, high clouds (cirrus, cirrocumulus, and cirrostratus), and deep convective clouds. This thesis focuses on the identification of deep convective clouds between June 2006-April 2011. Deep convective clouds produce heavier precipitation, which is

reflected by weak surface returns due to the rainfall attenuation, and have a thickness greater than 6 km. Figure 2.2 (B) shows the spatial distribution of CloudSat granules, with an orbital period of 99 minutes, on December 1, 2008. Deep convective cloud top pixels greater than 15 km are over plotted to get an understanding of the number of identified deep convective events during a typical day (discussed in more detail in Chapter 4). Cloud top imprecision may be estimated by the vertical resolution (240 m).

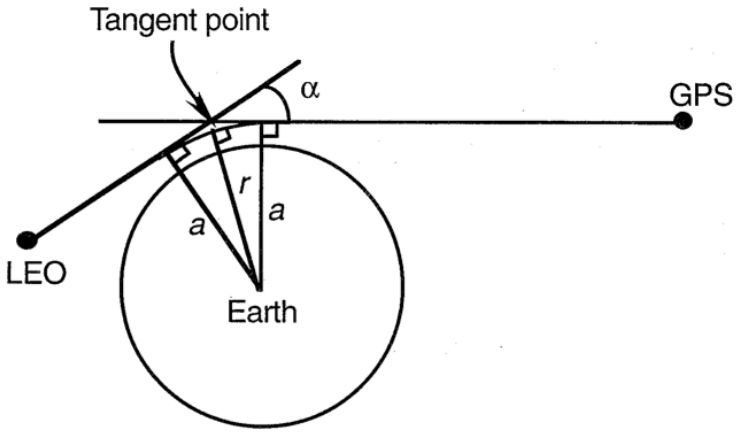

Fig. 1. Schematic of the low Earth orbiter (LEO) GPS occultation geometry of GPS-MET, defining the occultation bending angle α, the impact parameter a, and the radius to the ray periapsis tangent point, r.

Figure 2.1: Taken from Kursinski et al. (1996).

A)

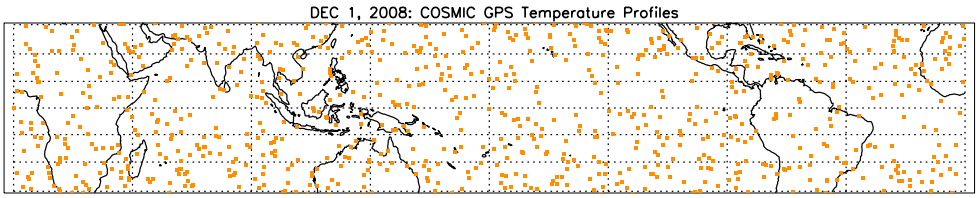

B)

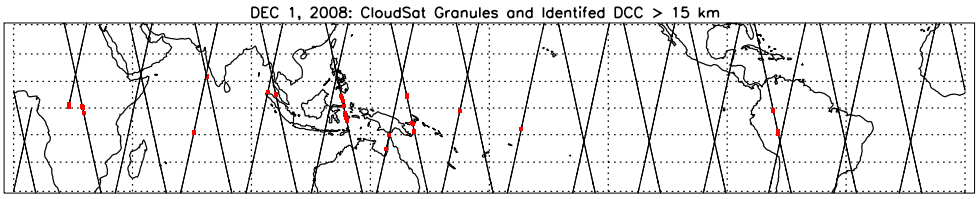

Figure 2.2: Spatial location of (A) COSMIC GPS temperature profiles and (B) CloudSat granules on December 1, 2008. Deep convective clouds identified by the 2B-CLDCLASS algorithm are plotted over the CloudSat granules.

3. EVIDENCE FOR CONVECTIVE INFLUENCE ON THE TROPICAL TROPOPAUSE LAYER (TTL) FOUND WITHIN THE SHADOZ DATASET

3.1 Tropospheric Ozone as a Tracer for Convective Transport

Several studies have examined the vertical distribution of tropospheric ozone, finding an interesting structure in the tropics. Kley et al. (1996) analyzed twenty-five vertical ozone profiles from the Central Equatorial Pacific Experiment (CEPEX). The measurements showed that near-zero ozone concentrations frequently occur in the marine boundary layer and the upper troposphere, between 10 km and the tropopause. The basis for this phenomenon is the chemical nature of tropospheric ozone. Conditions typical of a marine environment, such as low emission of nitric oxide (NO) from the surface and lightning, high levels of ultraviolet light, and high humidity, cause ozone destruction to occur at the surface (refer to Section 1.3.2). With the knowledge of this chemical process, Kley et al. (1996) suggested that very low ozone concentrations in the upper troposphere result from convective uplift of ozone from the surface. Together, these chemical and dynamical processes produce the unique vertical distribution.

A conceptual model is presented in Figure 3.1 to better visualize how ozone acts as a tracer of deep convective transport. As discussed, the marine boundary layer is characterized by low ozone concentrations (~20 ppbv) due to chemical ozone destruction. Ozone concentrations typically increase from the surface up to

the tropopause where they reach levels exceeding 100 ppbv. However, low ozone concentrations at the surface can be transported to the upper troposphere within deep convective plumes and detrained at the level of convective outflow. This causes low ozone concentrations in the upper troposphere that would not otherwise be present. Hence, low ozone concentrations in the upper troposphere can diagnose a recent convective event. However, this neglects an important dynamical process. Entrainment mixes environmental air into the convective updraft, diluting the plume. Thus, higher ozone concentrations are observed at the level of convective outflow than would be in the absence of entrainment. While Riehl and Malkus (1958) proposed undiluted ascent within deep convective 'hot towers', recent findings by Romps (2010) suggests undiluted ascent does not exist. While entrainment can disrupt the convective ozone signal, ozone is still an effective tracer for diagnosing deep convection.

Folkins et al. (1999) examined tropical ozone as an indicator of deep convection, finding a connection between upper tropospheric ozone and the lapse rate. Figure 3.2, taken from Folkins et al. (1999), shows the average profiles of ozone, temperature, and lapse rate from 108 Samoan ozonesondes launched during the Pacific Exploratory Mission (PEM). In this figure, the ozone concentrations begins to increase toward stratospheric values at approximately 14 km, and this shift between the tropospheric and stratospheric chemical regime is approximately 2-3 km below the CPT. Interestingly, the lapse rate transition in the upper troposphere, marking the point where the lapse rate diverges from the moist adiabat due a decline of deep convection, coincides with the ozone increase.

Therefore, Folkins et al. (1999) concluded that the ozone increase is associated with the reduction of convective transport from the surface. Gettelman and Forster (2002) also examined upper tropospheric ozone in connection with the lapse rate. Their study utilized satellite cloud observations, finding the average LRM height to correspond to the main influence of deep convection. Thus, they suggest the LRM can be a useful tool for investigating upper tropospheric ozone. Note that while these studies refer to the lapse rate (Γ), conventionally defined as $\Gamma = -\frac{dT}{dz}$, Figure 3.2 actually shows the vertical temperature gradient ($\frac{dT}{dz}$). This makes the LRM a maximum in the lapse rate rather than a minimum. To clarify, the plots in this study will depict the vertical gradient of potential temperature ($\frac{d\theta}{dz}$), referred to as the stratification, and the LRM will be used to describe the lapse rate maximum. Nonetheless, Folkins et al. (1999) and Gettelman and Forster (2002) established the vertical distribution of ozone to be associated with deep convective signals in the stratification.

The SHADOZ dataset, started in 1998, provides more observations at various locations throughout the tropics. Figure 3.3, taken from Folkins et al. (2002), displays the average profiles of ozone at seven locations, six of which are from the SHADOZ dataset. This study noted the average profile of ozone is "S" shaped, with the minimum ozone concentration located at the surface, a local maximum in the lower troposphere (~6.5 km), a local minimum in the upper troposphere (~12 km), and an exponential increase into the stratosphere. However, it also showed that

considerable differences exist between stations, with the lowest upper tropospheric ozone concentrations occurring at stations with active marine convection (Samoa, Fiji, Kaashidhoo, San Cristóbal). Solomon et al. (2005) also examined ozone profiles at various SHADOZ stations. Figure 3.4 (A), taken from Solomon et al. (2005), is a probability distribution displaying the likelihood that an ozone concentration at a given altitude and station will be below 20 ppbv. Figure 3.4 (B) is similar to 3.4 (A), except using SHADOZ data from 1998-2009. It clearly illustrates that the west Pacific (Fiji, Samoa, Tahiti, Java) more frequently observes low ozone concentration in the upper troposphere, referred to as reduced ozone events, when compared to other regions. The location of these reduced ozone events corresponds to a region of high sea surface temperatures and enhanced deep convection. Both studies suggest regional differences in deep convective activity are significant in determining the vertical distribution of ozone; however, they do not discuss regional differences in stratification. It is also important to consider that stations in west Pacific also more frequently observe lower surface ozone concentrations (except Java/Kuala Lumpur). Because upper tropospheric ozone concentrations are directly affected by transport from the surface, it is not surprising that lower ozone concentrations are observed in the upper troposphere at these stations.

Figure 3.4 (C) shows the likelihood that an ozone concentration at a given altitude and station will be below the average boundary layer ozone concentration, where the boundary layer is defined as a 150 mb layer starting at the surface. Java, Kuala Lumpur, and, to some extent, Nairobi, show ozone concentrations throughout the troposphere that are lower than their boundary layer concentrations. Fiji, Hilo,

and American Samoa sometimes observe upper tropospheric ozone concentrations lower than the boundary layer concentration, while the upper tropospheric ozone concentrations at San Cristóbal, Natal, Paramaribo, and Ascension are rarely lower than the boundary layer concentration. Figure 3.4 (C) presented an alternative way to view reduced ozone events, compared to Figure 3.4 (A) and (B), and motivates a deeper understanding of the associated physics.

This study expands on previous findings by focusing more closely on ozone variability at ten SHADOZ station, one of these stations being American Samoa. This station is of particular interest because of its history in the literature, the quality of its observation as it is operated by the United States, and its location in the west Pacific. In addition, US High Resolution Radiosonde Data (USRS) has a station at Pago Pago, American Samoa that is useful for determining the robustness of the SHADOZ dataset. The average annual vertical profiles of ozone for the ten stations considered are presented in Figure 3.5 (A). Profiles for stations including American Samoa, Ascension, Fiji, Natal, and San Cristóbal are "S" shaped as discussed by Folkins et al. (2002). However, profiles for the remaining stations (dashed) do not exhibit a similar "S" shape; Java is unique because its surface ozone concentration is greater than the ozone concentration in the upper troposphere, and the profiles for Hilo, Kuala Lumpur, Nairobi, and Paramaribo do not have a local minimum in the upper troposphere.

While the shape of the ozone profile differs for each station, further analysis reveals that the shape changes with season. Figure 3.5 (B) shows the average profile of ozone during the summer season at each station. The summer season is

determined by the station's latitude; June, July, August, and September defines the summer season for stations in the Northern Hemisphere, and December, January, February, and March defines the summer season for stations in the Southern Hemisphere. Stations that exhibit an "S" shape in the annual average have a more pronounced "S" shape during their summer season, with a lower surface concentration and a lower upper tropospheric minimum concentration. Hilo located at 19.4°N, is a subtropical station that does not exhibit an "S" shape in the annual average, yet shows an "S" shape during its summer season. Figure 3.6 shows the average ozone concentration in the boundary layer plotted against the average ozone concentration at 12 km, the approximate level of convective outflow, during the summer season. The ozone concentrations at 12 km tend to be double the value of the boundary layer concentration, however Kuala Lumpur and Java have a 1:1 ratio. The profiles at Kuala Lumpur and Java have higher surface concentrations compared to other stations in the west Pacific, which make the ozone profile more vertical rather than "S" shaped. The +/- one standard deviation of ozone at 12 km is also indicated in the plot. Hilo has the largest standard deviation, and high variation of ozone at 12 km may be related to greater variability in deep convective activity. Seasonal changes in ozone profiles are analyzed further by investigating each station separately to determine their unique relationship between chemistry and dynamics.

Figure 3.7 shows the average profiles of ozone divided by season for the American Samoa station. While each season demonstrates an "S" shape, changes in the height and concentration of the upper tropospheric ozone minimum are evident.

In austral summer, the upper tropospheric ozone minimum occurs at a higher altitude (~12.5 km) and lower concentration (~20 ppbv) compared to austral winter (~11 km/~30 ppbv). Surface ozone concentrations also change seasonally, with lower concentrations (~10 ppbv) occurring during austral summer compared to austral winter (~20 ppbv). Stations that display seasonal differences in "S" shape similar to American Samoa include Ascension, Fiji, Natal, Hilo, and San Cristóbal. Java, Kuala Lumpur, and Paramaribo show seasonal changes in ozone similar to that of Nairobi (Figure 3.8). These stations have little seasonal variability in surface ozone concentration, but observe changes in the height of the ozone increase. In austral summer, the ozone values begin to increase toward stratospheric levels at higher altitudes (~17 km) compared to austral winter (~15 km). Seasonal changes in ozone profiles are investigated in conjunction with the stratification to determine their relation to seasonal changes in convection.

Figure 3.9 (A) shows the stratification divided by season at American Samoa taken from the SHADOZ dataset. During austral summer, the LRM occurs at a higher altitude (~12 km) compared to austral winter (~ 10 km). This finding is consistent with the seasonal changes in the upper tropospheric ozone minimum height; when the LRM is at a higher altitude the upper tropospheric ozone minimum is at a higher altitude as well. Because the SHADOZ dataset only has a few soundings per month, Figure 3.9 (B) shows the average profile of stratification at American Samoa taken from USRS data. The LRM height tends to agree between dataset, however the largest difference is evident in the height of the stratification increase. Fiji, Hilo, and Natal show LRM changes similar to American Samoa. Because the LRM height

reflects the main influence of deep convection, the seasonal changes in the ozone minimum height at these stations appear to be affected by changes in deep convection. Figure 3.10 shows the stratification divided by season at Nairobi. In this case, the stratification increase is significantly higher during the season with the higher ozone increase. The differences in the height of the ozone increase/stratification increase reflect changes in base altitude of the TTL caused by the annual cycle of the residual circulation strength. Java and Paramaribo show stratification changes similar to Nairobi. Ascension, San Cristóbal, and Kuala Lumpur show little seasonal change in stratification, perhaps indicating little seasonal change in convection between these seasons (not shown). These findings suggest that seasonal changes in convective activity play a role in the vertical distribution of ozone by supporting more transport during a given season.

The work presented here confirms ozone as a useful tracer for diagnosing deep convection, and motivates further investigation of stratification in connection with reduced ozone events. This chapter will proceed by using stratification and temperature anomalies to better understand reduced ozone events and their affect on the TTL. Further investigation of the SHADOZ dataset is necessary to better understand TTL anomalies associated with deep convection.

3.2 Defining Reduced Ozone Events

The aim of this section is to present various diagnostics for quantifying convective influence on ozone profiles. Results are obtained for each station in order to get a sense of station differences. TTL properties associated with convectively

influenced ozone profiles will be investigated to better understand how this region is affected by deep convection.

3.2.1 The 'Ozone Minimum'

While not all SHADOZ stations display an "S" shaped average ozone profile (refer to Figure 3.5), individual profiles may contain a reduced ozone event in the upper troposphere. The need to better understand the upper tropospheric minimum in single profiles led to the development of the "ozone minimum" diagnostic (Gettelman and Forster 2002; Gettelman and Birner 2007). The approach in this study identifies the minimum ozone concentration in each profile, requiring it to be above 6.5 km, and records the height at the minimum. The height requirement is in place to ensure the event is upper tropospheric, and 6.5 km is chosen because it is the level in "S" shaped ozone profile where concentrations begin to decrease toward the upper tropospheric minimum. Figure 3.11 shows the average ozone concentration in the boundary layer plotted against the average ozone minimum concentration at each station during the summer season. The ozone concentrations at the minimum are lower than the concentrations at 12 km (refer to Figure 3.6), perhaps indicating the ozone minimum is more representative of the level of the convective outflow. The +/- one standard deviation also tends to be smaller at the ozone minimum compared to 12 km. Surprisingly, the ozone concentration at the minimum tend to be lower than the boundary layer concentration at Java and Kuala Lumpur. This suggests that upper tropospheric ozone at these stations cannot be described by transport from the surface. Frequency distributions of the ozone

minimum concentration and the ozone minimum height are presented to better understand ozone as a tracer for deep convection at each station.

Ozone minimum concentrations vary significantly between stations, however certain stations tend to behave similarly. Frequency distributions of the ozone minimum concentration for the American Samoa, Hilo, and Nairobi stations are presented in Figure 3.12. This figure also highlights the average boundary layer ozone concentrations. Stations in the vicinity of the west Pacific (Fiji, Java, Kuala Lumpur) have distributions of ozone minimum concentration similar to American Samoa. American Samoa and Fiji also have relatively low boundary layer ozone concentrations perhaps indicating direct transport from the surface. The frequency distribution for Hilo, which looks similar to that of San Cristóbal, has a larger spread of ozone minimum concentration compared to the West Pacific region, however the peak in the distribution for both American Samoa and Hilo is shifted toward lower concentrations. Ascension, Natal, and Paramaribo have distributions similar to Nairobi. These stations do not have a clear peak in ozone minimum concentration, with higher concentrations occurring more frequently.

Station differences in ozone minimum height are also evident, which can be seen in the frequency distributions at American Samoa, Hilo, and Nairobi presented in Figure 3.13. In order to better understand the connection between the ozone minimum height and the level of convective outflow, frequency distributions of the LRM height are also included in this figure. The LRM height is required to be above 6.5 km to be consistent with the ozone minimum height. It is evident that the ozone minimum height and LRM height do not peak at the same altitudes, rather for all

stations, except Paramaribo (not shown), the LRM height is shifted toward lower altitudes. This is consistent with the previous finding that the ozone minimum generally occurs just above the LRM (Gettelman and Forster 2002). Ozone minimum and LRM heights close to 6.5 km threshold are interpreted as profiles with little deep convective influence. Stations in proximity to the west Pacific (Fiji and Java, but not Kuala Lumpur) have distributions similar to American Samoa. These stations have very few ozone minimum and LRM heights close to 6.5 km, indicating strong convective influence. The frequency distribution for Hilo, which is similar to that of San Cristóbal, has a wide range of LRM height, some close to 6.5 km. These stations also have a wide range of ozone minimum height, perhaps indicating greater variability in convective transport. Kuala Lumpur, Ascension, Natal, and Paramaribo have frequency distributions similar to Nairobi. These stations have a high occurrence of ozone minimum heights close to 6.5 km, while the LRM height does not frequently occur at this level. It is surprising that the ozone minimum does not occur at the same height as the LRM, showing the ozone minimum is not always a strong indicator of the level of main convective outflow identified by the LRM. While the ozone minimum and LRM heights occur at similar levels for some stations, not all show this characteristic and require further analysis. However, the frequency distributions suggest some connection exists between the ozone minimum and the LRM. Investigating the annual cycles provides more insight into this relationship.

The annual cycles of the ozone minimum concentration and height, and the LRM height at American Samoa are presented in Figure 3.14. Lower ozone minimum concentrations (~15 ppbv) occur at higher altitudes (~12 km) during austral

summer, while higher ozone minimum concentrations (~25 ppbv) occur at lower altitudes (~ 11 km) during austral winter. This finding is consistent with the seasonal average profiles of ozone and stratification presented in Figure 3.7 and Figure 3.9. This suggests that American Samoa experiences greater deep convective influence during austral summer, consistent with its location (14.23° S) and the movement of the intertropical convergence zone (ITCZ). The annual cycle of the LRM height is determined using both the SHADOZ dataset and USRS data, which are in good agreement. Its annual cycle appears to follow that of the ozone minimum height, displaying a higher altitude LRM height during austral summer (~11.5 km) when compared to the LRM height during austral winter (~10.5 km). The annual cycles are constructed by averaging ozone minimum heights/concentrations and LRM heights identified from individual profiles. Creating an annual cycle by identifying the ozone minimum height/concentration and LRM height from monthly average profiles of ozone and stratification yield a similar result (not shown).

Other stations that display a clear annual cycle include Fiji (18.13° S) and Hilo (19.4° N), an expected result because their latitudes allow for greater seasonal change. In addition, American Samoa, Fiji, and Hilo are characterized by marine convection and pristine environments that may cause ozone to be a more effective tracer for diagnosing convection. Java (7.57° S) also displays an annual cycle, in spite of its high surface ozone concentrations. It seems that upper tropospheric ozone at Java is convectively influenced, but it does not result from direct transport from the surface. Other stations tend to have greater disagreement between the ozone minimum height and LRM height in monthly averages.

In order to get a better understanding of TTL properties associated with reduced ozone events, profiles are composited with respect to their ozone minimum height. Composite profiles of ozone, stratification, and temperature anomaly for the American Samoa station are presented in Figure 3.15. Figure 3.15 (B) shows the highest ozone minimum heights (> 90%) have higher altitude stratification increases when compared to the lowest ozone minimum heights (< 10%), but composites show little change in LRM height. A higher altitude stratification increase reflects an increase in the base height of the TTL. Temperature anomalies are also investigated in relation to the ozone minimum height in Figure 3.15 (C). The temperature anomaly profile shows strong CPT cooling accompanied by upper tropospheric warming for the highest ozone minimum heights (> 90%). This is the large-scale temperature signature of deep convection (refer to Figure 1.5), indicating the highest ozone minimum heights are convectively influenced. Fiji and Hilo show similar results, however other stations do not.

While the ozone minimum method provides some understanding of the link between the ozone and deep convection, it may not be accurately capturing the level of convective outflow because it is a point measurement and ozone may remain low over a layer in the upper troposphere. The lifetime of ozone in the upper troposphere, which can be up to a year at 10 km (Kley et al. 1996), and entrainment may also distort the ozone signal for individual convective events. Stratification and temperature anomalies associated with high altitude ozone minimums are encouraging, however differences in the monthly mean ozone minimum and LRM height motivate alternative methods for defining reduced ozone events.

3.2.2 Investigating Ozone and Stratification Anomalies

Reduced upper tropospheric ozone events have very low ozone concentrations with respect to the mean; therefore, ozone anomalies may be a useful way to view these events. In this section, ozone anomalies in the vicinity of the level of deep convective outflow are investigated to better understand the associated stratification and temperature fields. In order to obtain the ozone anomalies, each ozone profile is deseasonalized, by subtracting the average daily interpolated ozone profile, and standardized, by subtracting the mean and dividing by the standard deviation. At each 50 m interpolated level between 10-22 km, the ozone anomalies are composited. Ozone anomalies less than one standard deviation below the mean make up the negative anomaly composite, and ozone anomalies greater than one standard deviation above the mean make up the positive anomaly composite. This threshold is used to ensure a large enough sample size for each composite group. The stratification and temperature profiles associated with each composite group are deseasonalized, by subtracting the average daily interpolated profile, and averaged. Patterns in the composite stratification and temperature fields are investigated.

Figure 3.16 displays the average stratification anomaly for the negative anomaly composite contoured as a function of the height at which the ozone anomaly is taken and height for the American Samoa station. This figure shows that the stratification at 15 km is anomalously low when ozone anomalies between 12-18 km are negative. This response is due to increases in the LRM height, which corresponds to an increase in the TTL base altitude, associated with stronger deep

convective influence. Simply, this means the stratification remains lower at higher altitudes. Opposing stratification anomalies are found above and below the height of the ozone anomaly in the lower stratosphere. This is caused by vertical motion; potential temperature and ozone are quasi-passive tracers, and vertical advection acting on their background gradient will cause the observed statification anomalies (refer to Figure 3.17). An opposite signal is evident in the positive anomaly composite (not shown).

Figure 3.18 displays the average temperature anomaly for the negative anomaly composite contoured as a function of the height at which the ozone anomaly is taken and height at American Samoa. Here, a convective temperature signal is observed, with upper tropospheric warming accompanied by CPT cooling for ozone anomalies between 12-18 km. The strongest signal occurs for ozone anomalies at ~16 km. Cooling at the height of the ozone anomaly is also a signature of the plot caused by vertical advection (refer to Figure 3.17). An opposite signal is evident in the positive anomaly composite (not shown). The figures presented here suggest the negative anomaly composite (between 12-18 km) is made up of convectively influenced profiles; deep convection, which triggers the transport of reduced surface ozone concentrations to the upper troposphere, also changes the stability and temperature of the TTL. Because stratification and temperature anomalies appear convectively influenced over a wide range of ozone anomaly heights (between 12-18 km), reduced ozone events manifest themselves within this entire layer; however, the strongest convective signal is evident for highest ozone anomalies (>15km).

Because stratification remains lower in the upper troposphere for convectively influenced profile, stratification anomalies may also be a useful way to determine deep convective influence. Figure 3.19 is similar in construction to the previous plots; however, instead of examining the ozone anomaly in the upper troposphere, the stratification anomaly is investigated. Examining the temperature signal in connection with stratification anomalies is useful because it does not require ozone data. Figure 3.19 (A) shows the average temperature anomaly for the negative anomaly composite contoured as a function of the height at which the stratification anomaly is taken and height at the American Samoa SHADOZ station. Figure 3.19 (B), is the same plot as 3.19 (A) except that it uses the USRS data at American Samoa. The dataset shows similar results, confirming the usefulness of the SHADOZ dataset. Opposing temperature anomalies found above and below the height of the stratification anomaly is expected locally (refer to Figure 3.20); however, a deep layer convective temperature signal, with warming between 5- 13 km and cooling between 14-20 km, is evident for stratification anomalies between 13-17 km, which cannot be explained as the local signal. The opposite signal is seen for the positive anomaly composite (not shown). These figures suggest stratification anomalies in the upper troposphere are the result of deep convection.

Other stations that display similar composite anomaly profiles include Fiji and Hilo. These stations also showed convective influence for high altitude ozone minimum heights discussed in the previous section. Stations that do not appear to have convectively influenced stratification and temperature fields in the negative

anomaly composite may not experience the convective influence that these stations do, and greater variability in convection may lead to distorted convective signals.

An investigation of ozone and stratification anomalies effectively reveals composition, stratification, and temperature changes in TTL region resulting from deep convective events and promotes further study of the convective influence on this region. The results show that ozone and stratification anomalies at higher altitudes (>15 km) most effectively reveal deep convective temperature signals. Because the LRM rarely occurs at this level, and the fact that there are inconsistencies between the LRM height and the ozone minimum height, other measures of deep convection are investigated to better understand ozone as a tracer for deep convection.

3.2.3 The "Ozone Mixing Height"

The motivation for the "ozone mixing height" diagnostic comes from the Level of Neutral Buoyancy (LNB) (refer to Section 1.2.2). The LNB offers a useful way to quantify the upper extent of deep convective influence because it defines the level that a parcel rising adiabatically within a convective updraft will no longer be positively buoyant; once a parcel reaches this level, it will detrain and mix with the environment. Frequency distributions of the LNB at American Samoa computed from the SHADOZ dataset and USRS data are presented in Figure 3.21. The peak of LNB distribution at American Samoa is ~14 km, much higher than the peak of the LRM height distribution, ~12 km (refer to Figure 3.13). Differences appear in the LNB distributions for the different datasets as well. The LNB obtained using the

USRS data are higher than those found using SHADOZ dataset. However, greater agreement is seen when similar time periods (1998-2005) are used. Nonetheless, the LNB for at American Samoa is concentrated above 10 km, with few low altitude LNBs indicating strong convective influence at this station.

Because low ozone concentrations at the surface have the potential to be mixed up to LNB via deep convective updrafts, this parameter may be thought of as an upper bound for vertical ozone mixing. Ideally, the ozone concentrations at the LNB should be representative of ozone that is transported from the boundary layer if convective updrafts are undiluted. Figure 3.22 (Top) shows the frequency distributions of the ozone concentration at the LNB and in the boundary layer for the American Samoa station. Overlap exists between the distributions indicating that convective mixing that penetrates to up to the LNB may be undiluted. To quantify the overlap, a cumulative distribution is presented in Figure 3.22 (Bottom). It shows that approximately 75% of boundary layer ozone concentrations are less than 20 ppbv, while only 25% of ozone concentrations at the LNB are below 20 ppbv. While boundary layer concentrations are not entirely representative of ozone concentrations at the LNB, identifying the height of ozone concentrations similar to the concentrations observed at the LNB may give some indication of convective influence.

The ozone mixing height is defined as the highest altitude in a profile where ozone is below a given threshold concentration. At each station, threshold concentrations are determined by averaging ozone concentrations at the LNB

during each season. An ozone mixing height is determined for each profile and then compared to the LNB.

Frequency distributions of ozone mixing height and the LNB for American Samoa, Ascension, and Hilo are presented in Figure 3.23. For the American Samoa station, the LNB most frequently occurs between 10-15 km. The ozone mixing height for this station displays a frequency distribution similar to the LNB, however the distribution of ozone mixing height is shifted toward higher altitudes. The frequency distributions in the west Pacific (Fiji, Java, Kuala Lumpur) as well as Paramaribo and Natal look similar to that of American Samoa. The frequency distribution of the LNB at Ascension is bimodal, showing a greater number of LNBs close to the surface. Low altitude LNBs indicate a number of profiles that do not exhibit the potential for deep convection. And, consistent with the LNB, the distribution of ozone mixing height at Ascension is bimodal as well. The distribution for Ascension looks similar to that of San Cristóbal. This suggests these stations experience greater variability in deep convention. The frequency distribution of the LNB at Hilo is shifted toward lower altitudes, with few LNBs found above 10 km. However, ozone mixing height does not follow a similar distribution. The distribution at Nairobi is similar to Hilo.

Similar to the method used for the ozone minimum (refer to Figure 3.15), profiles are composited with respect to their ozone mixing height. Composite profiles of ozone, stratification, and temperature anomaly for the American Samoa station are presented in Figure 3.24. Figure 3.24 (B) shows significant stratification changes between composite groups. The highest ozone mixing heights (> 90%) have

a higher altitude stratification increase, indicating greater deep convective influence and a higher TTL base. It is also evident in Figure 3.24 (C) that the highest ozone mixing heights (> 90%) have the strongest convective signal (CPT cooling/ upper tropospheric warming), and the lowest ozone mixing heights (< 10%) have an opposing signal. It is interesting to note that while there is a strong temperature anomaly at 17 km, the height of the CPT does not change between composite groups (not shown). Rather, the sharpness of the CPT increases for the highest ozone mixing heights. Fiji, Hilo, Kuala Lumpur, Paramaribo, and Java exhibit similar structure in the stratification composites, while Fiji, Hilo, and Java also show similar structure in temperature anomaly composites. These figures reveal that using the LNB in conjunction with ozone effectively reveals stratification and temperature changes associated with deep convection. While some discrepancy exists between the LNB and the ozone mixing height, in principle, we feel that using that LNB in connection with ozone is a better way to quantify deep convection when compared to the ozone minimum, and the prominent temperature and stratification signals found when compositing confirms this.

3.3 Concluding Remarks

Work presented in this section demonstrates that various methods are able to show deep convective signatures in stratification and temperature associated with reduced ozone events. Plots of stratification and temperature anomaly composited with respect to their ozone minimum height (Figure 3.15) and ozone mixing height (Figure 3.24) reveal deep convective signals. However, in comparing

temperature fields for equal sample size, ordering highest to lowest ozone minimum/ozone mixing heights, it is evident the ozone mixing height has stronger convective signals. Figure 3.25 displays the temperature anomaly composites for both the ozone mixing height and the ozone minimum at the American Samoa station. Here, the ozone mixing height composites have a stronger convective signal for the highest composite group. Other composite groups also have more distinct signals when looking at the ozone mixing height. These results suggest that using the LNB in connection with vertical ozone profile is most effective for understanding the extent to which each profile experiences deep convective influence. This differs from previous studies that focus solely on the ozone minimum. Also, this study found both stratification and temperature to have a deep convective signal associated with the reduced ozone events. The large temperature anomalies found here motivate further investigation of the convective influence on TTL temperature using alternative datasets.

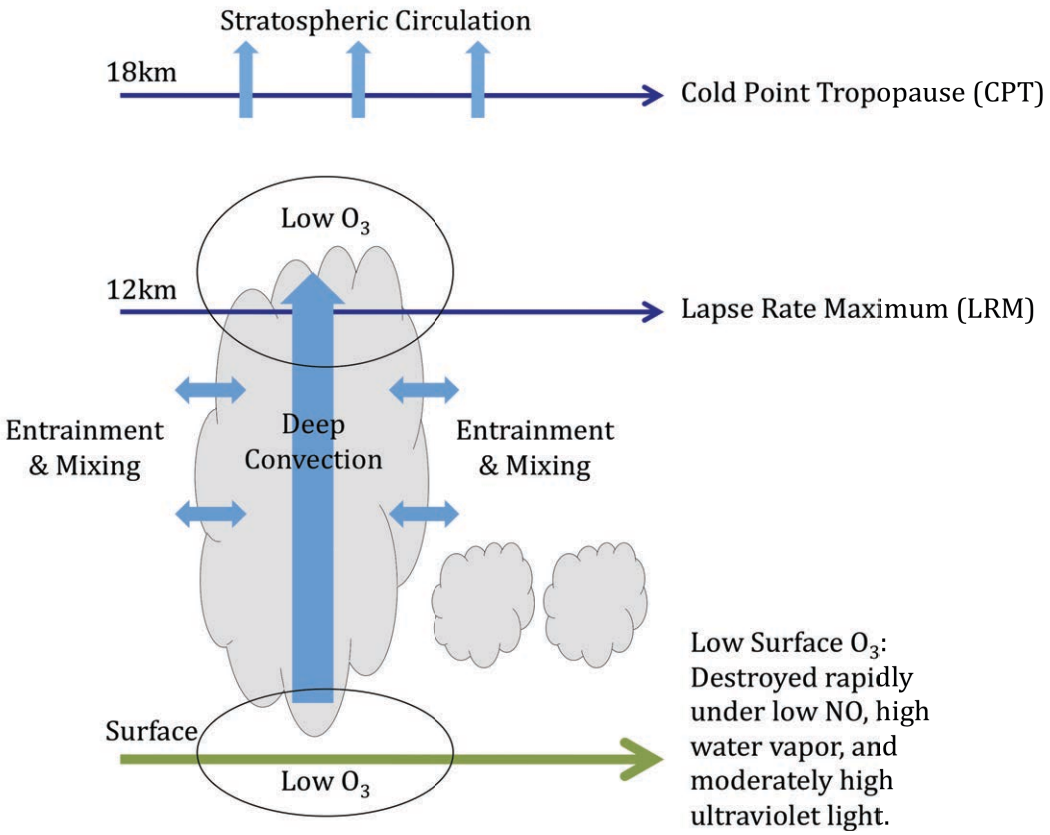

Figure 3.1: A conceptual model for understanding ozone as a tracer of deep convection. Low ozone concentrations near the surface can be transported to the upper troposphere within deep convective updrafts and detrained at the level of deep convective outflow. Entrainment and mixing can dilute the updraft, distorting the convective ozone signal.

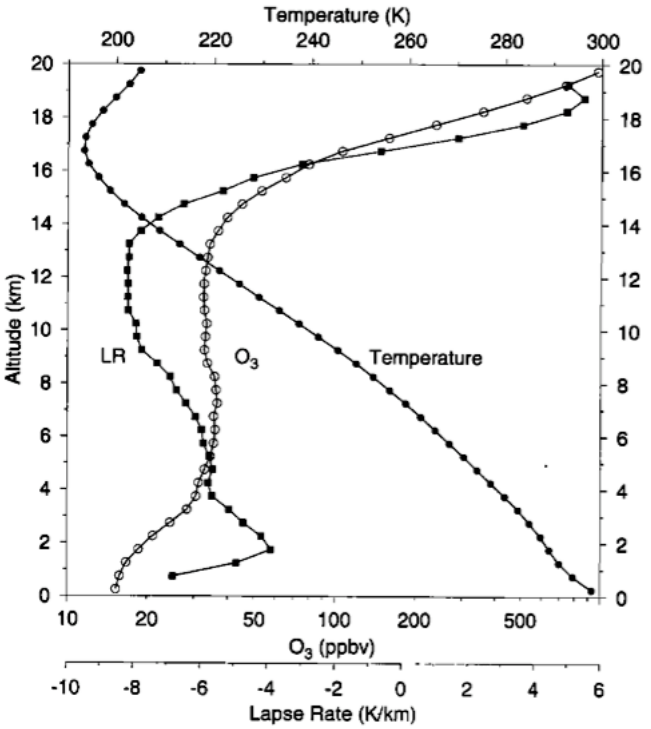

Figure 2. Average profiles of temperature, O_3, and lapse rate(LR) from all 108 Samoan ozonesondes.

Figure 3.2: Taken from Folkins et al. (1999).

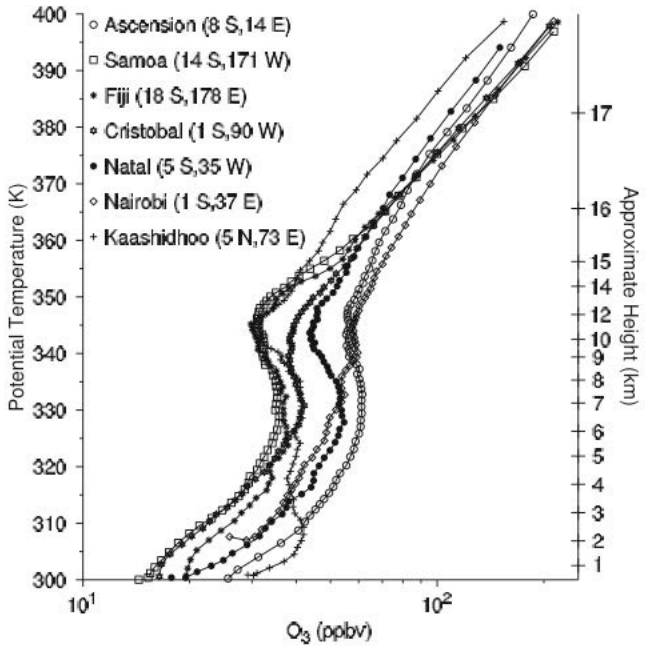

Figure 1. The mean annual dependence of ozone mixing ratio on potential temperature at Ascension (118), Samoa (175), Fiji (114), Cristóbal (131), Natal (68), Nairobi (132), and Kaashidhoo (53), where the number given in parentheses is the number of ozonesondes used at each location to construct the climatology. The Kaashidhoo profile is from ozonesondes launched during January–March. Latitude and longitude coordinates of each location are shown.

Figure 3.3: Taken from Folkins et al. (2002).

A)

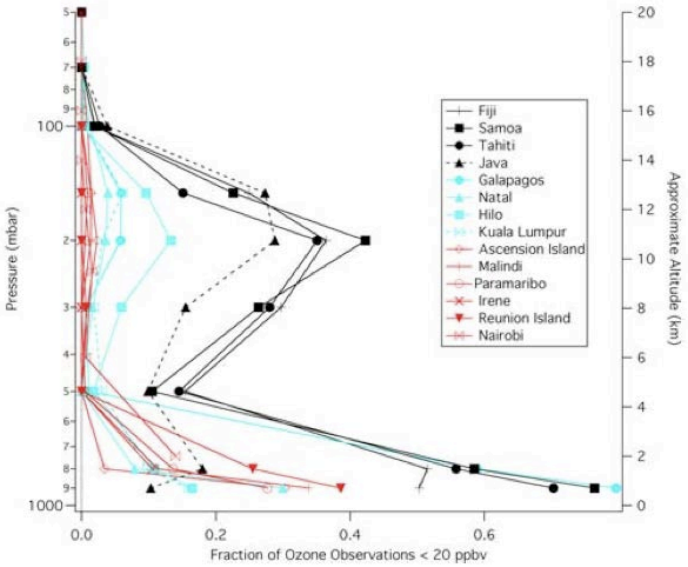

Figure 3. Vertical profile of frequency of occurrence of ozone mixing ratios below 20 ppbv at tropical ozonesonde stations, for the period from 1998–2004.

B)

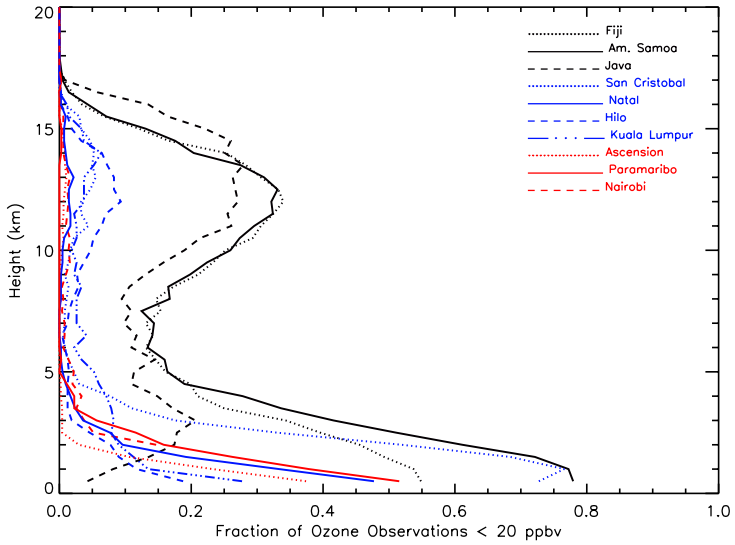

C)

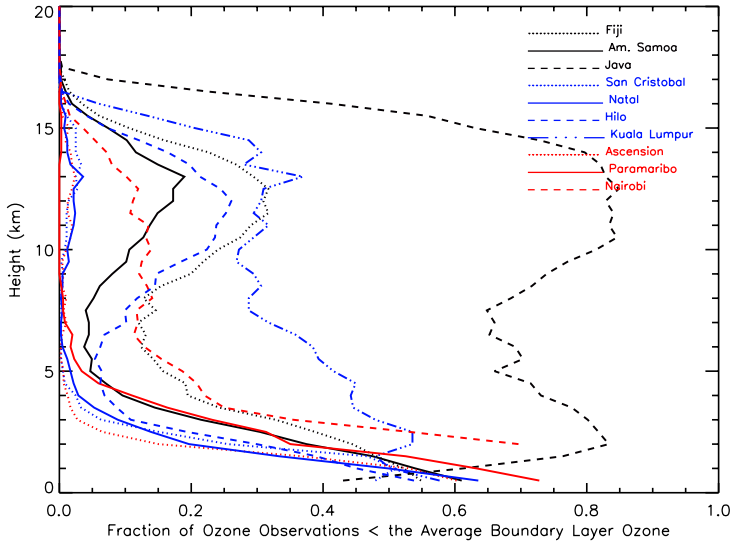

Figure 3.4: The vertical profile of frequency of occurrences of ozone mixing ratios (A) less than 20 ppbv for the time period 1998-2004, taken from Solomon et al. (2005), (B) less than 20 ppbv for the time period 1998-2009, and (C) less than the average boundary layer ozone mixing ratio at various SHADOZ stations.

A)

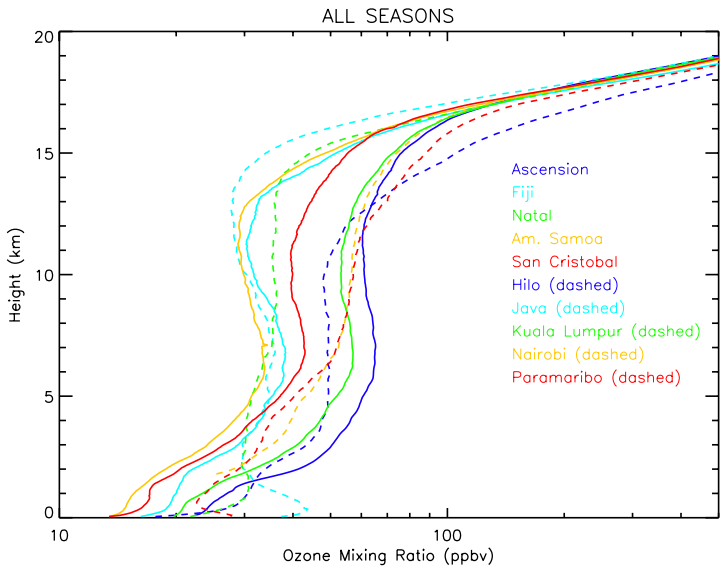

B)

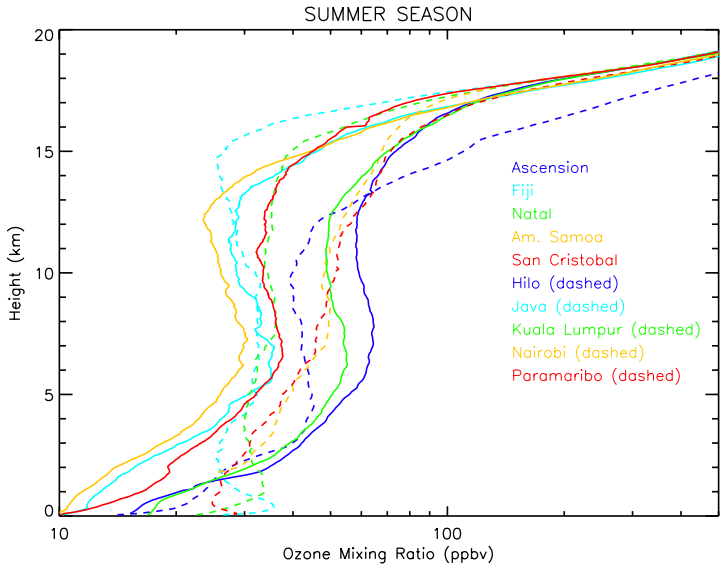

Figure 3.5: Vertical profiles of ozone at ten SHADOZ stations averaged for (A) all seasons and for the (B) summer season. Summer season depends on the stations latitude: June, July, August, and September for station in the Northern Hemisphere, and December, January, February, and March for stations in the Southern Hemisphere. Dashed profiles represent profiles that do not have the typical "S" shape described by Folkins et al (2002) in the annual average.

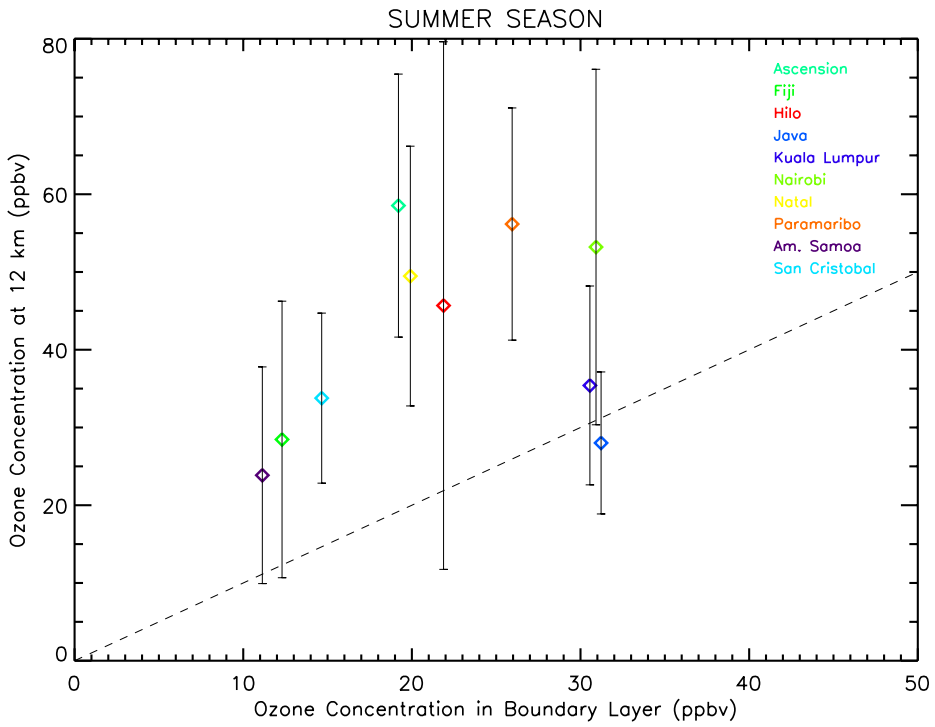

Figure 3.6: A scatter plot of average boundary layer ozone concentration plotted against the average ozone concentration at 12 km for each station. Error bars indicate +/- one standard deviation of the ozone concentration at 12 km. The 1:1 line appears as dashed.

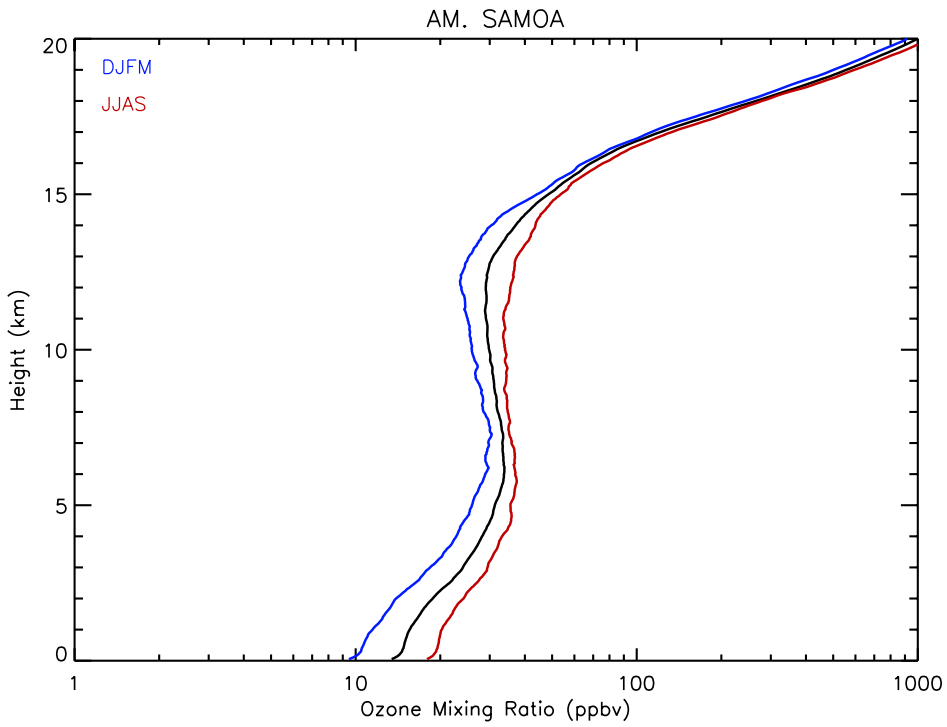

Figure 3.7: The average profile of ozone for all seasons (black) and divided by season at American Samoa (14.23°S). December, January, February, and March (DJFM, blue) make up the summer season. June, July, August, and Sept (JJAS, red) make up the winter season.

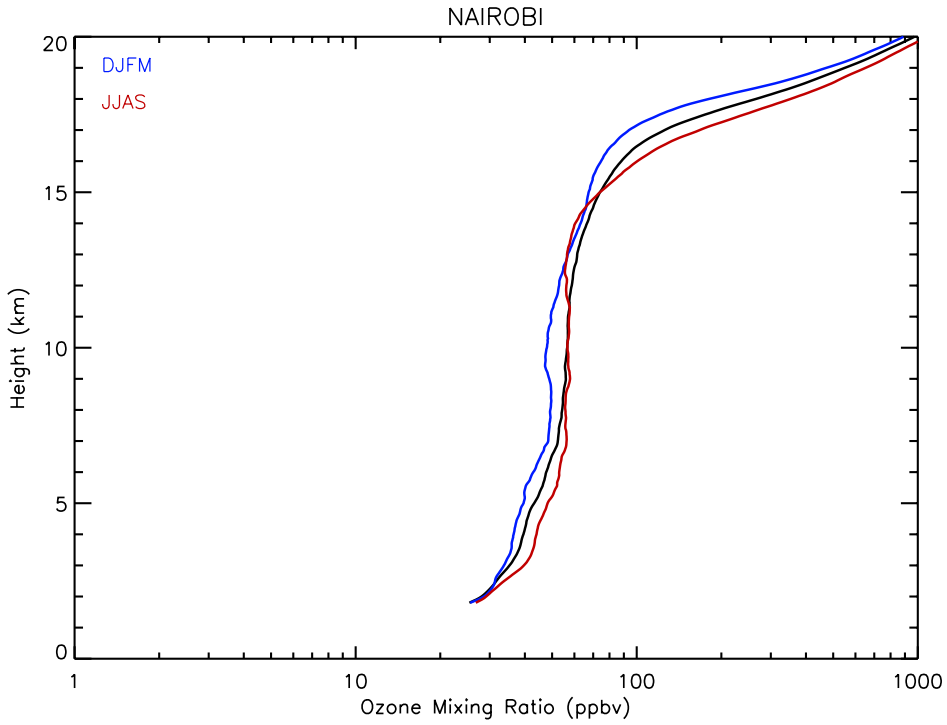

Figure 3.8: The average profile of ozone for all seasons (black) and divided by season at Nairobi (1.27°S). December, January, February, and March (DJFM, blue) make up the summer season. June, July, August, and Sept (JJAS, red) make up the winter season.

A)

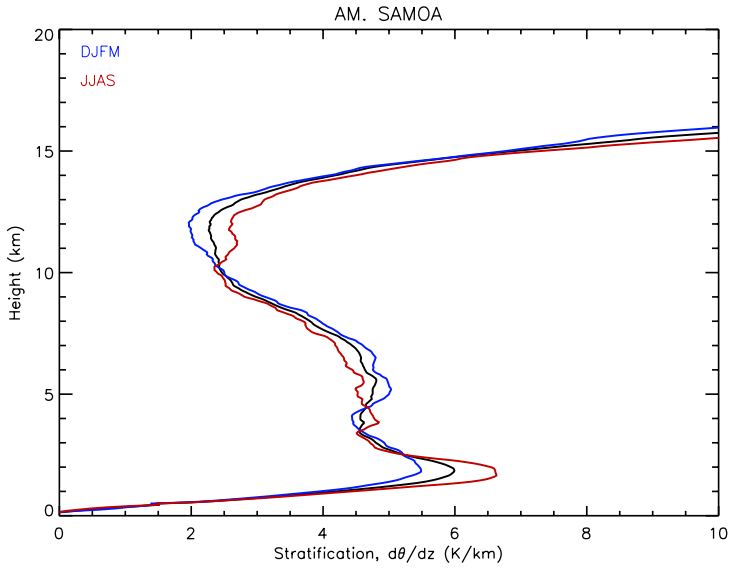

B)

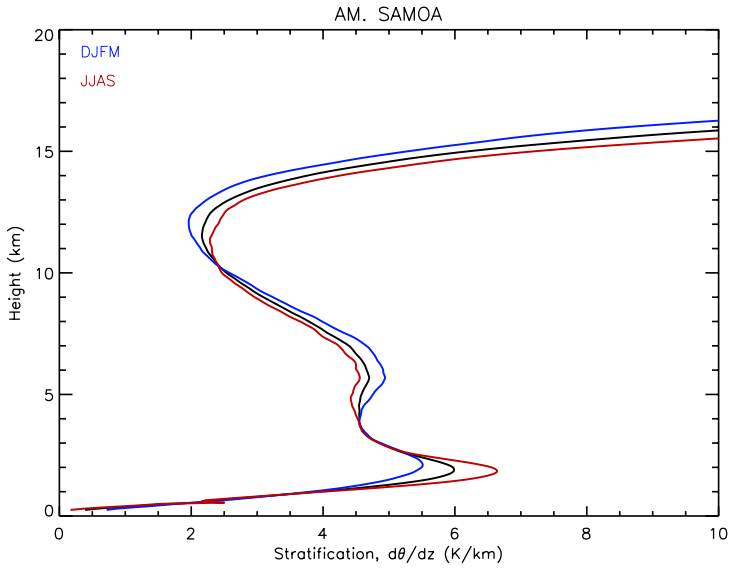

Figure 3.9: The average stratification profile for all seasons (black) and divided by season at American Samoa (-14.23°S) taken from the (A) SHADOZ dataset and (B) US High Resolution Radiosonde Data. December, January, February, and March (DJFM, blue) make up the summer season. June, July, August, and Sept (JJAS, red) make up the winter season.

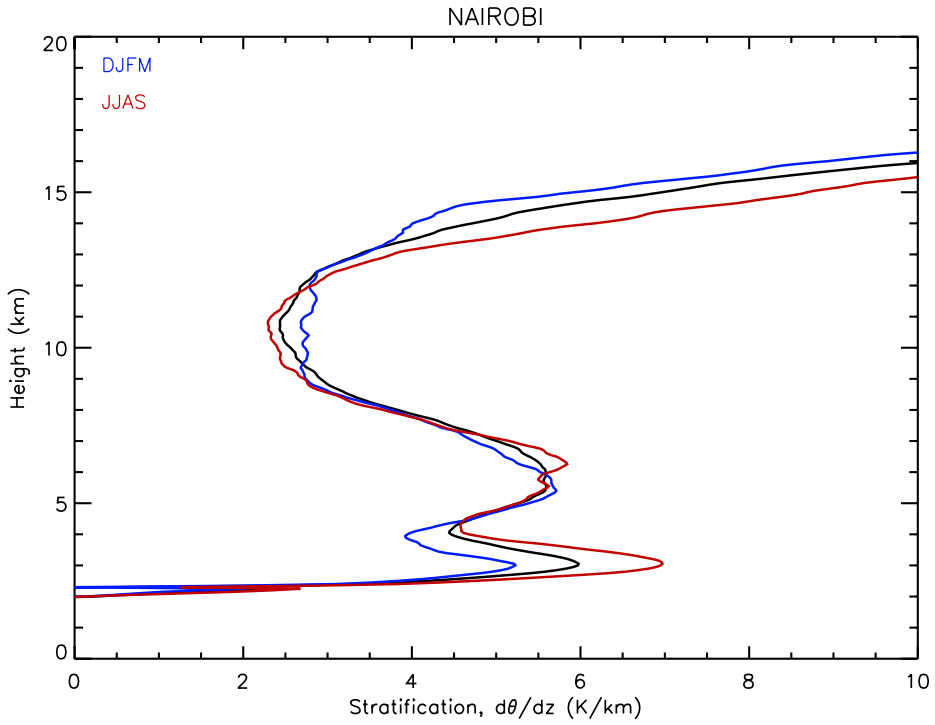

Figure 3.10: The average stratification profile for all seasons (black) and divided by season at Nairobi (1.27°S). December, January, February, and March (DJFM, blue) make up the summer season. June, July, August, and Sept (JJAS, red) make up the winter season.

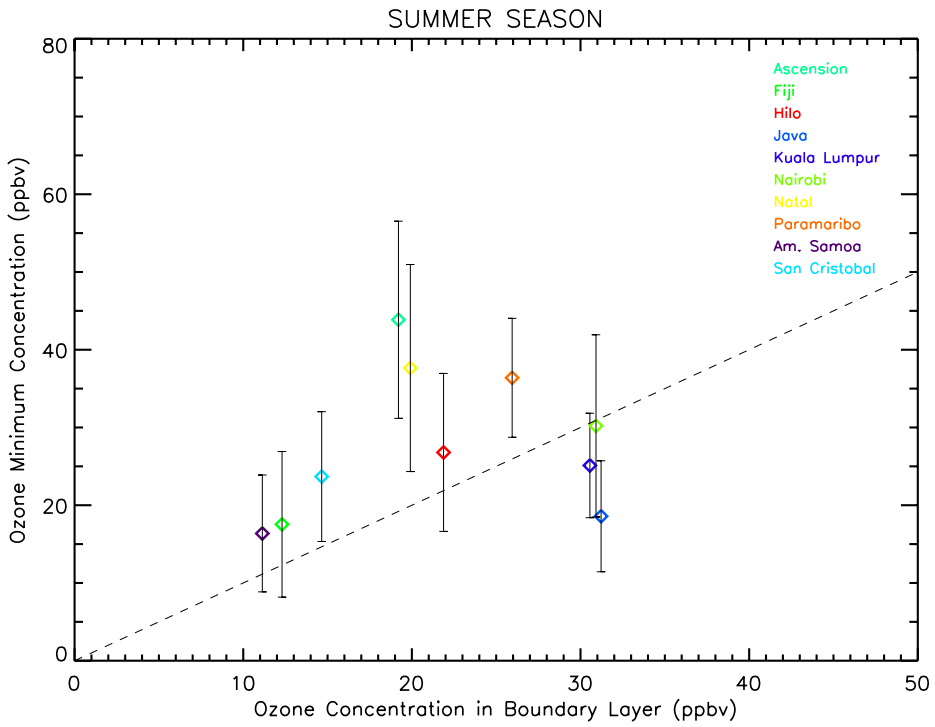

Figure 3.11: A scatter plot of average boundary layer ozone concentration plotted against the average ozone minimum concentration for each station. Error bars indicate +/- one standard deviation of the ozone minimum concentration. The 1:1 line appears as dashed.

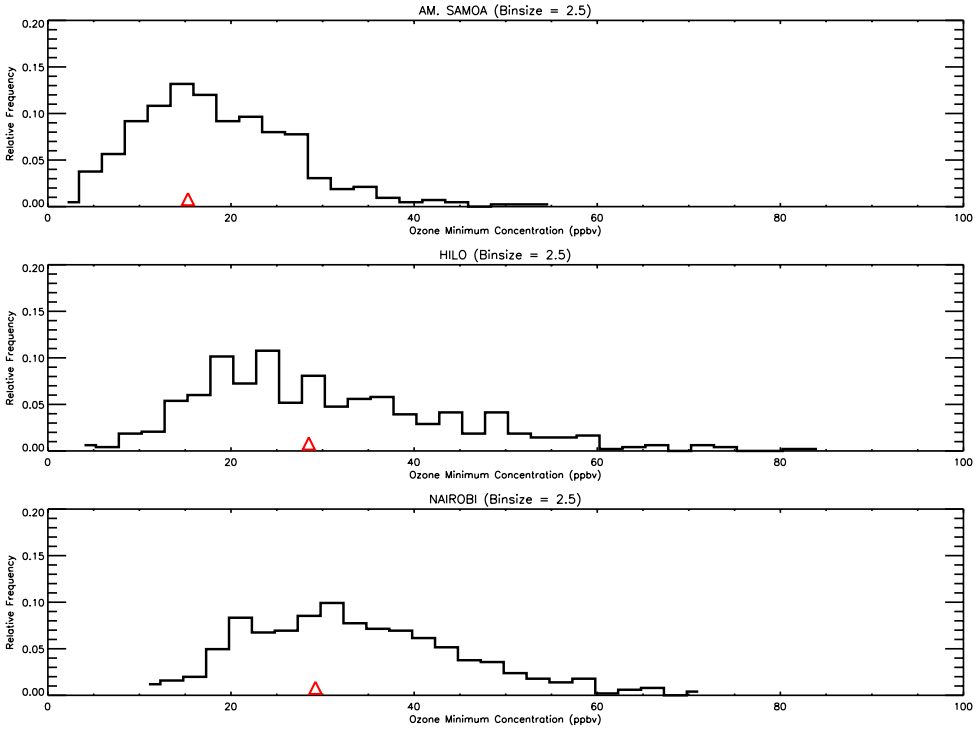

Figure 3.12: A frequency distributions of the ozone minimum concentration at American Samoa (Top), Hilo (Middle), and Nairobi (Bottom). Red triangles mark the average boundary layer ozone concentration for each station.

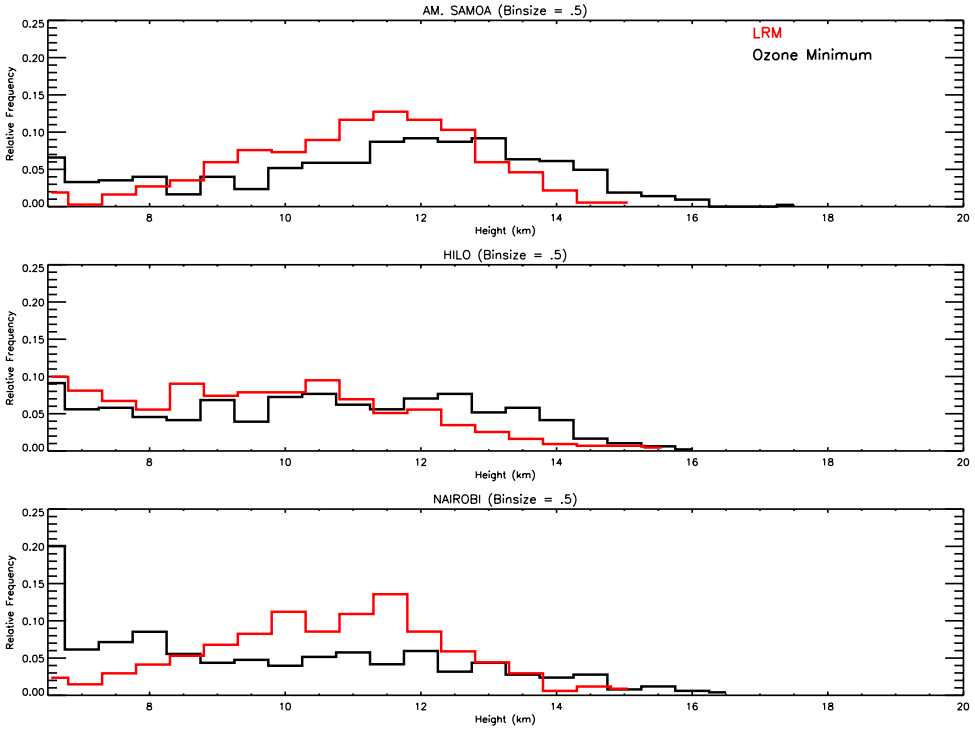

Figure 3.13: Frequency distributions of the ozone minimum height (black) and the LRM (red) at American Samoa (Top), Hilo (Middle), and Nairobi (Bottom).

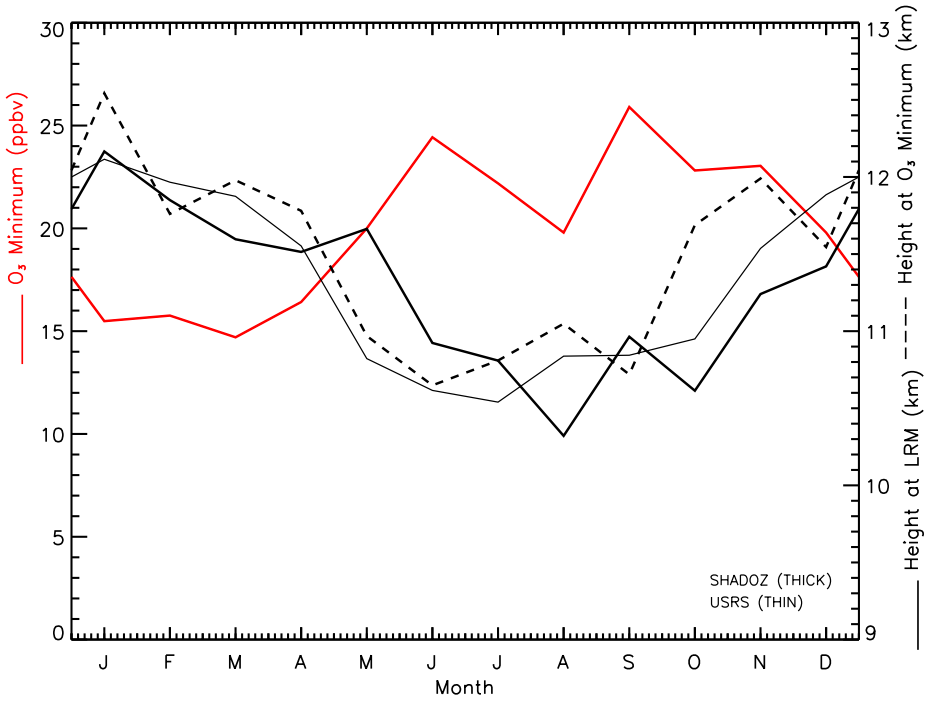

Figure 3.14: The annual cycle of the ozone minimum concentration (solid red), the ozone minimum height (dashed black), and the LRM height (solid black). The LRM height is computed using the SHADOZ data (thick) and US High Resolution Radiosonde Data (thin).

A)

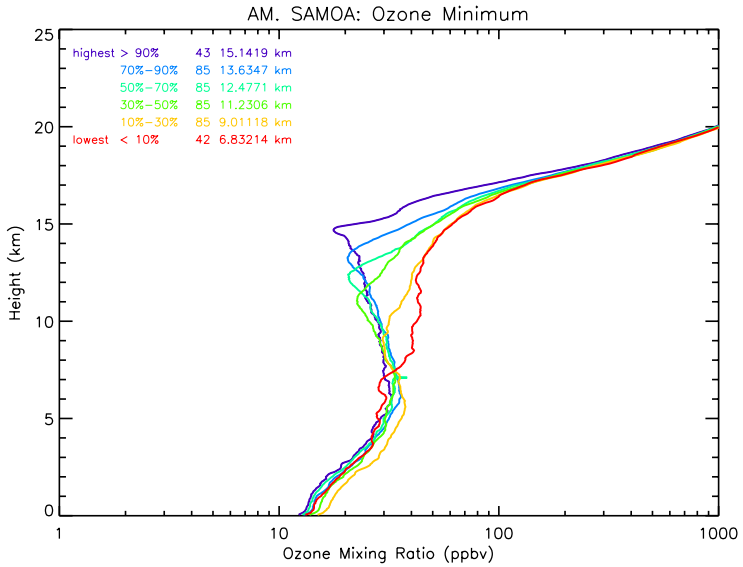
AM. SAMOA: Ozone Minimum
highest > 90% 43 15.1419 km
70%–90% 85 13.6347 km
50%–70% 85 12.4771 km
30%–50% 85 11.2306 km
10%–30% 85 9.01118 km
lowest < 10% 42 6.83214 km
Height (km)
Ozone Mixing Ratio (ppbv)

B)

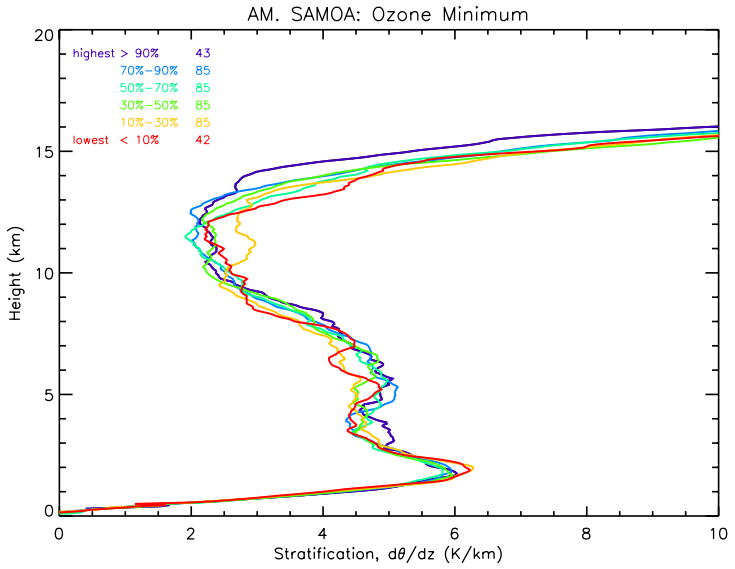
AM. SAMOA: Ozone Minimum
highest > 90% 43
70%–90% 85
50%–70% 85
30%–50% 85
10%–30% 85
lowest < 10% 42
Height (km)
Stratification, dθ/dz (K/km)

C)

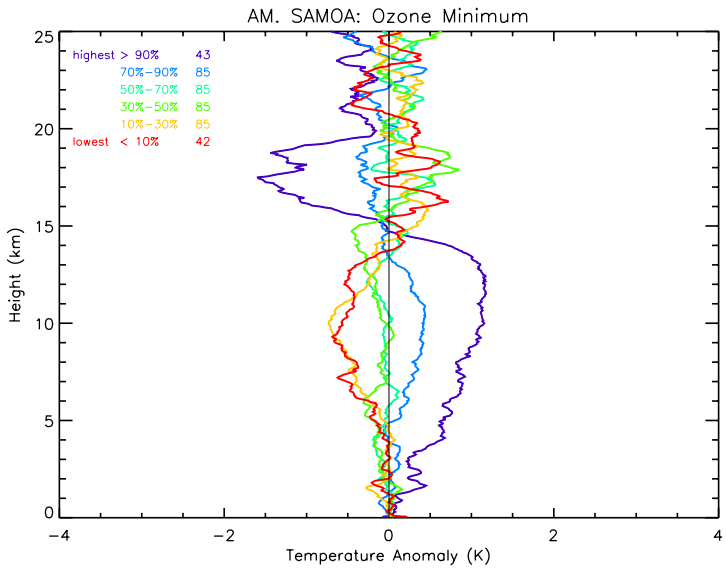

Figure 3.15: Average profiles of (A) ozone, (B) stratification, and (C) temperature anomaly composited by the height of the ozone minimum. The number of profiles that make up each composite group appears next to the percent. The average height of the ozone minimum for each composite group appears next to the number of profiles in (A).

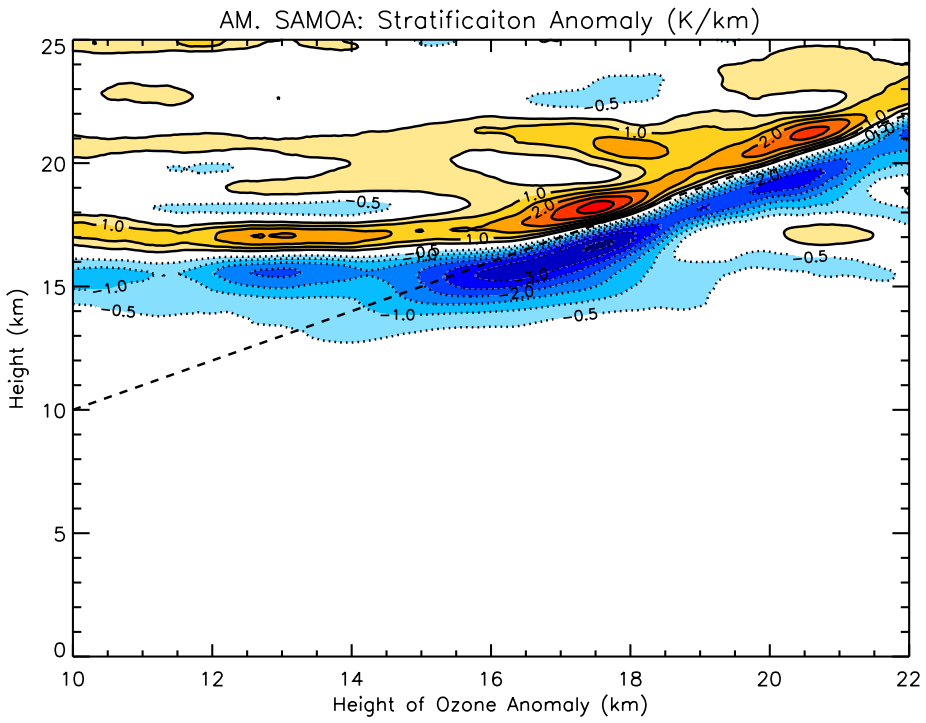

Figure 3.16: The average stratification anomaly for the negative anomaly composite contoured as a function of the height of at which the ozone anomaly is taken and height at American Samoa. The contour interval is 0.5 K/km, with dotted contours indicating negative anomalies. The 1:1 line appears as dashed.

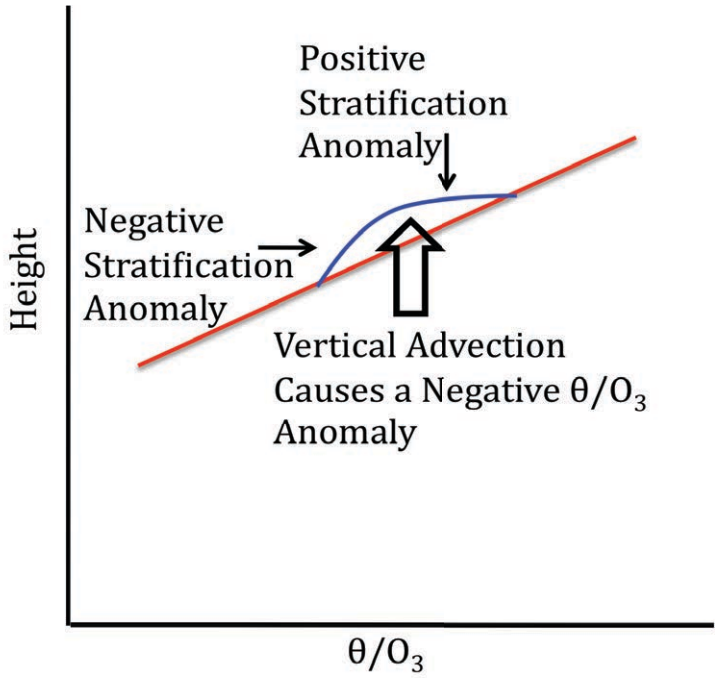

Figure 3.17: Mean (red) and perturbation (blue) ozone mixing ratio or potential temperature plotted as a function of height. In the stratosphere, ozone and potential temperature are quasi-passive tracers. Vertical advection acting on the background gradient of ozone can cause a negative ozone anomaly, which will also manifest in a negative potential temperature anomaly. Opposing stratification anomalies occur at the height of the ozone/potential temperature anomaly.

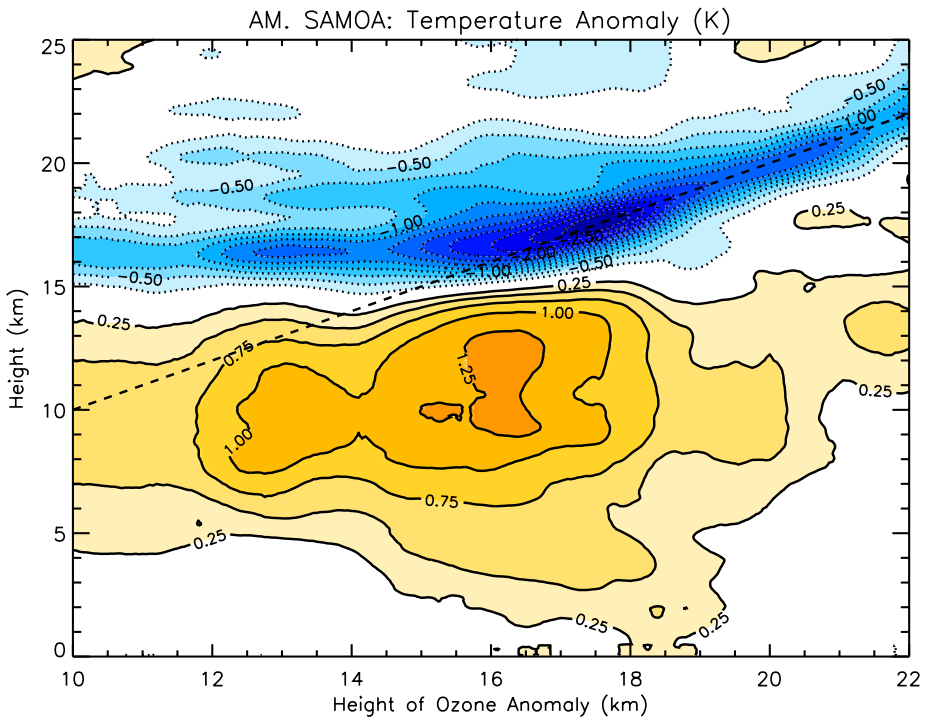

Figure 3.18: The average temperature anomaly for the negative anomaly composite contoured as a function of the height of at which the ozone anomaly is taken and height at American Samoa. The contour interval is 0.25 K, with dotted contours indicating negative anomalies. The 1:1 line appears as dashed.

A)

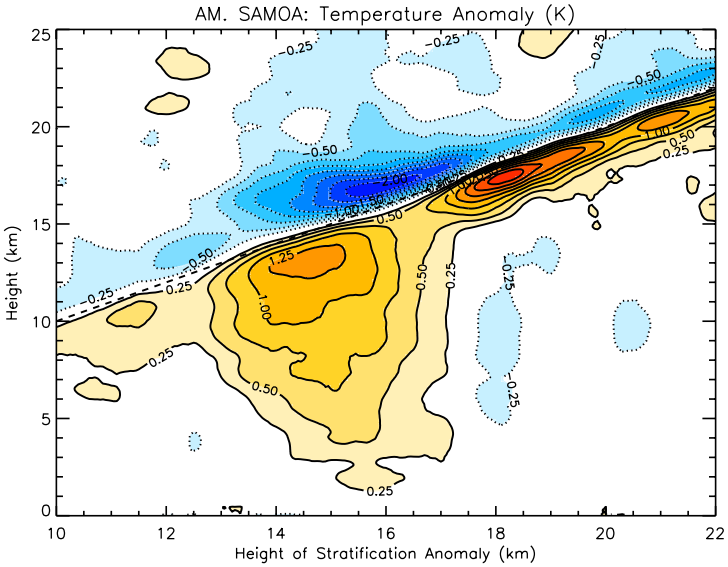

B)

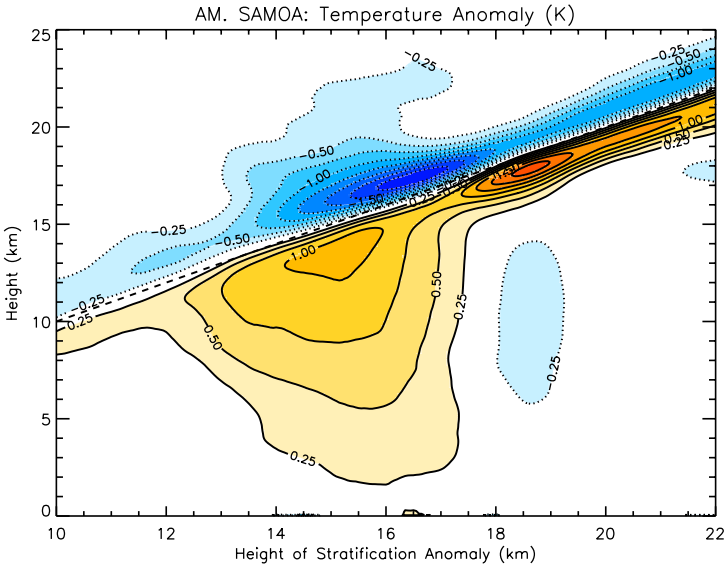

Figure 3.19: The average temperature anomaly for the negative anomaly composite contoured as a function of the height of at which the stratification anomaly is taken and height at American Samoa. Plots are computed using the SHADOZ dataset (A) and US High Resolution Radiosonde Data (B). The contour interval is 0.25 K, with dotted contours indicating negative anomalies. The 1:1 line appears as dashed.

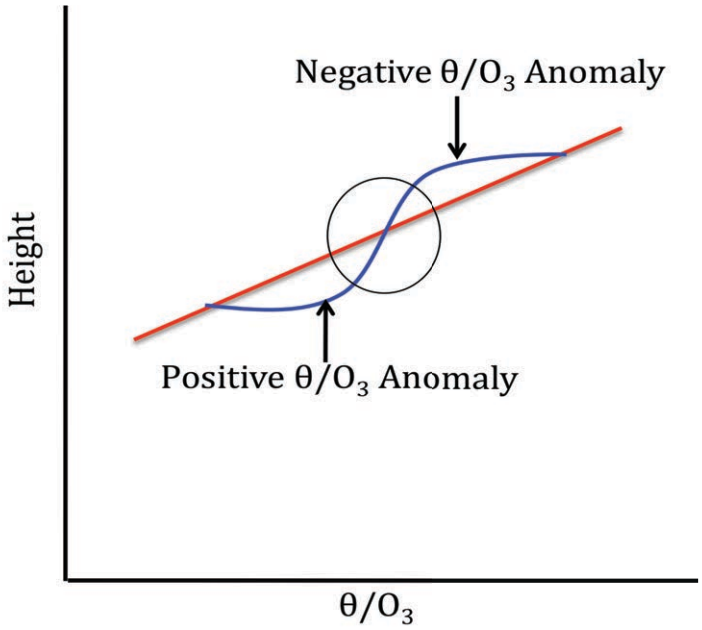

Figure 3.20: Mean (red) and perturbation (blue) ozone mixing ratio/potential temperature plotted as a function of height. Locally, a negative stratification anomaly (circled above) will be accompanied by warming below and cooling above.

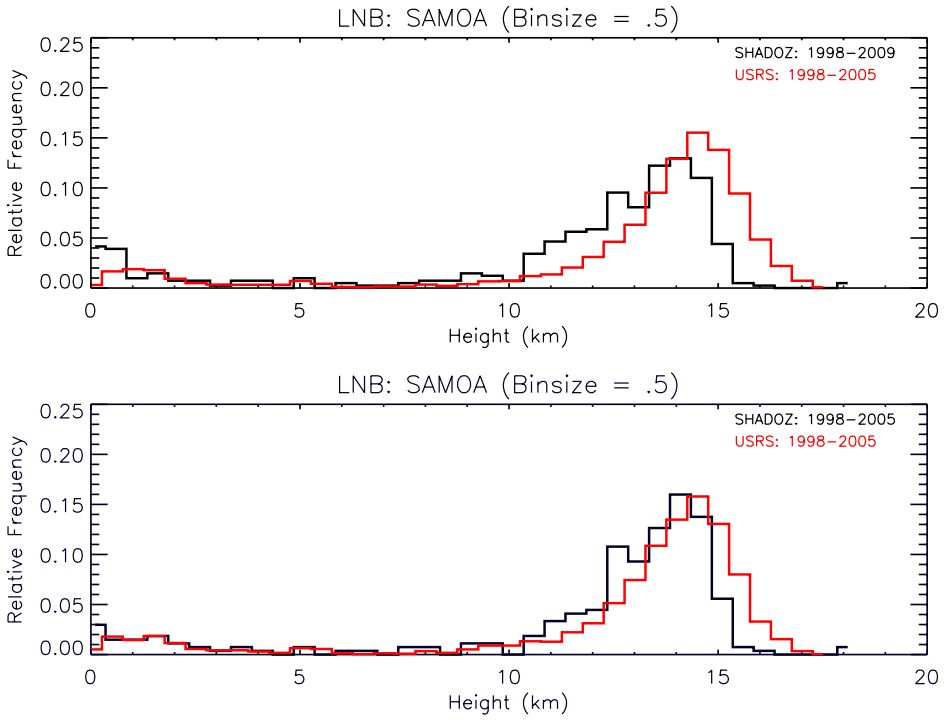

Figure 3.21: A frequency distribution of the LNB at American Samoa computed using the SHADOZ dataset (black) and US High Resolution Radiosonde Data (red) using all data (Top) and using comparable time periods and nighttime measurements (Bottom).

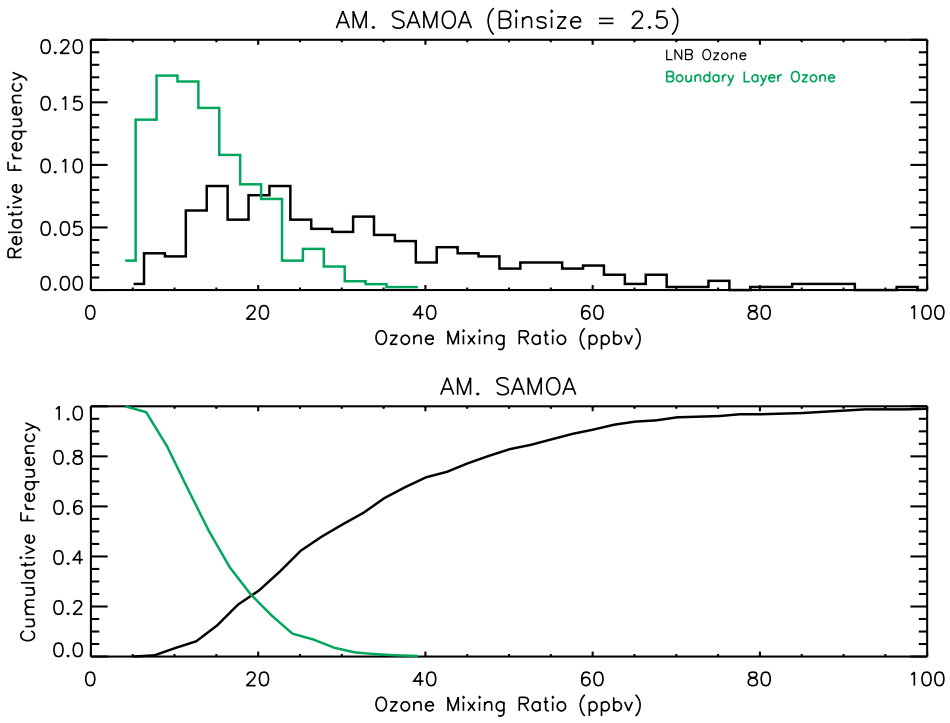

Figure 3.22: A frequency distribution (Top) of the ozone concentration at the LNB (black) and the boundary layer ozone concentration (green) at American Samoa. A cumulative distribution function (Bottom) of the ozone concentration at the LNB (black) and the boundary layer ozone concentration (green).

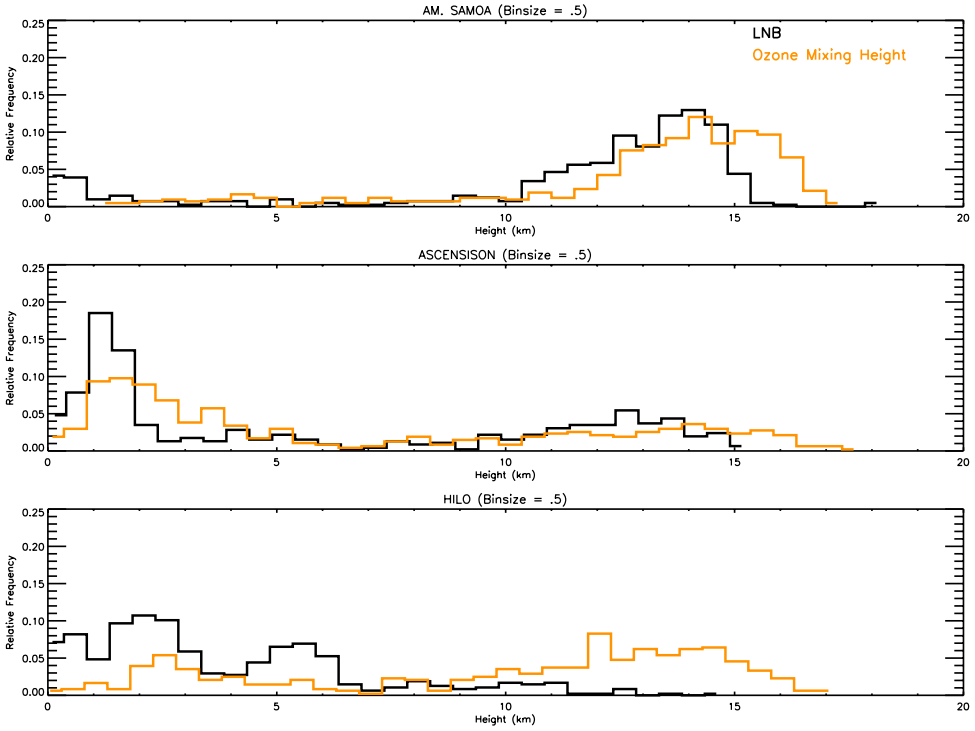

Figure 3.23: A frequency distribution of the LNB (black) and the ozone mixing height (orange) at American Samoa (Top), Ascension (Middle), and Hilo (Bottom).

A)

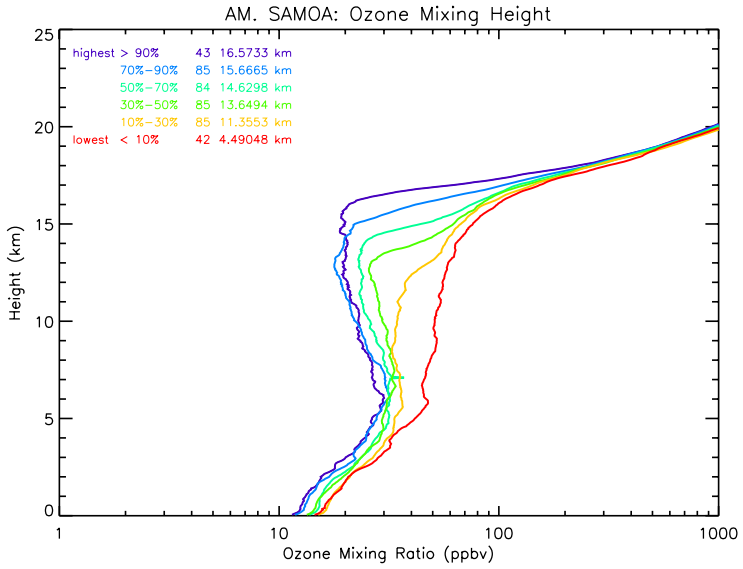
AM. SAMOA: Ozone Mixing Height
highest > 90% 43 16.5733 km
70%–90% 85 15.6665 km
50%–70% 84 14.6298 km
30%–50% 85 13.6494 km
10%–30% 85 11.3553 km
lowest < 10% 42 4.49048 km
Height (km)
Ozone Mixing Ratio (ppbv)

B)

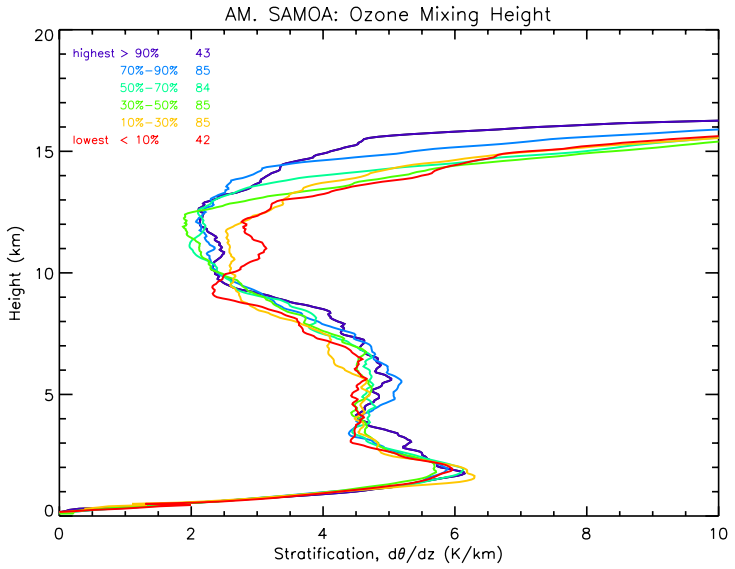
AM. SAMOA: Ozone Mixing Height
highest > 90% 43
70%–90% 85
50%–70% 84
30%–50% 85
10%–30% 85
lowest < 10% 42
Height (km)
Stratification, dθ/dz (K/km)

C)

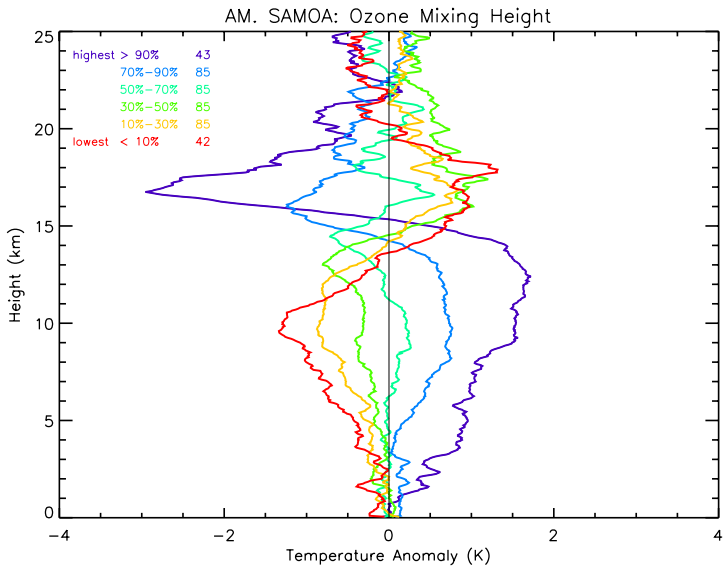

Figure 3.24: Average profiles of (A) ozone, (B) stratification, and (C) temperature anomaly composited by the height of the ozone mixing height at American Samoa. The number of profiles that make up each composite group appears next to the percent. The average height of the ozone minimum for each composite group appears next to the number of profiles in (A).

A)

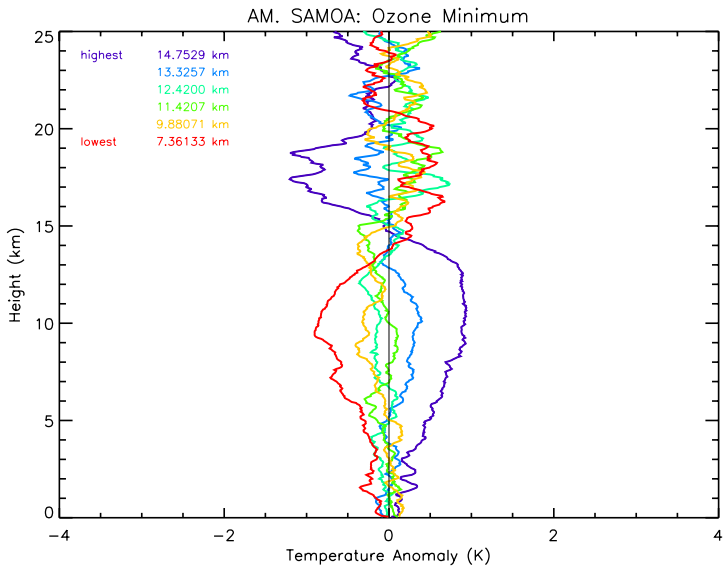

B)

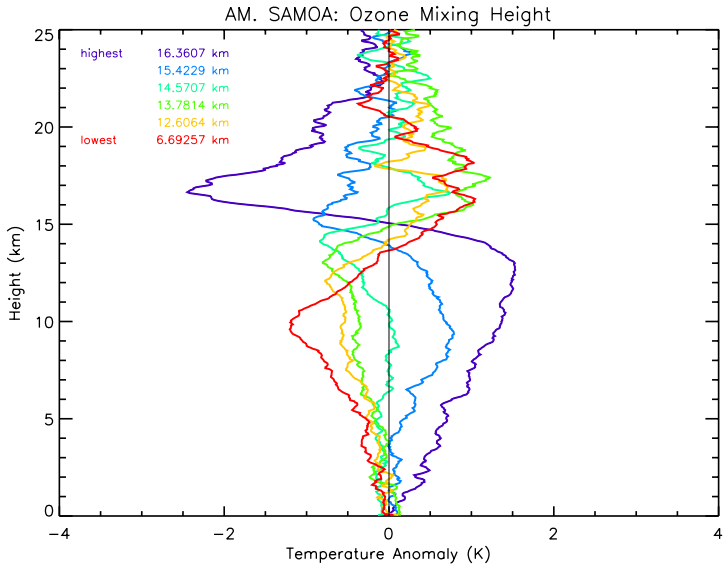

Figure 3.25: Average profiles of temperature anomaly composited by the height of the ozone minimum (A) and the ozone mixing height (B) at American Samoa. Each composite group contains the same number of profiles. The average height of the ozone minimum/ozone mixing height for each composite group appears in the plot.

4. ASSESSING CONVECTIVE INFLUENCE ON THE TROPICAL TROPOPAUSE LAYER (TTL) USING SATELLITE DATA

4.1 Deep Convective Cloud Occurrence from CloudSat Data

CloudSat 2B-CLDCLASS provides vertical cloud distribution sorted by cloud type. Here, we utilized the deep convective cloud type identified by this algorithm. This allows direct identification of a deep convective event, with the capacity to detect the maximum deep convective cloud height. In order to determine the maximum extent of deep convection, each 2B-CLDCLASS granule is sorted, identifying pixel columns that contain deep convective clouds. If a column is flagged as containing a deep convective cloud, the height, location, and time of the maximum deep convective cloud pixel height is recorded. Thus, we obtain spatial and temporal information concerning deep convective cloud tops.

Figure 4.1 displays the spatial distribution of deep convective cloud top pixels greater than 15 km (yellow), corresponding to the upper half of the TTL, and greater than 17 km (red), the approximate average height of the CPT, for DJF (Top), MAM, JJA, and SON (Bottom). The west Pacific, South America, and Africa most frequently observe deep convection of the highest threshold in all seasons. During DJF, the deepest convection takes place in northern Australia and the southwest Pacific, South America, and regions of Africa in the Southern Hemisphere. During JJA, frequency of deep convective cloud top pixels greater than 17 km over South

America is far reduced when compared to DJF. The deepest convection in JJA shifts to the Central Americas, the Asian monsoon region, and regions of Africa in the Northern Hemisphere. Deep convection greater than 15 km frequently occurs in the Indian and west Pacific Oceans in all seasons, while it is far less frequent in the Atlantic and east Pacific Oceans. Large areas of the Tropics, mainly over the oceans, do not experience deep convection greater than 15 km. This prompts another question: how often does deep convection greater than 15 km occur?

Figure 4.2 shows the (A) frequency distribution and the (B) cumulative distribution of deep convective cloud top pixel height. During DJF, only ~15% of deep convective cloud top pixels are greater than 15 km and only ~1% are greater than 17 km. The frequency distribution is bimodal, with a low altitude peak at 7 km and a high altitude peak at 14 km. While the deep convective clouds identified by the 2B-CLDCLASS algorithm do not include cumulus congestus, the low altitude peak is likely a remnant of their occurrence. The high altitude peak of the JJA distribution shifts toward lower altitudes and displays a lower relative frequency when compared to the high altitude peak in DJF. This indicates greater deep convective influence at higher altitudes during DJF. These figures show deep convection that overshoots 17 km is rare and only occurs in localized regions. Identified deep convective cloud top pixels will be useful for understanding the stratification and temperature of the TTL discussed in this chapter.

4.2 Lapse Rate Maximum (LRM) Statistics using COSMIC GPS Data

The LRM defines the lower bound of the TTL. This level indicates where the lapse rate departs from the moist adiabat and is no longer under the steady influence of convection (Gettleman and Forster 2002). Because the height of deep convection varies regionally, regional variability in LRM height is also expected. Here, we investigate the spatial distribution of the LRM height using the vertical derivative of COSMIC GPS temperature profiles (i.e. stratification). Stratification profiles are divided into a 2°x 2° grid, according to their location at 17 km, and averaged. The minimum of the average stratification profile defines the LRM height at each grid point. Defining the LRM in this way, rather than averaging LRM heights identified from individual profiles, better describes the average height of deep convective influence because it removes noise from individual events.

Figure 4.3 shows the spatial distribution of the annually averaged LRM height (Top). LRM heights are highest over the west Pacific, Africa, and South America, corresponding to regions with more frequent deep convective events greater than 17 km (refer to Figure 4.1). Figure 4.3 also shows the spatial distribution of LRM height during DJF (Middle) and JJA (Bottom). During DJF, the LRM height is highest over northern Australia, the southwest Pacific, South America, and regions of Africa in the Southern Hemisphere. During JJA, the highest LRM heights shift to the Central Americas, the Asian monsoon region, and Northern Hemisphere Africa. This is consistent with the seasonal shift in deep convection.

These findings show that the LRM height, defining the base of the TTL, is higher in regions that experience the deepest convection. This is consistent with

Gettelman and Forster (2002), which showed the annual cycle of LRM height to be strongly correlated with outgoing longwave radiation, and Gettelman and Birner (2007), which found a similar longitudinal structure in LRM height identified using one month of CHAMPS GPS data. Here, we have extended this analysis using COSMIC GPS data from April 2006-December 2010 to better define the spatial distribution of the LRM height in relation to deep convective cloud occurrence.

4.3 Investigating the Cold Point Tropopause (CPT) using COSMIC GPS Data

The CPT defines the upper bound of the TTL. The spatial distribution of CPT temperature is not zonally symmetric; rather the lowest temperatures occur in localized regions (refer to Section 1.2). This study investigates the temperature at 17 km, the approximate height of the CPT. Figure 4.4 (Top) shows the spatial distribution of the 20% (blue), 10% (green), 5% (yellow), and 1% (red) lowest temperatures at 17 km between 20°S-20°N. A clear longitudinal dependence is evident (Figure 4.4, Bottom). The 1% lowest temperatures at 17 km only occur in localized regions: the west Pacific, Africa, and South America. These regions also experience the highest frequency of deep convective events greater than 17 km (refer to Figure 4.1) and have high altitude LRM heights (refer to Figure 4.3).

While the actual temperature is lowest in regions with frequent occurrence of deep convection, determining the deviation from the mean is important for understanding convective influence. Deep convection warms the upper troposphere and cools the CPT with respect to the mean. Therefore, looking at the temperature anomaly at 17 km, rather than just the temperature, may give more information

about CPT variability associated with convection. In order to produce temperature anomaly profiles, COSMIC GPS temperature profiles are deseasonalized by removing the monthly mean temperature profile interpolated to the location of the sounding. The interpolation accounts for variations in COSMIC GPS temperature profile location at each vertical level. By way of the computed temperature anomaly profiles, the lowest anomalies at 17 km are investigated and compared to the lowest temperatures. Figure 4.5 displays the spatial distribution of the 20% (blue), 10% (green), 5% (yellow), and 1% (red) lowest temperature anomalies at 17 km between 10°S-10°N. The spatial distribution is not as localized as that of the lowest temperatures at 17 km, however the west Pacific and Africa still display numerous occurrences. It is important to note that the spatial distribution of temperature anomalies at 17 km between 20°S-20°N does not depend much on longitude, suggesting convection does not have a strong impact on temperature anomaly at 17 km moving away from the equator. However, overlap of regions with the lowest temperature anomalies (between 10°S-10°N), the lowest temperatures (refer to Figure 4.4), and high occurrence of deep convection greater than 17 km (refer to Figure 4.1) suggests deep convection has a significant impact on CPT temperature variability.

To better understand deep convective influence on temperature, distributions of temperature and temperature anomaly in convective and non-convective regions are compared. Figure 4.6 shows frequency distributions of the (A) temperature and (B) temperature anomaly at 17 km in the west Pacific (90°E-135°E) and east Pacific (135°W-90°W) between 10°S-10°N during DJF. The west

Pacific temperature distribution has a lower average temperature, a higher standard deviation, and a higher positive skew (the peak is shifted toward lower temperatures) compared to the east Pacific. The west Pacific temperature anomaly distribution also has a higher standard deviation compared to the east Pacific. These figures show that the west Pacific, a region with strong deep convective influence, experiences not only lower temperatures but also a greater spread of temperature anomalies. However, because many processes (including the annual cycle of the wave driven stratospheric circulation, ENSO, and deep convection) affect the temperature of this region, it is still necessary to identify the contribution of deep convection to CPT temperature variability.

4.4 COSMIC GPS and CloudSat Collocation

In order to understand deep convective influence on temperature, an investigation of the temperature anomaly at the time and location of a deep convective event is necessary. Data like this is hard to find without using model output. Here, deep convective cloud top pixels identified from CloudSat 2B-CLDCLASS are collocated with COMIC GPS temperature profiles. CloudSat and COSMIC missions, both launched in 2006, provide recent data with global coverage, and a few years over which to compute statistics.

4.4.1 Description of Method

First, the times of the identified deep convective cloud top pixels and the COSMIC GPS temperature profiles are transformed to a uniform measure with units

of number of hours since January 1, 2006 (0:00). Minutes are recorded as a fraction of an hour. The time it takes for a GPS temperature profile to pass through the atmosphere can be a few minutes, but this is ignored because we are unable to get close enough in time and space for minutes to be significant (to be discussed later). However, because the distance between the location of the profile at the top of the atmosphere and at the surface can be as much as 5 km, deep convective clouds are collocated to the location of the GPS profile at 17 km, the approximate height of the average CPT. The distance between deep convective clouds and temperature profiles is computed using the Great Circles Distance Formula: Distance = Radius*acos[sin(latitude1) * sin(latitude2) + cos(latitude1) * cos(latitude2) * cos(longitude2 - longitude1)]. In this formula, the radius is taken to be that of the earth (6378.7 km) and variations in radius are ignored because only the tropics are considered. The computed temperature anomaly profiles, described previously, are used to quantify the signal.

4.4.2 Results

Collocation of the deep convective clouds with temperature profiles allows for the direct observation of how deep convection affects the temperature of the TTL region. The large-scale temperature signal of deep convection, characterized by deep upper tropospheric warming and CPT cooling, is evident in temperature anomaly profiles in proximity to deep convective events. This temperature signal depends on the distance in time and space between the convective cloud top pixel

and the temperature profile, and it is strongly dependent on the height of the deep convective cloud top pixel.

The limiting factor to observing a deep convective temperature signal is the height of the deep convective cloud top pixel. Figure 4.7 shows the (A) DJF and (B) JJA average temperature anomaly profiles associated with various maximum deep convective cloud top pixel heights within 0-1000 km and +/- 6 hours. The DJF anomaly profile is computed for deep convective clouds between 20 °S-0 °, while the JJA anomaly profile is uses deep convective clouds between 0 °-20 °N. This latitude restriction takes into account the seasonal shift in deep convection (refer to Figure 4.1). An alternative plot depicting the same result appears in Figure 4.8. Here, the temperature anomaly is contoured as a function of the height of the maximum deep convective cloud top pixel and height. It is clear that the strongest convective temperature signal appears for temperature profiles in proximity to the highest deep convective clouds in both seasons. The temperature signal for deep convective clouds greater than 17 km in DJF is characterized by warming between 3-15 km, with the strongest warming (~1 K) occurring at ~12 km, and cooling between 15-18 km, with the strongest cooling (~-1.5 K) occurring at ~17 km. The anomaly profile associated with a maximum cloud top pixel between 16-17 km is similar, however the warming is between 3-14 km, with cooling between 14-17 km. The magnitude of the maximum cooling and heating is less than that for cloud top pixels greater than 17 km, and occurs at lower altitudes (maximum cooling is found at ~16 km). Cooling and warming shifts down and the magnitude is reduced further for the anomaly profiles in proximity to maximum cloud top pixels between 15-16 km. The

convective temperature signal disappears for deep convective clouds lower than 15 km. In chapter 4, results showed that the strongest convective temperature signal appears for ozone anomalies greater than 15 km (refer to Figure 3.18). This suggests that only the deep convective clouds that penetrate to the upper half of the TTL (> 15 km) have a significant impact on the temperature. As discussed previously, only ~15% of deep convective cloud top pixels are greater than 15 km, and ~1% are greater than 17 km (refer to Figure 4.2), and because deep convective clouds greater than 17 km only occur in localized region (refer to Figure 4.1), it seems that this temperature signal is only observed in these localized regions. The remainder of this section investigates the temperature anomaly in proximity to deep convective cloud top pixels greater than 17 km.

The signal also depends on the distance between the deep convective cloud top pixel and the COSMIC GPS temperature profile. Figure 4.9 shows the average temperature anomaly profile at varying distances between a deep convective cloud top pixel greater than 17 km and a COSMIC GPS temperature profile during (A) DJF and (B) JJA. During DJF, the strongest upper tropospheric warming/ CPT cooling is observed for temperature profiles within 0-250 km of a deep convective cloud top pixel. The strength of the warming/cooling decays with increasing distance. Despite the decay, a convective temperature signal is still apparent for temperature profiles within 2000-3000 km of a deep convective event. This indicates the signal is large-scale having an impact of TTL temperatures away from the deep convective event. DJF and JJA anomaly profiles within 0-250 km also show signs of cooling between the surface and 3 km. This is consistent with results in Folkins et al (2008), and

theory described by Houze (1989) where melting/evaporation in the subsidence region below a stratiform cloud base cools the environment. This signal decays to zero with increasing distance from the convective cloud top pixel, indicating this signal is smaller in scale when compared to the upper tropospheric warming/CPT cooling.

To better quantify deep convective influence on CPT temperature, Figure 4.10 shows the temperature anomaly at 17 km plotted as a function on the distance between the deep convective cloud top pixel and the COSMIC GPS temperature profile. Here, it is evident that the anomaly decays significantly faster with increasing distance in JJA, become insignificant beyond 2000 km. The anomaly in DJF is more persistent, having an impact up to 5000 km way from the convective event. Differences between seasons may be caused by the seasonal cycle of the stratospheric circulation acting to destabilize the TTL region during DJF and thereby promote deep convective influence on temperature. Large-scale tropical dynamics may also explain this signal, where tropical waves forced by deep convective heating produce a quasi-stationary temperature anomaly.

The time difference between convective cloud top pixels and COSMIC GPS temperature profiles also affects the temperature signal. Figure 4.11 shows the average anomaly profile within 0-1000 km and varying times of a deep convective event greater than 17 km during (A) DJF and (B) JJA. The closest anomaly profile in time (+/- 1 hr) to a deep convective event has the strongest cooling signal (~-1.5 K); however, the cooling is still in excess of ~-0.5 K at 17 km for profiles within +/- 96

hours (+/- 4 days) of the convective event. Here, it is evident that the convective temperature signal is persistent in time.

In order to recognize the time evolution of these events, Figure 4.12 shows the average temperature anomaly within 0-1000 km of a deep convective cloud top pixel greater than 17 km contoured as a function of time. During DJF, the convective temperature anomaly is strongest between -4 days to 8 days, while the temperature anomaly in JJA is significantly shorter lived. It is also appears that negative anomaly at the CPT precedes the strongest upper tropospheric warming, perhaps indicating destabilization of the upper troposphere prior to a convective event. Figure 4.12 effectively reveals the long time scale of the convective temperature signal.

To better understand the distribution of temperature anomalies, Figure 4.13 displays frequency distributions of temperature anomaly at (A) 17 km and (B) 10 km for profiles within 0-1000 km and +/- 6 hrs of a deep convective cloud top pixel greater than 17 km. The standard deviation of the temperature anomaly at 17 km is much higher than at 10 km indicating a larger range of temperature anomalies at 17 km. The anomaly at 17 km is on average -1.24 K, with ~70% of the observed anomalies being less than zero, while the anomaly at 10 km is on average 0.83 K, with ~75% of the observed anomalies being greater than zero. Here, it is evident that the majority of the anomalies have the expected mathematical sign.

4.5 Concluding Remarks

This chapter showed that deep convective cloud top pixels greater than 17 km correspond to regions with high LRM heights and low CPT temperatures.

Analysis of the convective temperature signal through collocation of deep convective cloud top pixels identified by CloudSat 2B-CLDCLASS and COSMIC GPS temperature profiles revealed that the signal is large-scale and persistent in time. However, the strongest signal appears for temperature profiles close in time and space to deep convective events that penetrate to the upper half of the TTL (>15 km). Figure 4.14 shows the average temperature anomaly for temperature profiles within 0-250 km and +/- 1 hour of a deep convective event greater than 17 km for DJF and JJA. While only 13 profiles make up the DJF anomaly profile, a very strong convective signal is evident with an anomaly of ~-3 K occurring at 17 km. This composite represents the closest in time and space this collocation method can get, and reveals the strongest signal. Here, we have directly identified the impact of deep convection on TTL temperature utilizing satellite data. This data provides a unique perspective of the region with large spatial coverage allowing for better quantification of the deep convective signal.

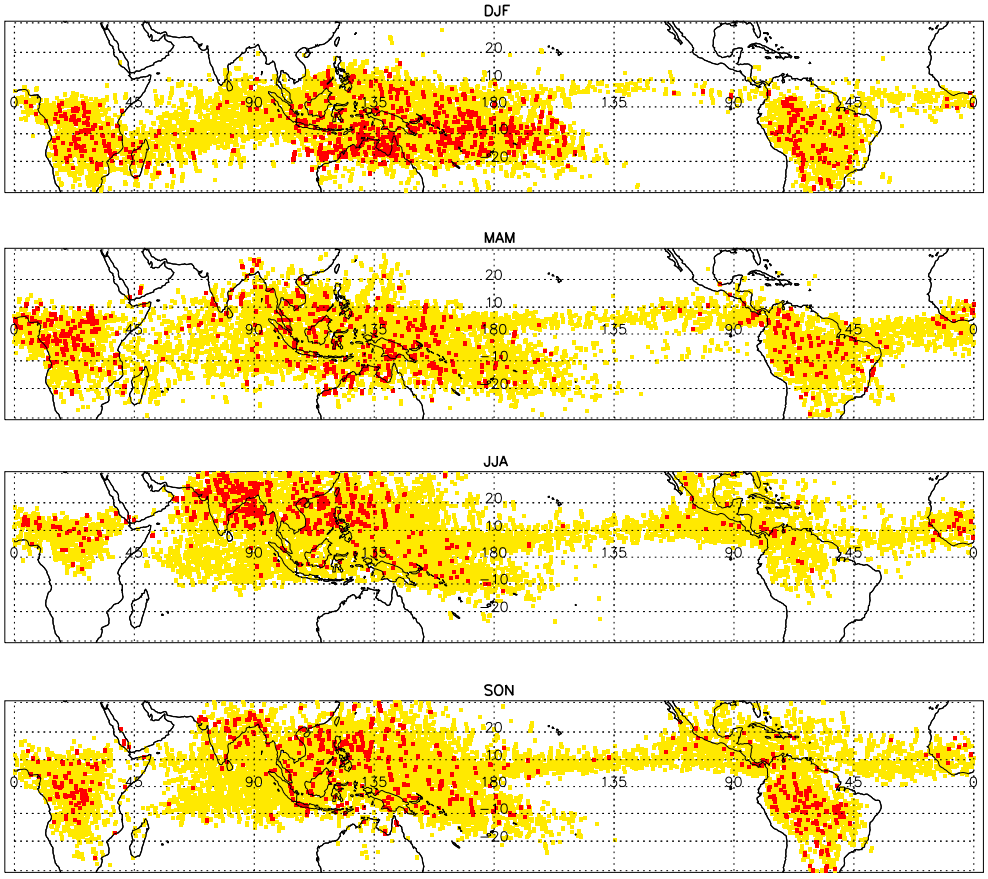

Figure 4.1: Spatial distribution of deep convective cloud top pixels greater than 15 km (yellow) and greater than 17 km (red) during DJF (top), MAM, JJA, and SON (bottom).

A)

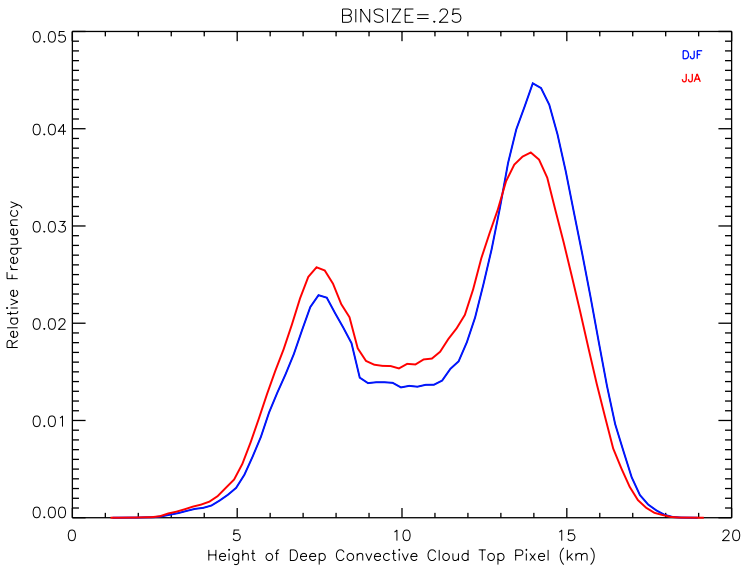

B)

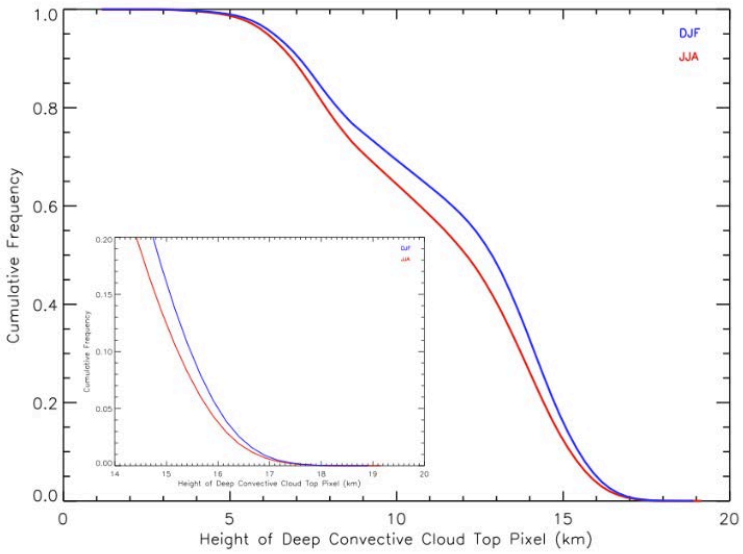

Figure 4.2: (A) Frequency distribution and (B) cumulative distribution of the height of the deep convective cloud top pixels identified from CloudSat 2B-CLDCLASS during DJF (blue) and JJA (red). The latitudes are restricted for each season: DJF represents clouds between 20°S-0° and JJA represents clouds between 0°-20°N.

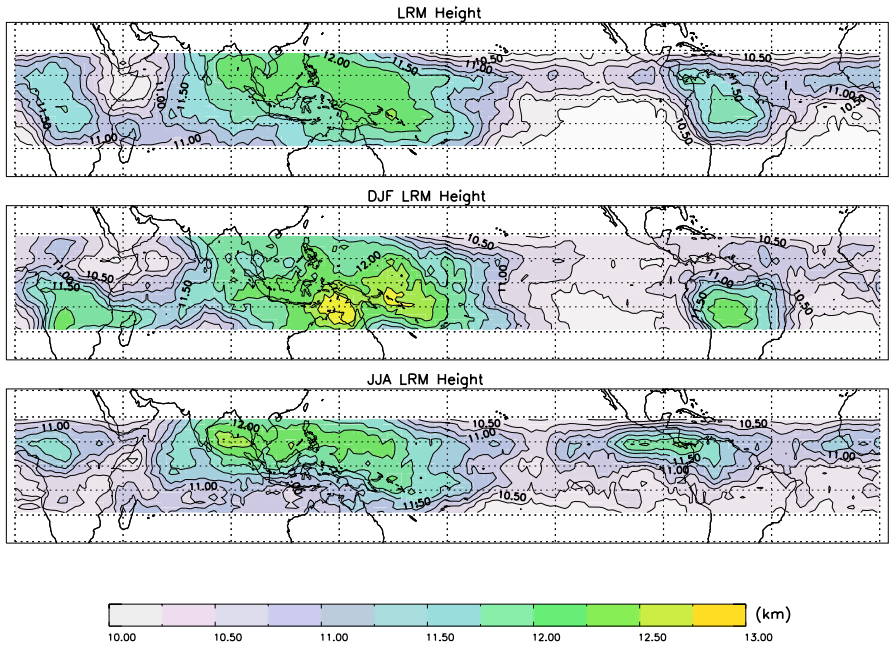

Figure 4.3: Spatial distribution of the annual (Top), DJF (Middle), and JJA (Bottom) LRM height computed using COSMIC GPS data.

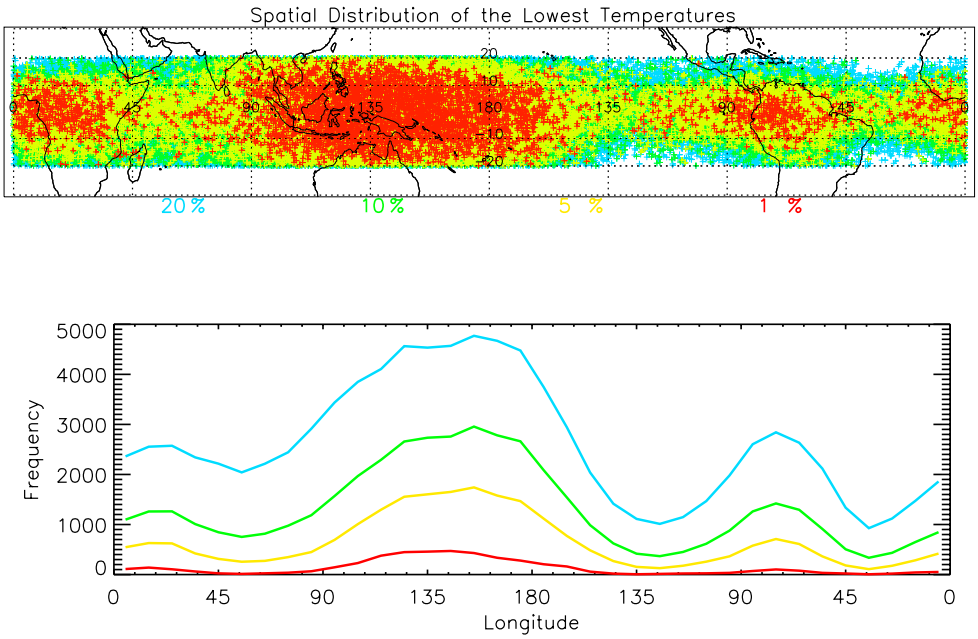

Figure 4.4: The spatial distribution of the 20% (blue), 10% (green), 5% (yellow), and 1% (red) lowest temperatures at 17 km found using COSMIC GPS data (Top).

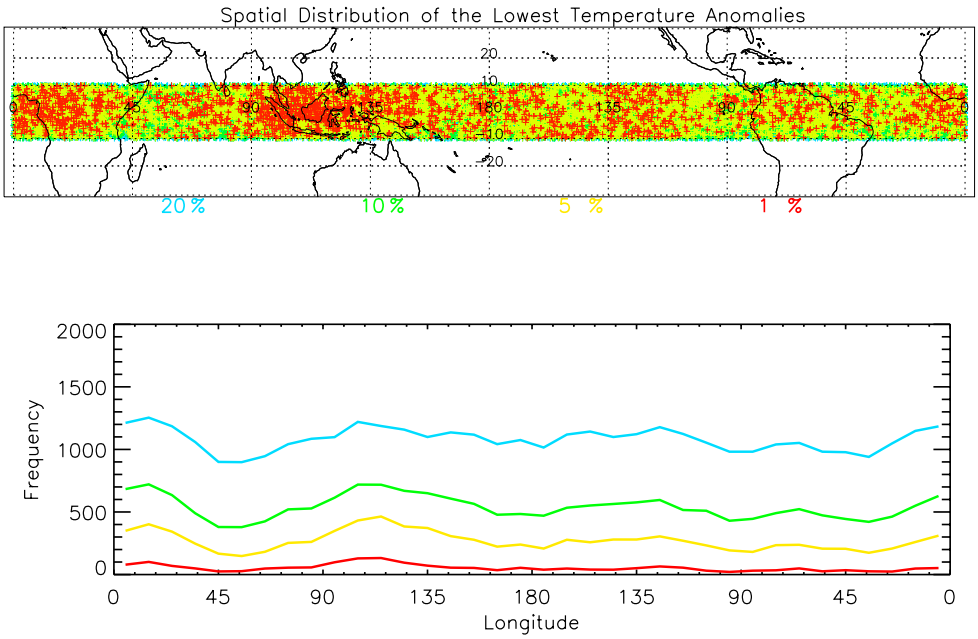

Figure 4.5: The spatial distribution of the 20% (blue), 10% (green), 5% (yellow), and 1% (red) lowest temperature anomalies at 17 km found using COSMIC GPS data (Top).

A)

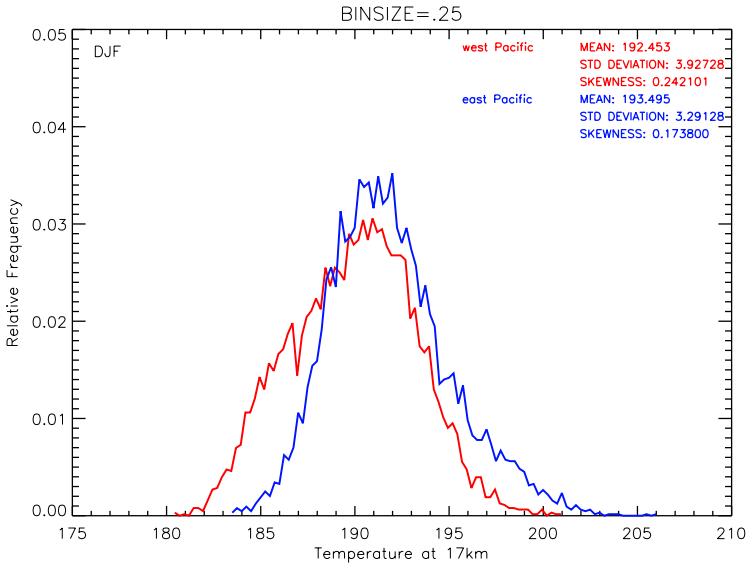

B)

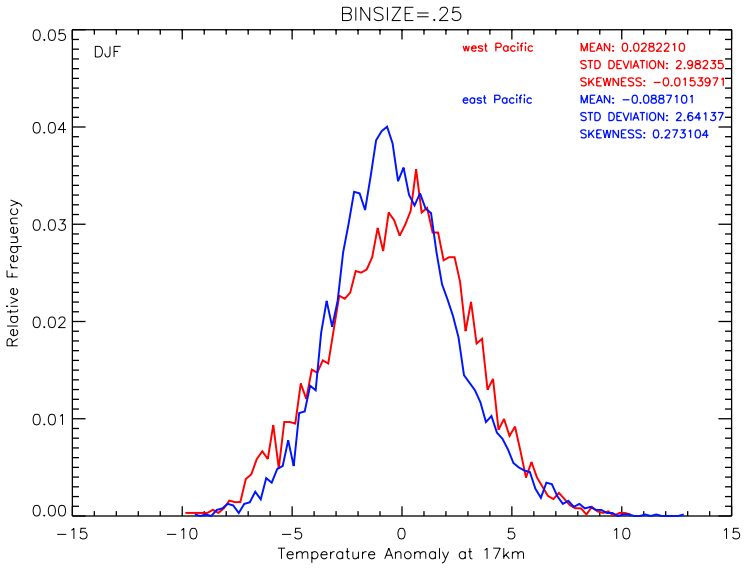

Figure 4.6: Frequency distributions of the (A) temperature at 17 km and the (B) temperature anomaly at 17 km. The red represents the west Pacific (90 °E-135 °E), and the blue represents the east Pacific (135 °W-90 °W) taken between 10 °S-10 °N during DJF.

A)

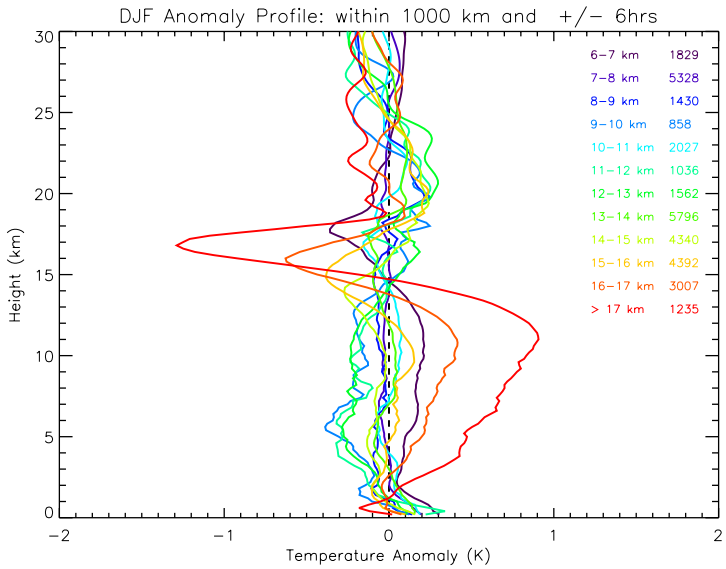

B)

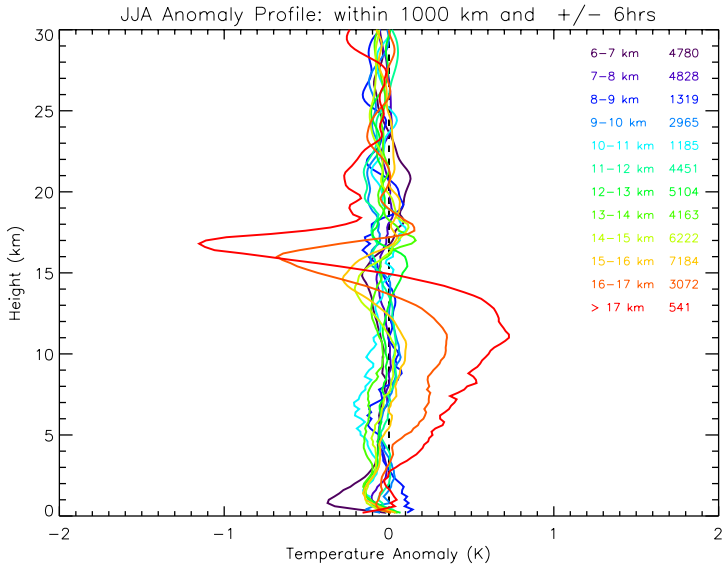

Figure 4.7: Average temperature anomaly profiles for GPS soundings within +/- 6 hrs and 1000 km of a maximum deep convective cloud greater than 17 km (red), between 16-17 km (orange), between 15-16 km (yellow), and etc. during (A) DJF and (B) JJA. The latitudes are restricted for each season: DJF represents clouds between 20°S-0° and JJA represents clouds between 0°-20°N. The number of profiles that go into each anomaly profile is shown on the right side of the figure.

A)

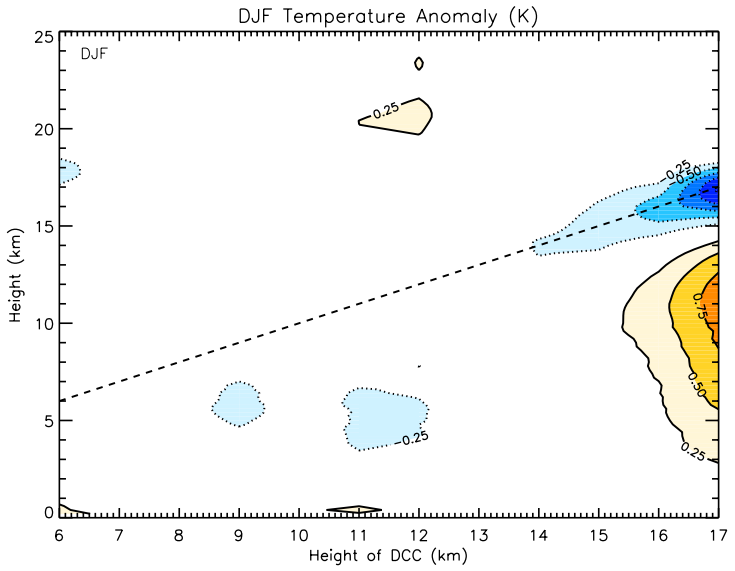

B)

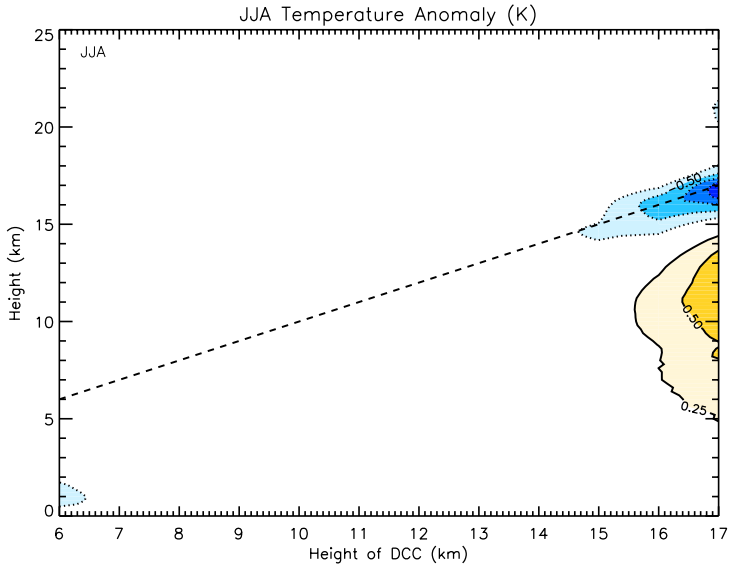

Figure 4.8: Average temperature anomaly within +/- 6 hrs and 1000 km of deep convection contoured as a function of the maximum deep convective cloud top pixel height within range and height during (A) DJF and (B) JJA. The latitudes are restricted for each season: DJF represents clouds between 20 °S-0 ° and JJA represents clouds between 0 °-20 °N. The contour interval is 0.25 K. The 1:1 line appears as dashed.

A)

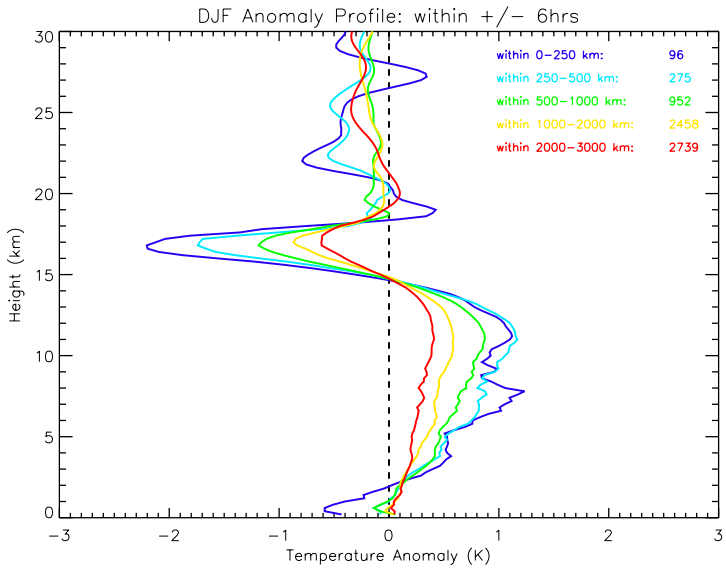

B)

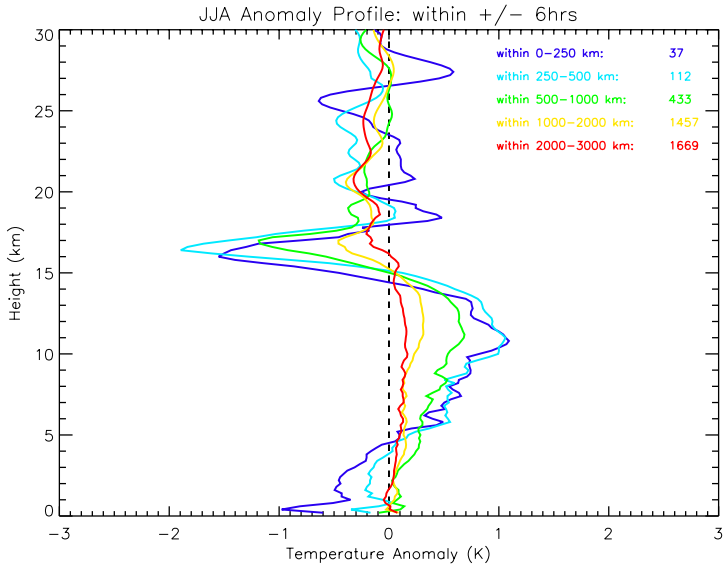

Figure 4.9: Average temperature anomaly profiles for GPS soundings within +/- 6 hrs and 0-250 km (purple), 250-500 km (blue), 500-1000 km (green), 1000-2000 km (yellow), and 3000 km (red) of a deep convective cloud greater than 17 km during (A) DJF and (B) JJA. The latitudes are restricted for each season: DJF represents clouds between 20°S-0° and JJA represents clouds between 0°-20°N. The number of profiles that go into each anomaly profile appears on the right side.

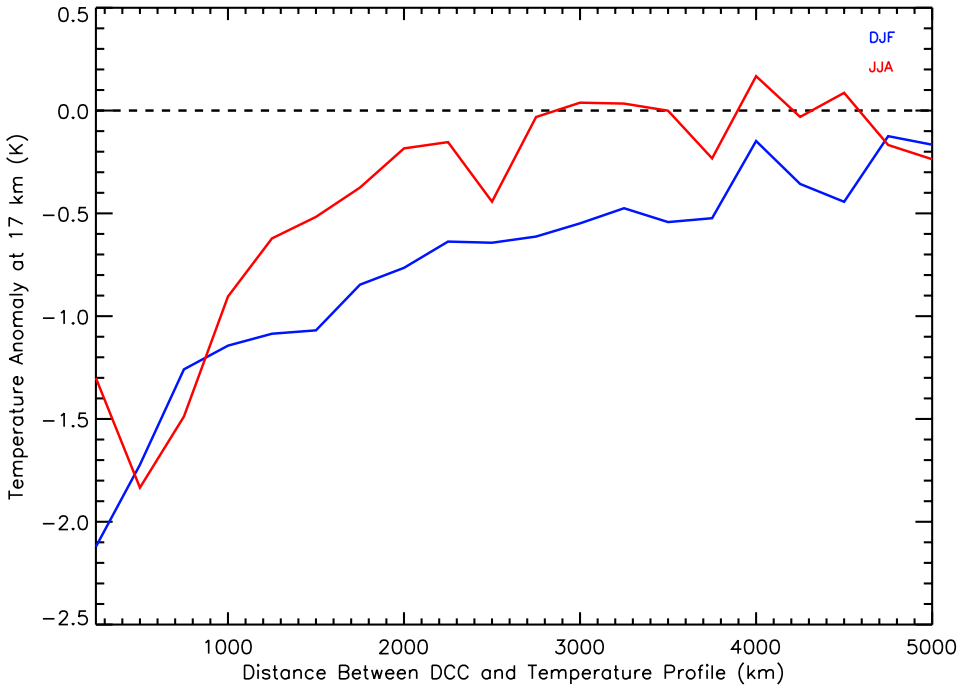

Figure 4.10: The temperature anomaly at 17 km plotted as a function of distance between the convective cloud top pixel and the COSMIC GPS temperature profile for DJF (blue) and JJA (red). The latitudes are restricted for each season: DJF represents clouds between 20°S-0° and JJA represents clouds between 0°-20°N.

A)

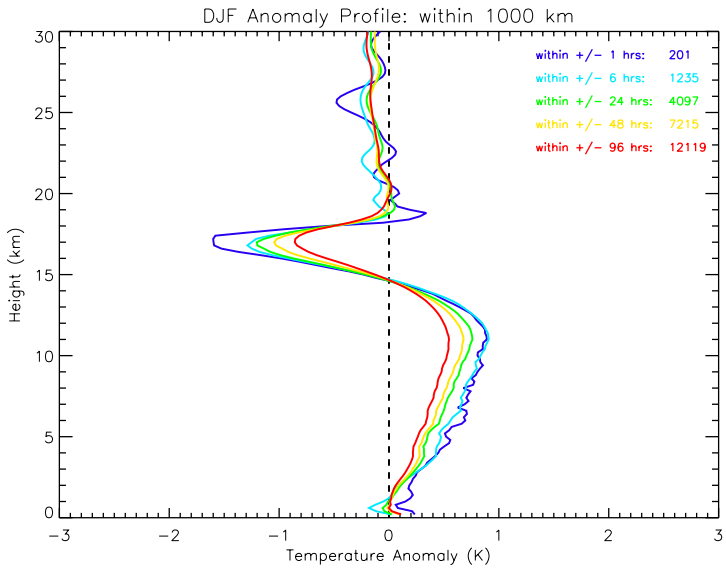

B)

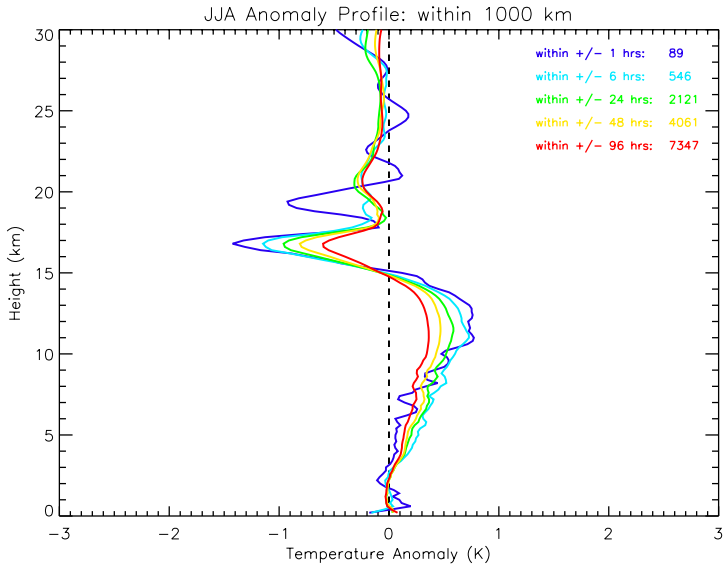

Figure 4.11: Average temperature anomaly profiles for GPS soundings within 1000 km and +/- 1 hrs (purple), +/- 6 hrs (blue), +/- 24 hrs (green), +/- 48 hrs (yellow), and +/- 96 hrs (red) of a deep convective cloud greater than 17 km during (A) DJF and (B) JJA. The latitudes are restricted for each season: DJF represents clouds between 20°S-0° and JJA represents clouds between 0°-20°N. The number of profiles that go into each anomaly profile is shown on the right side of the figure.

A)

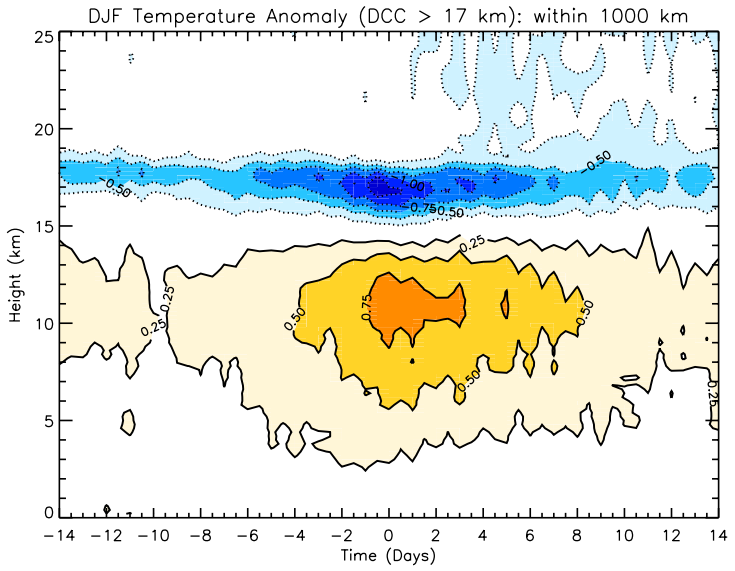

B)

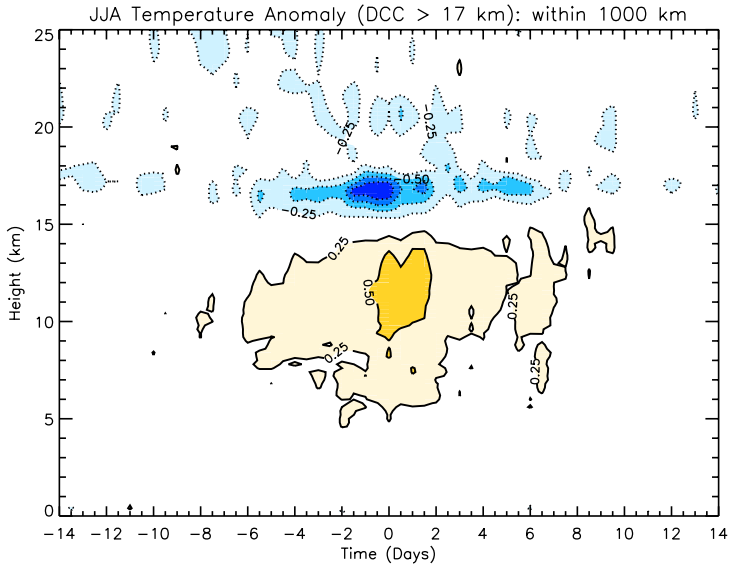

Figure 4.12: The temperature anomaly within 0-1000km of a deep convective cloud top pixel greater than 17 km contoured as a function of time and height during (A) DJF and (B) JJA. The latitudes are restricted for each season: DJF represents clouds between 20°S-0° and JJA represents clouds between 0°-20°N. The contour interval is 0.25 K.

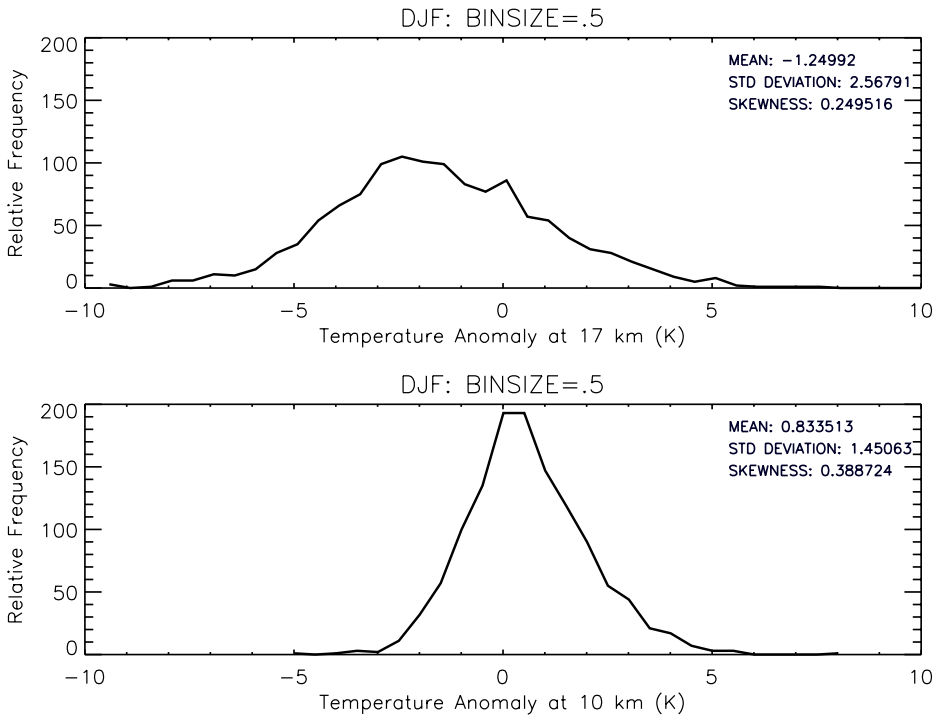

Figure 4.13: The frequency distribution of temperature anomalies at (A) 17 km and (B) 10 km for profiles within 0-1000 km and +/- 6 hrs of a deep convective cloud top pixel greater than 17 km during DJF. DJF represents clouds between 20°S-0°.

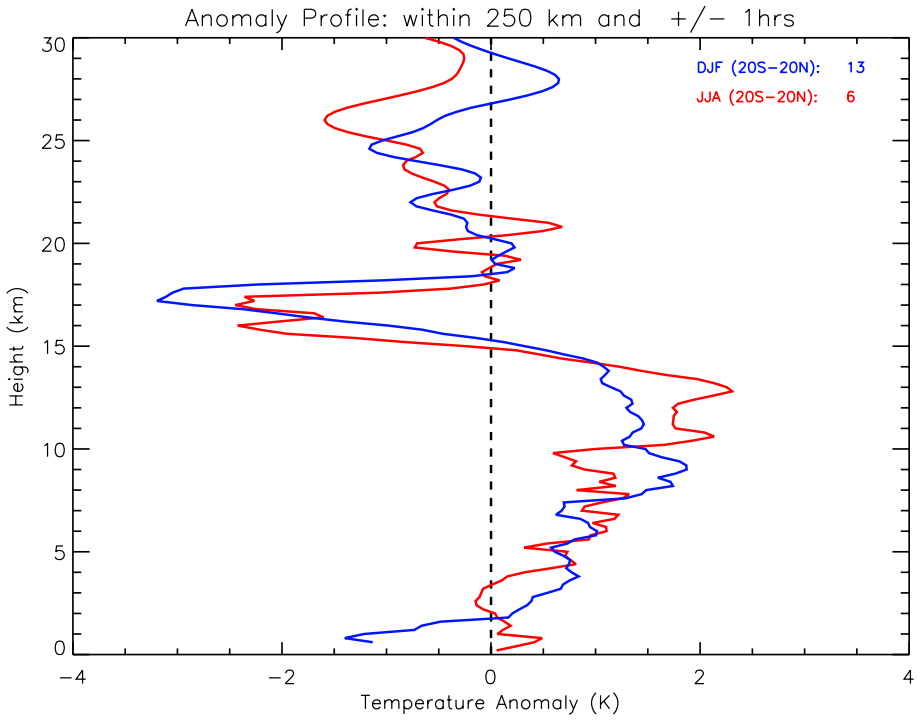

Figure 4.14: Average temperature anomaly profiles for GPS soundings within 250 km and +/- 1 hrs of a deep convective cloud greater than 17 km during DJF (blue) and JJA (red). The latitudes are restricted for each season: DJF represents clouds between 20°S-0° and JJA represents clouds between 0°-20°N. The number of profiles that go into each anomaly profile is shown on the right side of the figure.

5. CONCLUSIONS

This study has used two approaches in order to understand deep convective influence on the TTL. The first approach utilized the SHADOZ dataset, investigating ozone as a tracer for deep convection. Three methods were presented to quantify convective influence on ozone profiles: the ozone minimum, ozone/stratification anomalies, and the ozone mixing height. The ozone minimum method provided a starting point for understanding convective influence, but proved to be insufficient because ozone can remain low over a layer in the upper troposphere. Thus, the height of the ozone minimum, which is a point measurement, may be irrelevant in many situations. Ozone/stratification anomalies between 12-18 km revealed a convective signal in temperature, with a stronger signal occurring above 15 km, corresponding to the upper half of the TTL. Because the average LRM height is lower than 15 km, a new method was introduced, the ozone mixing height, motivated by the LNB. This method better separated profiles with strong deep convective influence.

The second approach for understanding deep convective influence on the TTL utilized CloudSat 2B-CLDCLASS data. Identified deep convective cloud top pixels were collocated with COMSIC GPS temperature profiles. The strongest convective temperature signal appeared when looking at deep convective cloud top pixels that penetrate to the upper half of the TTL (> 15 km). The signal also

appeared stronger when the distance in space and time was minimized. Results indicate that the convective temperature signal is large-scale and persistent is time. Separately, SHADOZ and CloudSat/COSMIC GPS revealed convective temperature signals; however, using them in combination can provide deeper understanding of the convective influence on the TTL.

Figure 5.1 shows the spatial distribution of deep convective cloud top pixels greater than 15 km (yellow), corresponding to the upper half of the TTL, and greater than 17 km (red), the approximate height of the CPT, during DJF. This is very similar to Figure 4.1, but it also highlights the SHADOZ stations. During DJF, American Samoa, Fiji, Java, and Kuala Lumpur are located in regions with strong deep convective influence, while Nairobi, Natal, San Cristobal, and Paramaribo lie on the periphery of regions with strong deep convection. Hilo and Ascension are not in close proximity to convection during DJF. Deep convective influence at Hilo is strongest during JJA; however, convective cloud top pixels are rarely greater than 15 km in any season. Knowledge of the exact proximity of each station to deep convection can be used to better explain their average ozone profiles.

Even though American Samoa, Fiji, Java, and Kuala Lumpur are all located in deep convective regions, their average ozone profiles are different; American Samoa and Fiji have an "S" shaped profile, while Java has a higher boundary layer ozone concentration and Kuala Lumpur does not have a strong upper tropospheric minimum (refer to Figure 3.5). Because their convective environments appear similar, the differences in shape likely arise from chemistry. Java and Kuala Lumpur are located in populated regions with greater pollution that leads to higher surface

ozone concentrations (Thompson et al. 2011). Therefore, it can be concluded that low ozone anomalies in the upper troposphere at these stations do not reflect transport from the surface; rather, the easterly prevailing wind at 200 hPa advects low upper tropospheric ozone concentrations from pristine convective regions like Samoa and Fiji.

To better understand convection at each station, deep convective cloud top pixels identified within 1000 km of a station are used to create cloud climatologies. The deep convective cloud climatology for the American Samoa station appears in Figure 5.2 (A), where relative frequency of identified deep convective cloud top pixels is contoured as a function of month and height. Here it is evident that deep convection most frequently occurs in December, January, February, March, and April. These months also display a bimodal distribution in deep convective cloud top pixel height. Deep convective cloud tops most frequently occur at 15 km; however, a second maximum is evident between 7-8 km indicating the presences of cumulus congestus. Plotted over the deep convective cloud climatology is the annual cycle of the LNB and the ozone mixing height. The LNB and the ozone mixing height tend to occur at the same altitude as the deep convective cloud tops, and are much more representative of convective cloud top pixel height when compared to the annual cycle of the LRM and the ozone minimum height.

Figure 5.2 (B) shows the annual cycle of ozone mixing ratio contoured as a function of height at American Samoa. This plot is similar in construction to plots in Thompson et al. (2011). Here, it is clear that upper tropospheric ozone concentrations are lower in months with a high frequency of deep convection, and

the strong transition between the tropospheric and stratospheric chemical regime occurs at ~15 km.

To better visualize the relationship between measures of deep convection, Figure 5.3 (A) shows the frequency distribution of convective cloud top pixel height, the LNB, and the LRM height. The peak of the LNB distribution aligns with the high altitude peak of the convective cloud top pixel distribution, while the LRM distribution peaks at a lower altitude. Thus, it is clear that the LNB better represents the deep convective cloud tops. Very few LNBs and deep convective cloud top pixels occur above 15 km, suggesting this is point where most convection subsides. Figure 5.3 (B) presents a frequency distribution of convective cloud top pixel height, the ozone mixing height, and the ozone minimum height. The high altitude peak of the deep convective cloud top pixel distribution falls between the peaks of the ozone minimum height distribution, which is shifted toward lower altitudes, and the ozone mixing height distribution, which is shifted toward higher altitudes. The ozone mixing height tends to overestimate the convective cloud top heights; however, it was able to better separate profiles with strong convective influence than the ozone minimum method (refer to Figure 3.25).

As a comparison, Figure 5.4 and 5.5 shows similar panels to Figure 5.2 and 5.3 but at Natal. Figure 5.4 (A) shows the annual cycle of deep convective cloud top pixel height. Natal differs from American Samoa in that it has a strong wet and dry seasons. The wet season December-June has a high frequency of convective cloud top pixels occurring at 14 km and 7 km. The annual cycles of the ozone mixing height and LNB tend to follow the convective cloud tops, occurring at higher

altitudes during the wet season. The annual cycles of the LRM and ozone minimum height are below the convective cloud tops. Figure 5.4 (B) shows the annual cycle of ozone mixing ratio contoured as a function of height at Natal. Upper tropospheric ozone is low during the wet season, indicating convective transport from the surface. The dry season has very high ozone concentrations in middle and upper troposphere. Thompson et al. (2011) described this as a feature of the descent via the Walker Circulation, however it seems likely the strong shift in upper tropospheric ozone is due to the reduction of deep convective transport in this season. Thus, the lack of deep convection decreases vertical mixing of low surface ozone concentrations leading to increased ozone concentrations in the upper troposphere. It is important to note that the dry season will also have larger amounts of biomass burning pollution, which causes chemical ozone production, acting as sort of a positive feedback on ozone in this season. Nevertheless, the dry season at Natal provides insight into ozone in the "absence" of dynamics. Figure 5.5 (A) shows the peak of the LNB distribution and the high altitude peak of the deep convective cloud top pixel distribution occur at the same altitude, while the LRM is not representative of convective cloud top height. The peak of the ozone mixing height in Figure 5.5 (B) also much better characterizes convective cloud top when compared to the ozone minimum.

Combining SHADOZ and CloudSat has shown that the height of deep convective cloud tops is well represented by the LNB. Despite the discrepancy between the ozone mixing height and deep convective cloud top pixel height, it is concluded that using ozone at the LNB is a useful way to define the ozone mixing

height threshold; however, future work is still necessary. Because the maximum LNB and convective cloud tops subside at ~15 km, deep convection is concluded to be significant in influencing composition up to this level during convective seasons. Although the calculation of the LNB assumes undilute convection, strong agreement between the convective cloud top pixel height and the LNB suggest that it effectively defines the maximum extent of deep convective influence. While the LRM shows regional variability, occurring at higher altitudes in convective regions, its altitude does not reflect the level where deep convection has a significant impact on the TTL. Because the convective temperature/stratification signals appeared for ozone anomalies between 12-18 km, with 12 km being the peak of the LRM distribution, we conclude that maximum detrainment of convection is between the LRM and LNB, but it is the highest deep convective events that have the greatest impact on the TTL. Results show strong temperature anomalies (~-3 K) at 17 km in connection with the 10% highest ozone mixing heights at American Samoa (refer to Figure 3.24) and temperature profiles in close proximity to convective cloud tops pixels greater than 15 km (refer to Figure 4.7 and 4.8). These finding demonstrate that deep convective events penetrating to the upper half of the TTL have the greatest impact on TTL temperature, stratification, and chemical composition.

This thesis presents an observational analysis of the TTL revealing new findings concerning the impact deep convection has on this region. Measurements are limited, yet we are also able to combine many recently developed datasets to provide a unique prospective of the TTL. Our successful approach exemplifies critical thinking and patience in face of a challenge.

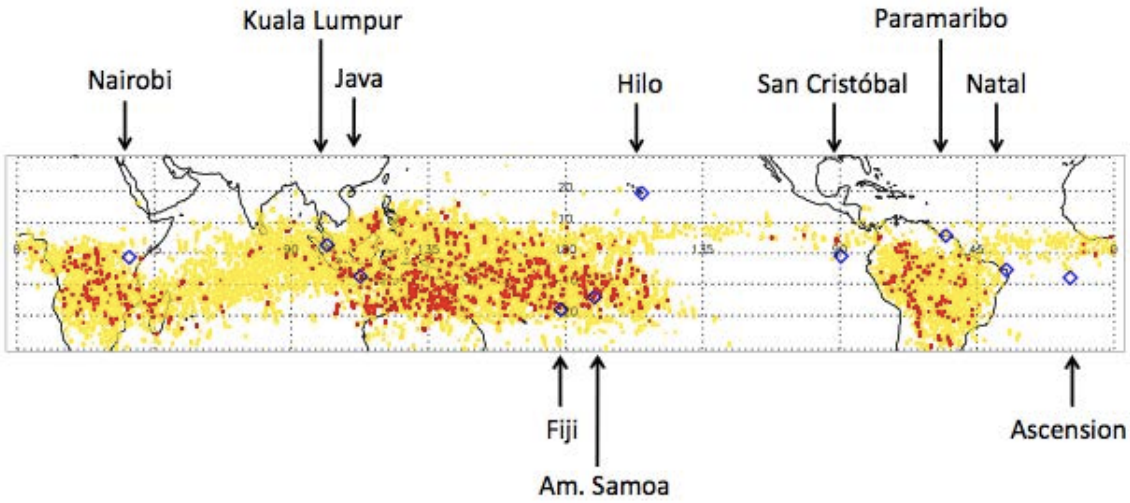

Figure 5.1: Spatial distribution of deep convective cloud top pixels greater than 15 km (yellow) and greater than 17 km (red) during DJF. The locations of SHADOZ stations investigated in this study are marked with blue diamonds.

A)

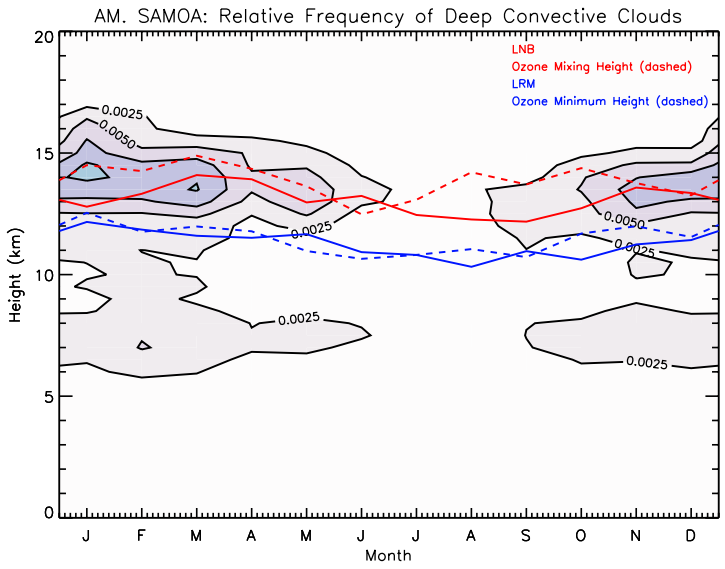

B)

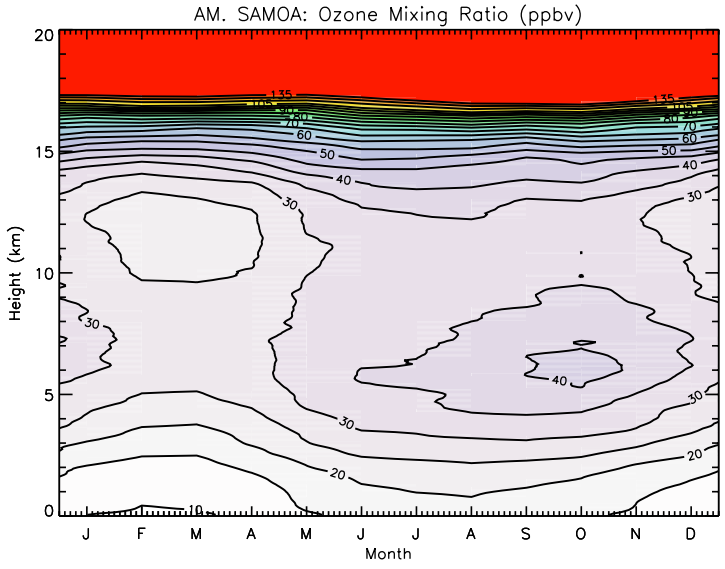

Figure 5.2: The (A) annual cycle of deep convective cloud top pixel height within 1000 km of American Samoa. Also included is the annual cycle of the LNB (red, solid), the ozone mixing height (red, dashed), the LRM height (blue, solid), and the ozone minimum height (blue, dashed). The (B) annual cycle of the ozone concentration (ppbv) at American Samoa similar to a plot in Thompson et al. (2011).

A)

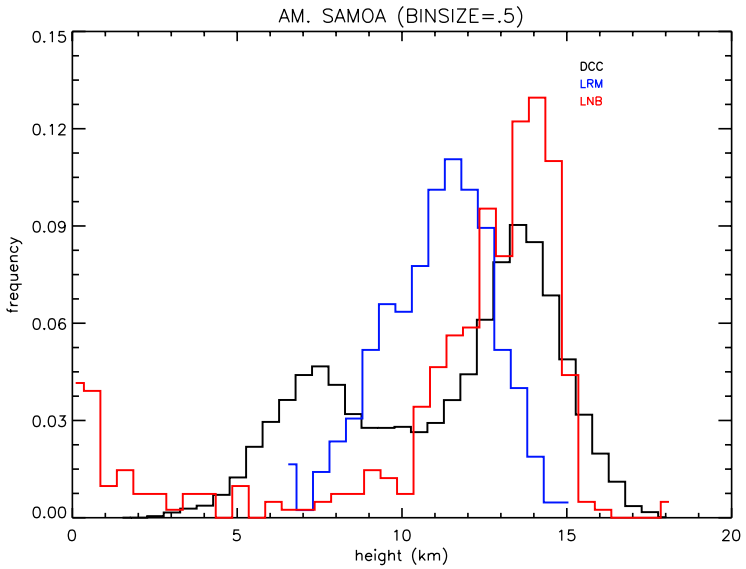

B)

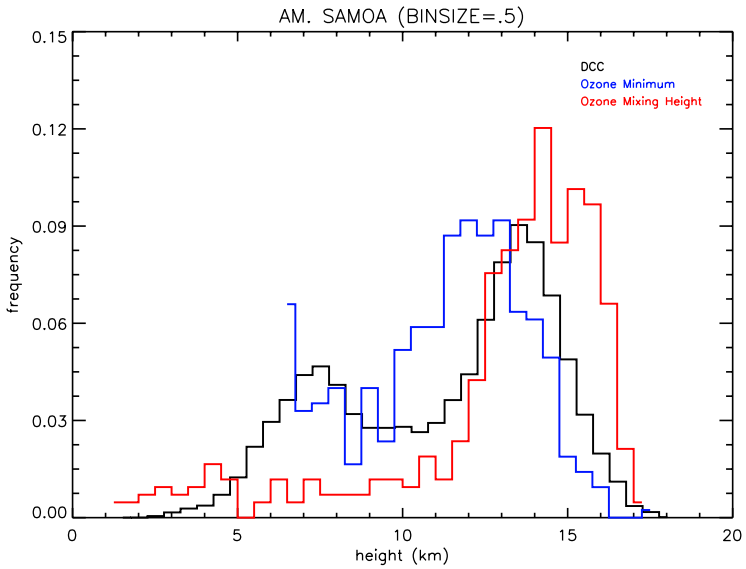

Figure 5.3: The (A) Frequency distribution of deep convective cloud top pixels height (black), LNB (red), and LRM (blue), and the (B) frequency distribution of deep convective cloud top pixels height (black), ozone mixing height (red), and the ozone minimum height (blue) at American Samoa.

A)

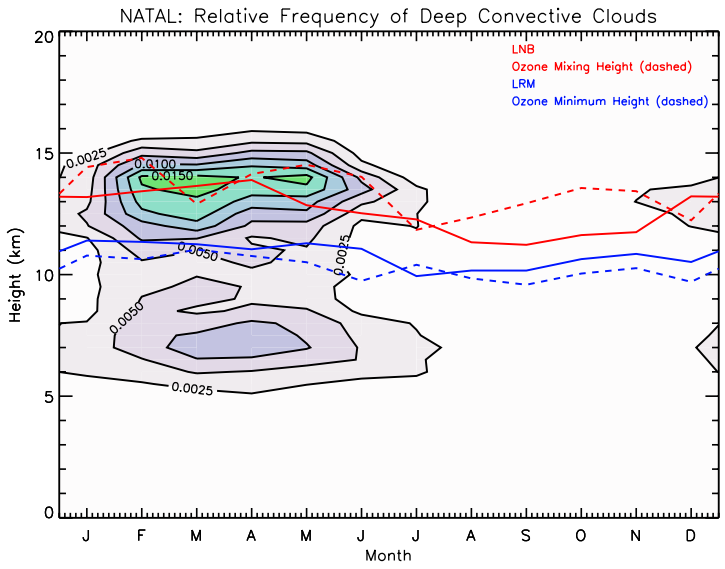

B)

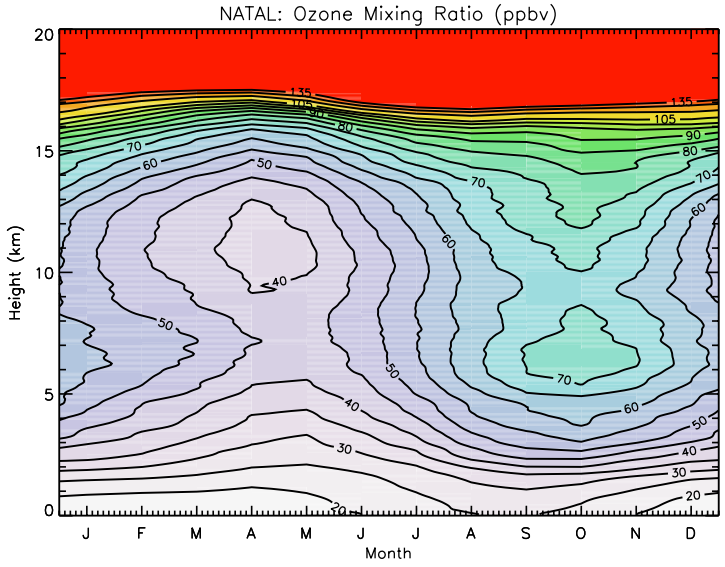

Figure 5.4: The (A) annual cycle of deep convective cloud top pixel height within 1000 km of American Samoa. Also included is the annual cycle of the LNB (red, solid), the ozone mixing height (red, dashed), the LRM height (blue, solid), and the ozone minimum height (blue, dashed). The (B) annual cycle of the ozone concentration (ppbv) at Natal similar to a plot in Thompson et al. (2011).

A)

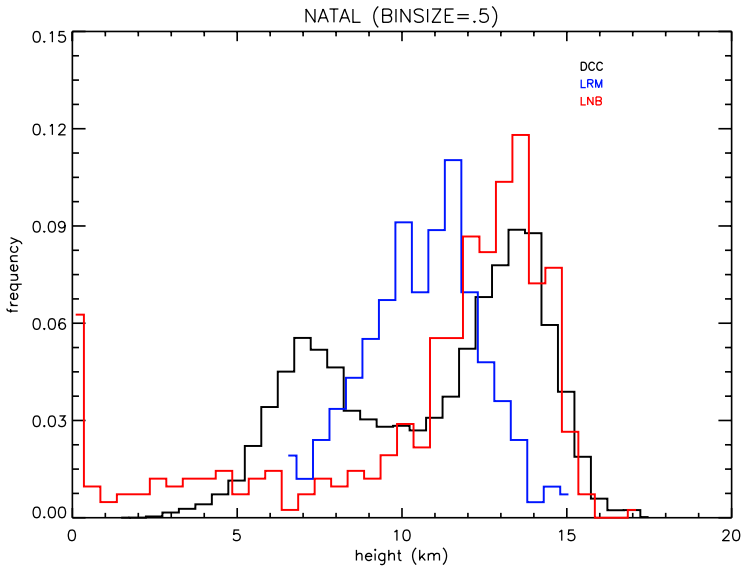

B)

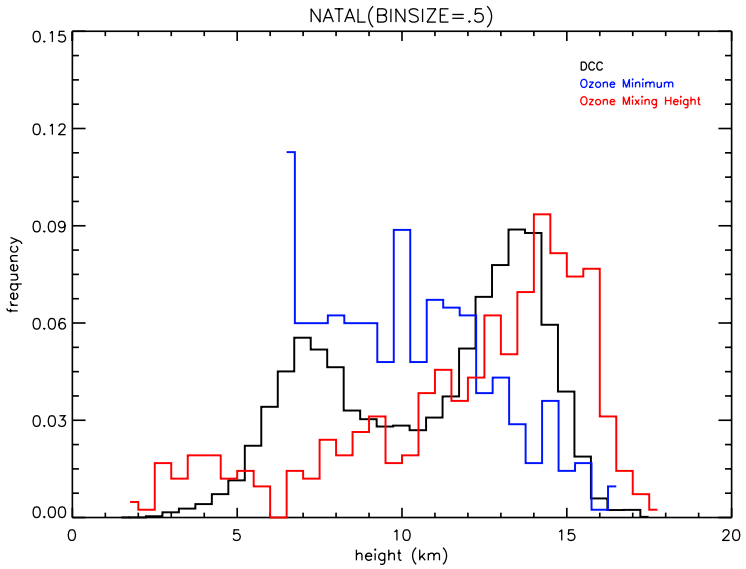

Figure 5.5: The (A) Frequency distribution of deep convective cloud top pixels height (black), LNB (red), and LRM (blue), and the (B) frequency distribution of deep convective cloud top pixels height (black), ozone mixing height (red), and the ozone minimum height (blue) at Natal.

REFERENCES

Anthes, R. A., and Coauthors, 2008: The COSMIC/FORMOSAT-3 Mission: Early Results. *Bull. Amer. Meteor. Soc.,* **89,** 313-333.

Birner, T., 2010: Residual circulation and tropopause structure. *J. Atmos. Sci.,* **67**, 2582–2600.

Brewer, A. W., 1949: Evidence for a world circulation provided by measurements of helium and water vapor distribution in the stratosphere. *Quart. J. Roy. Meteor. Soc.,* **75,** 351-363.

Calvo, N., R. R. Garcia, W. J. Randel, D. R. Marsh, 2010: Dynamical Mechanism for the Increase in Tropical Upwelling in the Lowermost Tropical Stratosphere during Warm ENSO Events. *J. Atmos. Sci.,* **67**, 2331–2340.

Charney, J. G., and P. G. Drazin, 1961: Propagation of planetary- scale disturbances from the lower into the upper atmosphere. *J. Geophys. Res.,* **66**, 83–109.

Corti, T., and Coauthors, 2008: Unprecedented evidence for deep convection hydrating the tropical stratosphere. *Geophys. Res. Lett.,* **35,** L10813, doi:10.1029/2008GL033641.

Folkins, I., M. Loewenstein, J. Podolske, S. J. Oltmans, and M. Porffitt, 1999: A barrier to vertical mixing at 14 km in the tropics: Evidence from ozonesondes and aircraft measurements. *J. Geophys. Res.*, **104**, 22,095-22,102.

Folkins, I., C. Braun, A. M. Thompson, and J. Witte, 2002: Tropical ozone as an indicator of deep convection. *J. Geophys. Res.*, **107,** 4184, doi: 10.1029/2001JD001178.

Folkins, I., S. Fueglistaler, G. Lesins, and T. Mitovski, 2008: A Low-Level Circulation in the Tropics. *J. Atmos. Sci.,* **65,** 1019-1034.

Fueglistaler, S., M. Bonazzola, P. H. Haynes, and T. Peter, 2005: Stratospheric water vapor predicted from Lagrangian temperature history of air entering the stratosphere in the tropics. *J. Geophys. Res.*, **110,** D08107, doi: 10.1029/2004JD005516.

Fueglistaler, S., A. E. Dessler, T. J. Dunkerton, I. Folkins, Q. Fu, and P. W. Mote, 2009: Tropical Tropopause Layer. *Rev. Geophys.,* **47,** RG1004, doi: 10.1029/2008RG000267.

García-Herrera, R., N. Calvo, R. R. Garcia, and M. A. Giorgetta, 2006: Propagation of ENSO temperature signals into the middle atmosphere: A comparison of two general circulation models and ERA-40 reanalysis data, *J. Geophys. Res.,* **111,** D06101, doi:10.1029/2005JD006061.

Gettelman, A., and P. M. de F. Forster, 2002: A Climatology of the Tropical Tropopause Layer. *J. Meteor. Soc. Japan,* **80,** 911-924.

Gettelman, A., and T. Birner, 2007: Insights into Tropical Tropopause processes using global models. *J. Geophys. Res.*, **112,** D23104, doi: 10.1029/2007JD008945.

Highwood, E. J., and B. J. Hoskins, 1998: The tropical tropopause. *Quart. J. Roy. Meteor. Soc.,* **124,** 1579-1604.

Holloway, C. E., and J. D. Neelin, 2006: The Convective Cold Top and Quasi Equilibrium. *J. Atmos. Sci.,* **64,** 1467-1487.

Holton, J. R., P. H. Haynes, M. E. McIntyre, A. R. Douglass, R. B. Rood, and L. Pfister, 1995: Stratosphere-Troposphere Exchange. *Rev. Geophys.,* **33,** 403-439.

Holton, J. R. and A. Gettelman, 2001: Horizontal transport and the dehydration of the stratosphere. *Geophys. Res. Lett.,* **28,** 2799-2802.

Houze, R. A. Jr., 1989: Observed structure of mesoscale convective systems and implications for large-scale heating. *Quart. J. Roy. Meteor. Soc.,***115,** 425-461.

Jacob, D. J., 1999: *Introduction to Atmospheric Chemistry.* Princeton University Press, 266 pp.

Kerr-Munslow, A. M., and W. A. Norton, 2006: Tropical Wave Driving of the Annual Cycle in Tropical Tropopause Temperatures. Part I: ECMWF Analyses. *J. Atmos. Sci.,* **63,** 1410-1419.

Kley, D., P. J. Crutzen, H. G. J. Smit, H. Vömel, S. J. Oltmans, H. Grassl, and V. Ramanathan, 1996: Observations of Near-Zero Ozone Concentrations over the Convective Pacific: Effects on Air Chemistry. *Science*, **274**, 230-233.

Kley, D., 1997: Tropospheric Chemistry and Transport. *Science*, **276,** 1043-1044.

Kuang, Z., and C. S. Bretherton, 2004: Convective Influence on the Heat Balance of the Tropical Tropopause Layer: A Cloud-Resolving Model Study. *J. Atmos. Sci.,* **61,** 2919-2927.

Kuo, Y. -H., W. S. Schreiner, J. Wang, D. L. Rossiter, Y. Zhang, 2005: Comparison of GPS radio occultation soundings with radiosondes. *Geophys. Res. Lett.,* **32,** L05817, doi:10.1029/2004GL021443.

Kursinski, E. R., and Coauthors, 1996: Initial results of radio occultation observations of the Earth's atmosphere using the Global Positioning System. *Science*, **271,** 1107-1110.

Kursinski, E. R., G. A. Haij, J. T. Schofield, R. P. Linfield, and K. R. Hardy, 1997: Observing the Earth's atmosphere with radio occultation measurements using the Global Positioning System. *J. Geophys. Res.*, **102**, 23429-23465.

Liu, C. and E. J. Zipser, 2005: Global distribution of convection penetrating the tropical tropopause. *J. Geophys. Res.*, **110,** D23104, doi: 10.1029/2005JD006063.

Luo, Z.. G. Y. Liu, and G. L. Stephens, 2008: CloudSat adding new insight into tropical penetrating convection. *Geophys. Res. Lett.,* **35,** L19819, doi: 10.1029/2008GL035330.

Newell, R. E., and S. Gould-Stewart, 1981: A stratospheric fountain? *J. Atmos. Sci.,* **38,** 2789-2796.

Norton, W. A., 2006: Tropical Wave Driving of the Annual Cycle in Tropical Tropopause Temperatures. Part II: Model Results. *J. Atmos. Sci.,* **63,** 1420-1431.

Randel, W. J., and F. Wu, 2003: Thermal variability of the tropical tropopause region derived from GPS/MET observations. *J. Geophys. Res.*, **108,** 4024, doi: 10.1029/2002JD002595.

Randel, W. J., M. Park, F. Wu and N. Livesey, 2007: A large annual cycle in ozone above the tropical tropopause linked to the Brewer-Dobson circulation. *J. Atmos. Sci.,* **64,** 4479-4488.

Randel, W. J., R. R. Garcia, N. Calvo, and D. Marsh, 2009: ENSO influence on zonal mean temperature and ozone in the tropical lower stratosphere, *Geophys. Res. Lett.,* **36,** L15822, doi:10.1029/2009GL039343.

Reid, G. C., and K. S. Gage, 1981: On the Annual Variation in Height of the Tropical Tropopause. *J. Atmos. Sci.,* **38,** 1928-1938.

Reid, G. C., and K. S. Gage, 1996:The tropical tropopause over the western Pacific: Wave driving, convection, and the annual cycle. *J. Geophys. Res.*, **101**, 21233-21241.

Riehl, H and J. S. Malkus, 1958: On the heat balance in the equatorial trough zone. *Geophysica*, **6,** 503-538.

Romps, D. M., 2010: A direct measure of entrainment. *J. Atmos. Sci.,* **67**, 1908–1927.

Sassen K. and Z. Wang, 2008: Classifying clouds around the globe with CloudSat radar: 1-year of results. *Geophys. Res. Lett.,* **35,** L04805, doi: 10.1029/2007GL032591.

Sherwood, S. C., and A. E. Dessler, 2000: On the control of stratospheric humidity. *Geophys. Res. Lett.,* **27,** 2513-2516.

Solomon, S., D. W. J. Thompson, R. W. Portmann, S. J. Oltmans, and A. M. Thompson, 2005: On the distribution and variability of ozone on the tropical upper troposphere: Implications for tropical deep convection and chemical-dynamical coupling. *Geophys. Res. Lett.,* **32,** L23813, doi: 10.1029/2005GL024323.

Stephens, G. L., and Coauthors, 2002: The CloudSat Mission and the A-Train. *Bull. Amer. Meteor. Soc.,* **83,** 1771-1790.

Thompson, A. M., and Coauthors, 2003a: Southern Hemisphere Additional Ozonesondes (SHADOZ) 1998-2000 tropical ozone climatology 1. Comparison with Total Ozone Mapping Spectrometer (TOMS) and ground-based measurements. *J. Geophys. Res.*, **108,** 8238, doi: 10.1029/2001JD000967.

Thompson, A.M., and Coauthors, 2003b: Southern Hemisphere Additional Ozonesondes (SHADOZ) 1998-2000 tropical ozone climatology 2. Tropospheric variability and the zonal wave-one. *J. Geophys. Res.*, **108,** 8241, doi: 10.1029/2002JD002241.

Thompson, A. M., A. L. Allen, S. Lee, S. K. Miller, and J. C. Witte, 2011: Gravity and Rossby wave signatures in the tropical troposphere and lower stratosphere based on Southern Hemisphere Additional Ozonesondes (SHADOZ), 1998-2007. *J. Geophys. Res.*, **116,** D05302, doi: 10.1029/2009JD013429.

Vallis, G. K., 2006: *Atmospheric and Oceanic Fluid Dynamics*. Cambridge University Press, 745 pp.

Vömel, H., and K. Diaz, 2010: Ozone sonde cell current measurements and implications for observations of near-zero ozone concentrations in the tropical upper troposphere. *Atmos. Meas. Tech.*, **3,** 495-505, doi: 10.5194/amt-3-495-2010.

Wayne, R. P., 1991: *Chemistry of Atmospheres.* Oxford University Press.

Yulaeva, E., J. R. Holton, and J. M. Wallace, 1994: On the cause of the Annual Cycle in Tropical Lower-Stratospheric Temperatures. *J. Atmos. Sci.,* **51,** 169-174.